NASA CR-140199
ERIM 190100-24-T

NASA

RADIATIVE TRANSFER IN REAL ATMOSPHERES

by

Robert E. Turner
Infrared and Optics Division

July 1974

ENVIRONMENTAL RESEARCH INSTITUTE OF MICHIGAN
FORMERLY WILLOW RUN LABORATORIES, THE UNIVERSITY OF MICHIGAN

prepared for

NATIONAL AERONAUTICS AND SPACE ADMINISTRATION

Johnson Space Center, Houston, Texas 77058
Earth Observations Division
Contract NAS 9-9784, Task IV

TECHNICAL REPORT STANDARD TITLE PAGE

1. Report No. NASA CR-ERIM 190100-24-T	2. Government Accession No.	3. Recipient's Catalog No.
4. Title and Subtitle RADIATIVE TRANSFER IN REAL ATMOSPHERES		5. Report Date December 1973 6. Performing Organization Code
7. Author(s) Robert E. Turner		8. Performing Organization Report No. ERIM 190100-24-T
9. Performing Organization Name and Address Environmental Research Institute of Michigan Infrared and Optics Division P.O. Box 618 Ann Arbor, Michigan 48107		10. Work Unit No. Task IV 11. Contract or Grant No. NAS9-9784
12. Sponsoring Agency Name and Address National Aeronautics and Space Administration Johnson Space Center Earth Observations Division Houston, Texas 77058		13. Type of Report and Period Covered Technical Report 1 February 1973 - 31 October 1973 14. Sponsoring Agency Code

15. Supplementary Notes

Dr. Andrew Potter/TF3 is Technical Monitor for NASA.

16. Abstract

Any complete analysis of multispectral data must include the effects of the atmosphere on the radiation field. This report treats the problem of multiply scattered radiation in an atmosphere characterized by various amounts of aerosol absorption and different particle-size distributions. Emphasis is put on the visible part of the spectrum and includes the effect of ozone absorption. Absorption by other gaseous components in the infrared region is not treated.

The work also includes an investigation of an atmosphere bounded by a non-homogeneous, Lambertian surface. The effect of background on target is studied in terms of various atmospheric and geometric conditions.

Results of this investigation show that contaminated atmospheres can change the radiation field by a considerable amount and that the effect of a non-uniform surface can significantly alter the intrinsic radiation from a target element—a fact of considerable importance in the recognition processing of multispectral remote sensing data.

17. Key Words	18. Distribution Statement
Aerosol absorption Multiply scattered radiation Ozone absorption Recognition processing Remote sensing	Initial distribution is listed at the end of this document.

19. Security Classif. (of this report)	20. Security Classif. (of this page)	21. No. of Pages	22. Price
UNCLASSIFIED	UNCLASSIFIED	106	

PREFACE

This report describes part of a comprehensive, continuing research program in remote sensing of the environment by aircraft and satellite. The research is being conducted for NASA's Lyndon B Johnson Space Center, Houston, Texas, by the Environmental Research Institute of Michigan (ERIM), formerly the Willow Run Laboratories, Institute of Science and Technology, The University of Michigan. The main objective of this program is to develop remote sensing as a practical tool for obtaining extensive environmental information quickly and economically.

Remote sensing of the environment involves the transfer of radiation from objects of interest on the Earth's surface through the atmosphere to a sensor either within or outside the atmosphere. Since this intervening atmospheric medium alters the intrinsic radiation from surface elements, the interpretation of multispectral scanner data can be significantly affected. This report deals with the definition of the natural radiation field encountered in a realistic remote sensing environment from the viewpoints of radiative-transfer theory and atmospheric optics.

The research described in this report was performed under Contract NAS9-9784, Task IV, and covers the period from 1 February 1973 through 31 October 1973. Dr. Andrew Potter served as Technical Monitor. The program was directed by R. R. Legault, Vice President of ERIM, J. D. Erickson, Principal Investigator and Head of ERIM's Information Systems and Analysis Department, and R. F. Nalepka, Head of ERIM's Multispectral Analysis Section. The ERIM number of this report is 190100-24-T.

The author wishes to acknowledge the direction provided by R. R. Legault and J. D. Erickson. Helpful suggestions were made by R. F. Nalepka. Computer programming and other technical analysis were provided by N. A. Contaxes, W. B. Morgan, and L. R. Ziegler. The author also thanks R. M. Coleman for her secretarial assistance in the preparation of this report.

CONTENTS

PRECEDING PAGE BLANK NOT FILMED

FIGURES

SYMBOLS

A	aerosol (subscript)
a, α, b, γ	distribution parameters
b_o	brightness factor
C	contrast
C_o	contrast ratio $(1 - L_o/L_B)$
E_o	extraterrestrial solar irradiance at the top of the atmosphere
E''	isotropic field
$\tilde{E}_-$	total downward irradiance
f	aerosol absorptivity factor
I	intensity of radiation
i	index for a, s, or t, Eq. (39)
I(o)	beam intensity at origin
$\vec{k}$	complex propagation vector
L_{att}	directly attenuated scattering component
L_B	background radiance
L_{ds}	doubly scattered sky radiance
L_o	intrinsic radiance of the object
L_P	spectral path radiance
L_p	radiance along infinite path through atmosphere
$\bar{L}(\hat{R}, \hat{\Omega})$	total spectral radiance
L_S	spectral radiance at surface
L_{sur}	singly scattered surface radiance
L_{tot}	sum of $L_{sur} + L_{ss} + L_{ds}$
L_{ss}	singly scattered sky radiance
m_1	real part of refractive index
m_2	imaginary part of refractive index
η	refractive index of the medium
$m(\lambda)$	refractive index
N	molecular number density

$N(z, r)$	particle number density for radius r at altitude z
$P(\cos \chi)$	scattering phase function
$P_\ell(\cos \chi)$	Legendre polynomial
$p(\cos \chi)$	scattering phase function
$Q_s(x, m)$	scattering efficiency factor
$\vec{r}$	coordinate position vector
s	particulate size distribution
T	spectral transmittance
t	time or total
$t(\lambda)$	aerosol turbidity
V	visual range
x	distance, size parameter
$\alpha_A(\lambda, m, z)$	absorption coefficient for polydispersion
$\beta_A(\lambda, m, z)$	scattering coefficient for polydispersion
δ	anisotropy parameter
κ	volume extinction coefficient
$\kappa_A(\lambda, m, z)$	extinction coefficient for polydispersion
$\kappa_d(\lambda)$	volume extinction coefficient for dust particle
$\kappa_R(\lambda)$	volume extinction coefficient for Rayleigh scattering
$\kappa_w(\lambda)$	volume extinction coefficient for water aerosol
μ_o, ϕ_o	angular coordinates of the sun
$\eta(\tau)$	anisotropy parameter
ξ	$\sin \eta \cos \psi$
ν	$\sin \eta \cos \psi$
ρ_i	interior Lambertian disk reflectance
ρ_e	exterior Lambertian disk reflectance
$\sigma_R(\lambda)$	Rayleigh scattering cross section
$\sigma_s(\lambda, r, m)$	scattering cross section
$\sigma_t(\lambda, r, m)$	total cross-section scattering
(τ)	optical depth
χ	angle between the incoming direction and the scattered direction
ψ_ℓ and ζ_ℓ	Riccati-Bessel functions

Ω	solid angle
$\hat{\Omega}$	unit vector in the direction of the scattered photon at position $\hat{R}$
ω	angular frequency
$\omega_0(\tau)$	single-scattering albedo

1
SUMMARY

As part of the continuing development of an atmospheric-radiative-transfer model which can be used to correct multispectral data, we must consider as many atmospheric effects as possible that may have an influence on the data. In previous studies we have constructed a radiative-transfer model which included the effect of multiple scattering in homogeneous, non-absorbing, plane-parallel atmospheres bounded by spatially uniform surface conditions. Although variable atmospheric states characterized by visual range were included, we considered only non-absorbing aerosol particles in the atmosphere. Also, the surface dealt with was a spatially uniform Lambertian one.

In the present further work we consider a variety of more realistic atmospheric conditions characterized by visual range, composition of aerosols, size distribution of aerosol particles, and ozone absorption. Hence, we have expanded our atmospheric-radiative-transfer model to include almost every kind of atmospheric state possible with regard to the composition and structure of aerosols. Excluded are certain strong gaseous absorption effects in the infrared, with this omission justified on the grounds that in the design of sensors, one usually ignores these regions anyway.

Another problem addressed in the current study is the occasional influence of background on the target through radiation being scattered from elements outside the instantaneous field of view into that field of view. In this report we examine this effect and employ the necessary approximations to solve the problem analytically Also, a solution is presented for the case of an airborne or spacecraft sensor viewing a non-Lambertian surface from any point in or outside of the atmosphere. This solution can be used in an analysis of the changes to be expected in multispectral data as a sensor moves in a horizontal plane over the terrain being investigated.

2

INTRODUCTION

In the remote sensing of terrain features on Earth's surface, discrimination of specific targets from their backgrounds is essential. One method of accomplishing this is to analyze the radiation received in several wavelength intervals on the assumption that classes of objects can be defined in terms of their spectral properties. Such analysis depends upon variabilities in remotely sensed data which can be attributed to the complex spectral properties intrinsic to materials found on the Earth's surface. Discrimination techniques are by no means limited to spectral variations alone; other schemes can be based upon polarization or goniometric characteristics of various classes of objects to provide a "signature" and thus a unique means of identification. But remote sensing based upon polarization and/or goniometric properties has not found widespread use, probably because (1) very little is known about the intrinsic polarization characteristics of natural materials and even less concerning their goniometric properties, and (2) the sensor requirements and operational systems needed to acquire meaningful data based upon these properties are rather complex. In this report, however, we deal exclusively with analytical approaches applicable to the development and implementation of discrimination techniques based upon spectral variations.

Aside from the intrinsic properties of natural materials, there exist variations, such as the variability of the atmosphere, resulting from elements extrinsic to these materials. Although one would like to collect data under ideal environmental conditions, the implementation of an operational remote sensing system necessitates the acquisition of data under conditions which, unfortunately, are oftentimes far from ideal. For this reason it is important that the more systematic variations associated with atmospheric effects be considered in the analysis of remote sensor data.

The spectral radiance at a sensor is given by the following:

$$L_T = L_S T + L_P$$

where L_S is the spectral radiance at the surface

T is the spectral transmittance between the sensor and the object being observed

L_P is the spectral path radiance—that is, the radiation along the path between the sensor and target arising from multiple scattering or intrinsic emission

All three of these quantities depend upon the state of the atmosphere; they can vary considerably with altitude, wavelength, view angle, sun angle, and surface albedo. A complete atmospheric radiation model should provide those quantities which determine a unique set of parameters appropriate to the environmental conditions which exist at a particular time.

Previous work on this problem has resulted in an atmospheric-radiative-transfer model which accounts —assuming multiple scattering in cloudless, plane-parallel atmospheres with no absorption—for variations in the radiometric quantities named above. The usual assumption in atmospheric-radiative-transfer problems is that there is little absorption by aerosols in the visible part of the electromagnetic spectrum. This is definitely not the case, however, for the contaminated air commonly found in large urban areas where sulfate, carbonate, and other soot particles exist in large quantities. Furthermore, from recent investigations of the atmospheric particulate load around the world, it is becoming evident that aerosols play an important role in determining the overall energy balance of Earth. For this reason we investigated the influence of contaminated atmospheres on the natural radiation field.

Another effect treated in this report is the influence of background on target via scattering in the atmosphere. Radiation reflected from background objects will eventually be scattered into the field of view of a sensor and, hence, will influence the signal from the target. This complicated effect requires that the radiative-transfer equation be solved in two or three dimensions in order to define the radiation field anywhere in the atmosphere for non-homogeneous boundaries. In our study of this phenomenon, we assume it to be a function of basic parameters describing pertinent optical characteristics of the atmosphere.

3
THE ATMOSPHERIC STATE

In the remote sensing of Earth's surface by means of electromagnetic radiation reflected from terrain objects, the atmosphere can scatter and absorb the radiation and, hence, alter the intrinsic radiation characteristics of the object being investigated. The resultant radiation received by a sensor depends upon factors such as viewing geometry, time of year, surface conditions, and atmospheric state. It is the state of the atmosphere that we shall discuss in this section.

3.1 COMPOSITION OF THE ATMOSPHERE

The state of the atmosphere at any location and at any time can be defined by a unique set of parameters fully describing all aspects of the atmosphere. However, we are not interested in all aspects of the atmosphere, but only in those of key importance to remote sensing applications. Thus, micro-fluctuations in density or ion content are of no import, but we are certainly interested in visibility. Our goal, therefore, is a somewhat limited specification of parameters which can be used to define the state of the atmosphere. For purposes of the present study, we shall be concerned mainly with the scattering and absorbing properties of gases and particulates that exist in our atmosphere.

3.1.1 ATMOSPHERIC GASES

By definition, the visible portion of the electromagnetic spectrum is that part of it to which the human eye is most sensitive; thus it is not surprising that this part of the spectrum undergoes little absorption by the atmosphere. The major permanent gaseous components of our atmosphere are molecular oxygen, nitrogen, and argon. These gases absorb very little radiation in the visible and near-infrared part of the spectrum; only variable components such as water vapor, carbon dioxide, ozone, sulfur dioxide, nitrogen compounds, methane, and other trace gases absorb such radiation to any extent. Of these variable components, ozone, water vapor, and carbon dioxide are the most important absorbers of radiation in the near-infrared. For the purposes of this study, we shall consider only ozone in the Chappuis bands in the region 0.44 to 0.74 μm and assume that all other radiation in the region 0.40 to ~2.0 μm is not absorbed by gases. Since the gaseous absorption regimes of the various atmospheric components are well known, it is relatively easy to select those spectral regions within which absorption is at a minimum. More detailed studies of atmospheric gases have been done by Goody [1] and Zuyev [2].

Throughout the visible part of the spectrum, ozone is the primary gaseous absorber. There are variable amounts in the troposphere, but the general altitude variation is known [3]. A profile of the ozone number density is illustrated in Fig. 1. Note that the maximum density occurs at an altitude of about 23 km.

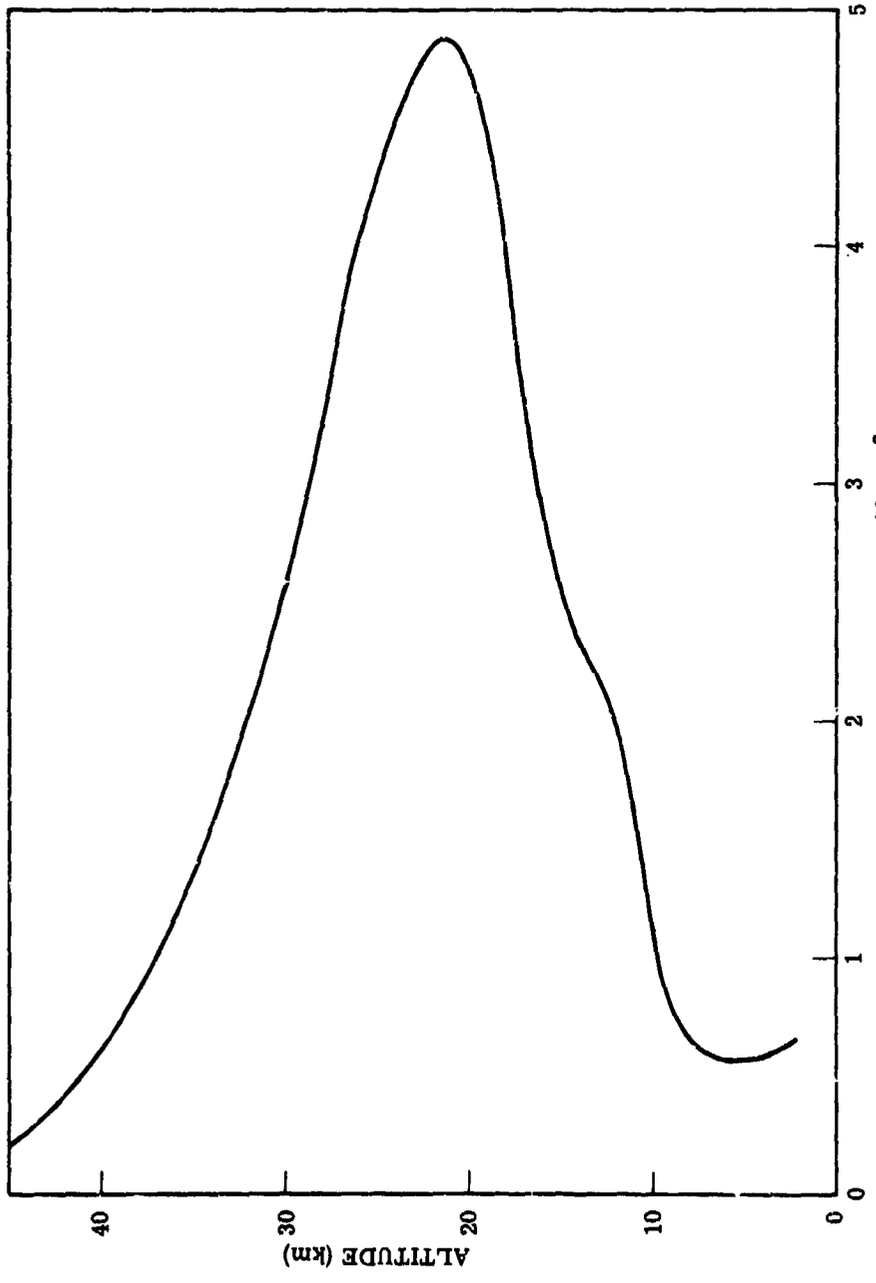

FIGURE 1. ALTITUDE PROFILE FOR OZONE DENSITY

3.1.2 AEROSOLS

One may define an aerosol as a semi-permanent suspension of solid or liquid particles in the Earth's atmosphere. Typical aerosol distributions would be hazes, clouds, mists, fogs, smokes, and dusts. It is the aerosol component of the atmosphere which is quite variable. Depending upon location and time, aerosols can have many compositions, sizes, shapes, and densities. In condensation processes, the predominant composition is water (for which the refractive index is well known). Depending upon the history of the distribution, however, various contaminants can mix with water and water vapor in the formation of droplets to produce a composition quite different from that of water. The major primary source of atmospheric aerosols on a world-wide basis is sea spray [4]; other primary sources are wind-blown dust and smoke from forest fires. While the composition of worldwide aerosol distribution can be estimated, this composition can nevertheless vary over a wide range depending upon its proximity to various local sources. The only ways in which the composition can be determined is by direct in situ sampling of the air in a particular location or by radiometric techniques. Much in situ sampling has been done by Volz [5, 6], Grams et al. [7], and Flanigan and Delong [8]. As a result of their work and that of others, the mean world-wide aerosol can be considered to have a real refractive index of about 1.5 and an imaginary part between 0.01 and 1.0. Hence,

$$m(\lambda) = m_1 - im_2 \tag{1}$$

where m_1 and m_2, respectively, are the real and imaginary part of the refractive index, and λ is the wavelength. For realistic atmospheric conditions,

$$1.33 \lesssim m_1 \lesssim 1.55 \tag{2}$$

and

$$0 < m_2 \lesssim 1.0 \tag{3}$$

which are roughly independent of wavelength.

Particles also come in various sizes. Generally, however, they can be put into three categories: the Aitken nuclei with radii between 10^{-7} and 10^{-5} cm, the large particles with radii between 10^{-5} and 10^{-4} cm, and the so-called giant particles with radii greater than 10^{-4} cm. In most hazes, the optically active region is made up of those particles in the large or giant categories. Junge [9] showed that most aerosol distributions follow the simple power law.

$$N(z, r) = C(z)r^{-\nu} \tag{4}$$

where N(z, r) is the particle number density for radius, r, at altitude, z

ν is the exponent of the power law

Experimentally, ν has been found to vary from 2 to 5 for various tropospheric aerosol distributions. Also, other investigators have found a better fit to the particulate data by using the modified gamma distribution,

$$N(z, r) = ar^{\alpha} \exp(-br^{\gamma}); \quad 0 \leq r < \infty \tag{5}$$

where a, α, b, and γ are parameters which describe the distribution.

Deirmendjian [10] has used this function to characterize different hazes. The following is a list of the hazes Deirmendjian considered and the relevant parameters.

Haze Type	a	α	γ	b
M	5.3333×10^4	1	1/2	8.9443
L	4.9757×10^6	2	1/2	15.1186
H	4.0000×10^5	2	1	20.0000

Haze M, used to describe a marine or coastal haze, has a peak in the distribution at $r = 0.05\mu m$. The haze L represents a continental distribution and has a peak at $r = 0.07\mu m$. The haze H model can be used to represent a stratospheric aerosol or dust layers; it has a peak at $0.10\mu m$. A graph of the three hazes is illustrated in Fig. 2. We shall make use of these hazes in the detailed analysis of atmospheric radiation.

For the liquid aerosols it can be assumed that the particles are spherical or nearly spherical in shape. For solid particles, however, the shape may assume any form. A number of investigators [11, 12, 13] have studied the influence of particle shape on the scattering of radiation. The scattering of electromagnetic radiation by odd-shaped particles has a different pattern from that produced by spherical particles; but given a polydisperse collection of odd-shaped particles, the nature of the difference is not clear. Most of the work on radiation in atmospheres concerns spherical aerosols; we shall follow suit and neglect the complications of particle shape.

Thus far we have considered the composition, sizes, and shapes of aerosol particles, but in order to define the atmospheric state we must also know the concentration of particles. Wiegand [14] was the first to measure the vertical profile of an aerosol number concentration of condensation nuclei. As a result of his measurements and many others cited in Ivlev [15], it was found that the concentration of condensation nuclei obeys an exponential law with altitude. It was also determined that a zone of increased concentration of large particles exists in the

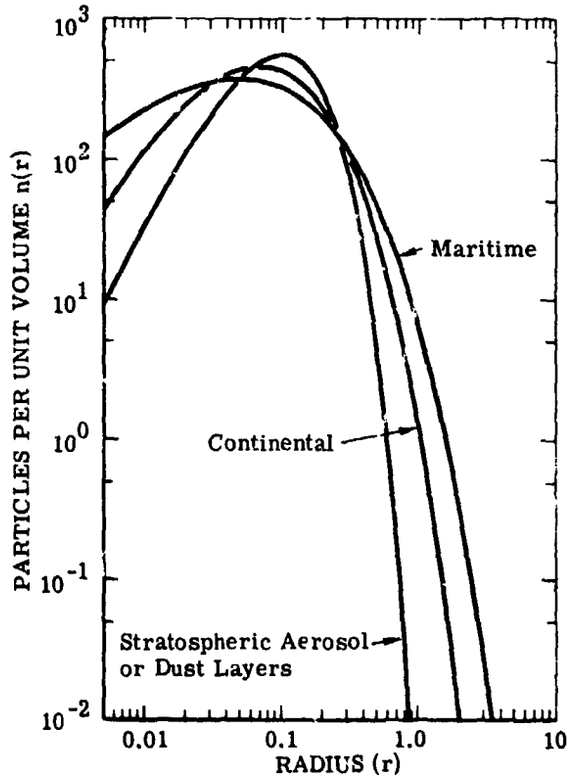

FIGURE 2. HAZE-TYPE DISTRIBUTION FUNCTIONS USED. Units depend on the particular model. [10]

17 to 23 km altitude range (Junge layer) and in a probable layer under the tropopause at 9 to 10 km. These layers are relatively stable compared to the lower part of the troposphere. As an example of an aerosol model atmosphere, Zuyev [2] has constructed the following altitude-dependent, number density-distribution-function for aerosols:

$$N(z) = \begin{cases} N(0)e^{-bz}; & z \le 5 \text{ km} \\ 0.03; & 5 \text{ km} \le z \le 15 \text{ km} \\ 0.03e^{0.06z}, & 15 \text{ km} \le z \le 20 \text{ km} \\ 0.01e^{-0.09z}; & z \ge 20 \text{ km} \end{cases} \tag{6}$$

where N(z) and N(0), respectively, are the number densities at altitude z and the Earth's surface (altitude 0).

In conclusion, we can say that the most significant aspect of aerosol particles in the atmosphere is their high degree of variability—in composition, size distribution, and especially in number density. All the models in the current literature deal with a highly approximate average-condition from which large deviations can occur in real situations. The many details of aerosol science will not be considered in this report. For a more complete study of the physics and chemistry of aerosols, see Mason [16], Fuchs [17], Davies [18], or Green and Lane [19].

3.2 TURBIDITY

Having examined the basic characteristics of the gases and aerosol particles composing the atmosphere, we now consider those parameters which relate to the attenuation of radiation passing through the atmosphere.

If a collimated beam of monochromatic radiation is incident upon a scattering and absorbing medium, then the intensity of the beam at distance x is given by

$$I(x) = I(0)e^{-\kappa x} \tag{7}$$

where I(o) is the beam intensity at the origin. The quantity κ, called the volume extinction coefficient, is equal to the sum of the volume absorption and volume scattering coefficients. Since attenuation of radiation in the atmosphere is caused primarily by molecular scattering, scattering and absorption by water droplets, and also by dust particles, Linke [20] proposed that the attenuation be measured by taking the ratio of the total integrated attenuation coefficients to the pure Rayleigh integrated coefficients. Thus,

$$t(\lambda) = \frac{\int_0^\infty \kappa_R(\lambda)dz + \int_0^\infty \kappa_w(\lambda)dz + \int_0^\infty \kappa_d(\lambda)dz}{\int_0^\infty \kappa_R(\lambda)dz} \tag{8}$$

where $\kappa_R(\lambda)$, $\kappa_w(\lambda)$, and $\kappa_d(\lambda)$ are the volume extinction coefficients for Rayleigh, water aerosol, and dust particle scattering respectively. Thus, the turbidity, $t(\lambda)$, is a measure of the departure of a real atmosphere from the ideal pure Rayleigh atmosphere. Equation (8) can also be written as

$$t = 1 + W + R \tag{9}$$

where W is the humid turbidity factor and R is the residual turbidity factor. For a pure atmosphere free of water and dust, t = 1. Values of the turbidity vary from 3.59 for a continental tropical air mass in the summer months to 2.16 for a sea arctic air mass in winter. Tables of typical turbidity values are given by Kondratyev [21] for many locations and weather conditions. The turbidity as a function of altitude is shown in Fig. 3 [22]; this figure was constructed from data collected by Elterman [23] in optical searchlight measurements. The maximum near the tropopause is the result of convective activity causing particles to concentrate at that stable position.

3.3 VISIBILITY

Visibility in meteorology refers to the transparency of the atmosphere to visible radiation. Usually characterized by a quantity, V, called visual range, it depends upon the optical properties of the atmosphere, the properties of both the object sighted and its background, and illumination conditions. Middleton [24] derives the so-called air-light equation given by

$$L = L_o e^{-\kappa x} + L_p(1-e^{-\kappa x}) \tag{10}$$

where L_o is the intrinsic radiance of the object
L_p is the radiance along an infinite path through the atmosphere
κ is the volume extinction coefficient

Tverskoi [25] derives a contrast equation:

$$C = \frac{C_o}{1 + \frac{1}{b_o}(e^{-\kappa x} - 1)} \tag{11}$$

where C_o is the ratio of the difference between background and intrinsic radiances to background radiances, and b_o is a brightness factor. This equation can be simplified:

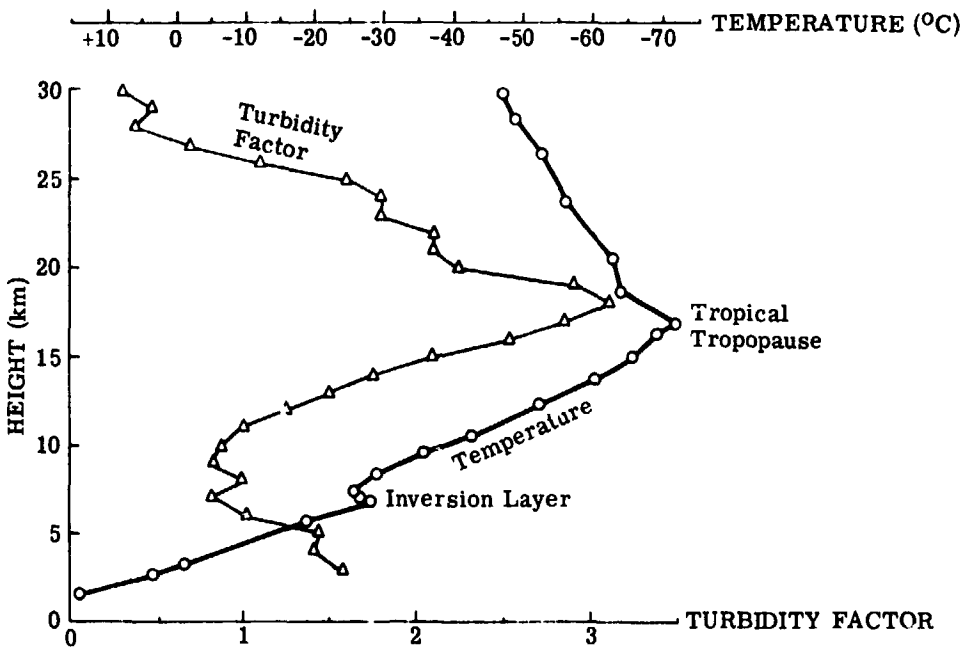

FIGURE 3. AEROSOL AND TEMPERATURE PROFILES FOR 4-5 NOVEMBER 1964 [22]

$$C = C_o e^{-\kappa x} \tag{12}$$

The visual range in km is that distance at which the relative contrast is 2%, i.e.,

$$\ell n(C/C_o) = \ell n\, 0.02 = e^{-\kappa V} \tag{13}$$

or

$$V = -\frac{\ell n\, 0.02}{\kappa} = \frac{3.912}{\kappa} \tag{14}$$

Equation (14) is usually taken as the defining equation for visual range at a wavelength of 0.55μm, which is near the peak of the human visual-response curve.

4
OPTICAL PARAMETERS

Section 3 considered the physical state of the atmosphere. In this section we deal with the optical properties of the atmosphere; specifically, we define and calculate the appropriate atmospheric optical parameters used in radiative-transfer models.

4.1 SCATTERING THEORY

Radiation which passes through a homogeneous medium free of any discontinuities will cause waves to interfere in such a way that no scattering takes place. Realistic media at temperatures above absolute zero, however, have discontinuities such as crystal impurities, density fluctuations, and various sized particles; Earth's atmosphere is such a medium. We assume, moreover, that all scatterings are independent, that is, that there is no phase relation between scattered waves. For this to be true, the distance between scattering centers must be at least several times the size of the scattering centers themselves. This condition is certainly fulfilled for atmospheric hazes and even for dense fogs. Given this physical setting, we will now determine the basic optical quantities needed for radiative-transfer analysis.

4.1.1 RAYLEIGH SCATTERING

The theory of light scattering in the atmosphere originated when Lord Rayleigh [26] found an explanation for the blue color of the clear sky. It is now known that this hue is the result of the scattering of radiation from density fluctuations, rather than from molecules as had been assumed earlier. If we have a plane electromagnetic wave with electric field strength

$$\vec{E}(\vec{r},t) = \vec{E}_o e^{i(\vec{k}\cdot\vec{r}-\omega t)} \tag{15}$$

where $\vec{k}$ is the complex propagation vector

$\vec{r}$ is a coordinate position vector

ω is the angular frequency

then this wave impinging upon a scattering center whose size is much smaller than the wavelength of the radiation will produce scattered waves in an effect called Rayleigh scattering. The scattering cross-section can be obtained by integrating the Poynting vector over a period of oscillation. The result is

$$\sigma_R(\lambda) = \frac{8\pi^3}{3N^2\lambda^4}\left(m^2 - 1\right)^2 \cdot \frac{6 + 3\delta}{6 - 7\delta} \tag{16}$$

where N is the molecular number density

λ is the wavelength

δ is an anisotropy parameter to account for polarization effects

m is the refractive index of the medium

Of importance here is the $1/\lambda^4$ dependence of the cross-section, a characteristic of radiation from an oscillating dipole field.

It can also be shown that the scattering pattern is described by the following formula:

$$p(\cos\chi) = \frac{3}{4}(1 + \cos^2\chi) \tag{17}$$

in which χ is the angle between the incoming direction and the scattered direction. The function $p(\cos\chi)$, which is called the scattering phase function, is normalized to unity over all 4π steradians, that is,

$$\int_{\Omega} p(\cos\chi)\,d\Omega = 1 \tag{18}$$

where Ω is the solid angle.

4.1.2 MIE SCATTERING

The scattering of electromagnetic radiation by homogeneous dielectric spheres is called Mie scattering. In principle, determining the scattering and absorption cross-sections and the scattering phase function is straightforward. First, the wave equation is solved inside and outside the sphere; then the solutions are matched at the boundary to determine the constants. The intensity of the radiation scattered into an angle χ is given by

$$I = \frac{\lambda^2}{4\pi^2 R^2}\,\frac{|S_1|^2 + |S_2|^2}{2}\,I_o \tag{19}$$

where R is the distance from the sphere, and I_o is the incident intensity. The scattering amplitudes $|S_1|^2$ and $|S_2|^2$ are given by

$$\begin{aligned} S_1 &= \sum_{\ell=1}^{\infty} \frac{2\ell+1}{\ell(\ell+1)}\left[a_\ell \pi_\ell + b_\ell \tau_\ell\right] \\ S_2 &= \sum_{\ell=1}^{\infty} \frac{2\ell+1}{\ell(\ell+1)}\left[a_\ell \tau_\ell + b_\ell \pi_\ell\right] \end{aligned} \tag{20}$$

In Eq. (20) a_ℓ and b_ℓ, which are the Mie coefficients, are given by

$$a = \frac{\psi_\ell'(mx)\psi_\ell(x) - m\psi_\ell(mx)\psi_\ell'(x)}{\psi_\ell'(mx)\zeta_\ell(x) - m\psi_\ell(mx)\zeta_\ell'(x)} \tag{21}$$

$$b = \frac{m\psi_\ell'(mx)\psi_\ell(x) - \psi_\ell(mx)\psi_\ell'(x)}{m\psi_\ell'(mx)\zeta_\ell(x) - \psi_\ell(mx)\zeta_\ell'(x)} \tag{22}$$

where m and x, respectively, are the complex refractive index and size parameters—that is, $m = m_1 - im_2$ and $x = 2\pi r/\lambda$ when r is the particle radius. The functions ψ_ℓ and ζ_ℓ are the Riccati-Bessel functions, and a prime indicates differentiation with respect to the argument. The π_ℓ and τ_ℓ functions are given by

$$\pi_\ell(\cos\chi) = \frac{dP_\ell(\cos\chi)}{d\cos\chi} \tag{23}$$

and

$$\tau_\ell(\cos\chi) = \cos\chi\,\pi_\ell(\cos\chi) - \sin\chi\frac{d\pi_\ell(\cos\chi)}{d\cos\chi} \tag{24}$$

where $P_\ell(\cos\chi)$ is a Legendre polynomial. The scattering cross-section is

$$\sigma_s(\lambda, r, m) = \pi r^2 Q_s(x, m) = \frac{\lambda^2}{2\pi}\sum_{\ell=1}^{\infty}(2\ell+1)\left[|a_\ell|^2 + |b_\ell|^2\right] \tag{25}$$

where $Q_s(x, m)$ is called the scattering efficiency factor. The total (scattering plus absorption) cross-section is

$$\sigma_t(\lambda, r, m) = \pi r^2 Q_t(x, m) = \frac{\lambda^2}{2\pi}\sum_{\ell=1}^{\infty}(2\ell+1)\mathrm{Re}(a_\ell + b_\ell) \tag{26}$$

where $Q_t(x, m)$ is the total eifficiency factor. Likewise, the absorption cross-section is then

$$\sigma_a(\lambda, r, m) = \sigma_t(\lambda, r, m) - \sigma_s(\lambda, r, m) \tag{27}$$

with a corresponding efficiency factor $Q_a(x, m)$. As in the Rayleigh case, a scattering phase function can be defined:

$$P(\cos\chi) = \frac{1}{2\pi x^2 Q_s(x, m)}\left[|S_1|^2 + |S_2|^2\right] \tag{28}$$

Calculating all the functions given above for various refractive indices and size parameters is quite involved. Nevertheless, computer programs have been written which allow the performance o this analysis. Having obtained a program written by J. V. Dave, we used it to

calculate the cross-sections and phase functions. For example, we have calculated the scattering efficiency factor for homogeneous spheres of refractive indices m = 1.29, 1.29 - 0.0465i, and 1.28 - 1.37i. The results are shown in Fig. 4. It should be noted that the efficiency factor is greatest for the real index (that is, when there is no absorption) and decreases with increasing imaginary index. The absorption efficiency factor has also been calculated for m = 1.28 - 0.0465i and 1.28 - 1.37i. Here the efficiency factor is large for a high imaginary index and small particles, as illustrated in Fig. 5. Finally, the total efficiency factor is shown in Fig. 6 for the same set of refractive indices. Thus, it can be seen that efficiency factors vary strongly for different refractive indices and size parameters.

4.2 ATTENUATION COEFFICIENTS

Knowing the cross-sections, one can then calculate the scattering, absorption, and extinction coefficients by multiplying the cross-sections by the particle number density. For real atmospheric conditions characterized by haze, fogs, and dusts, there is a distribution of particle sizes. (One distribution, characterized in Section 3.1.2, is the modified gamma distribution.) Thus, for a polydispersion, one must integrate over particle size to obtain the absorption, scattering, and extinction coefficients:

$$\alpha_A(\lambda, m, z) = \int_0^\infty \sigma_{a,A}(\lambda, m, r) n(z, r)\, dr \tag{29}$$

$$\beta_A(\lambda, m, z) = \int_0^\infty \sigma_{s,A}(\lambda, m, r) n(z, r)\, dr \tag{30}$$

$$\kappa_A(\lambda, m, z) = \int_0^\infty \sigma_{t,A}(\lambda, m, r) n(z, r)\, dr \tag{31}$$

where α, β, and κ denote absorption, scattering, and extinction coefficients

A designates aerosol

$n(z, r)$ is the aerosol-particle number density at altitude z for particles in size range Δr at size r

The number density is normalized as follows:

$$N(z) = \int_0^\infty n(z, r)\, dr \tag{32}$$

where n(z) is just the total number density. Likewise, the corresponding coefficients for molecular scattering can be found. The scattering cross-section is given by Eq. (16), and the absorption cross-section is usually taken to be that for ozone in the visible spectral region. Thus, we have for the complete atmosphere:

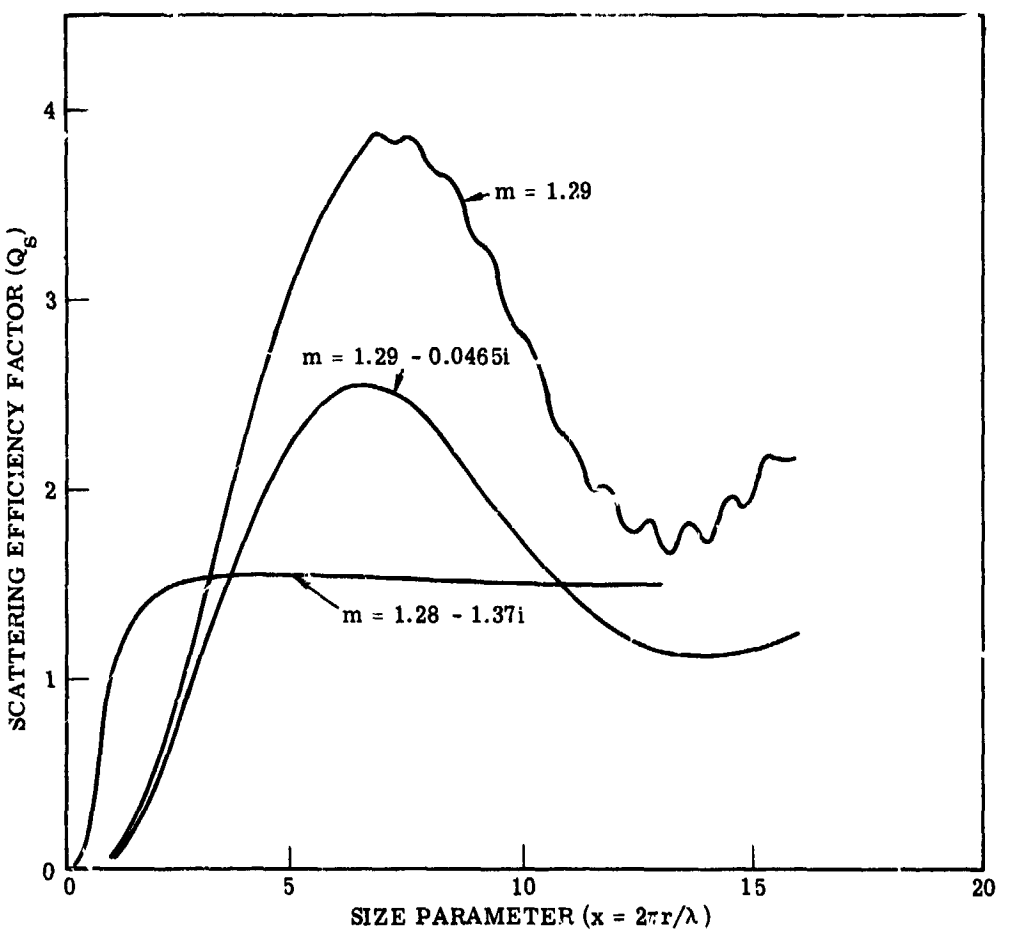

FIGURE 4. SCATTERING EFFICIENCY FACTOR FOR HOMOGENEOUS SPHERES OF COMPLEX REFRACTIVE INDEX m

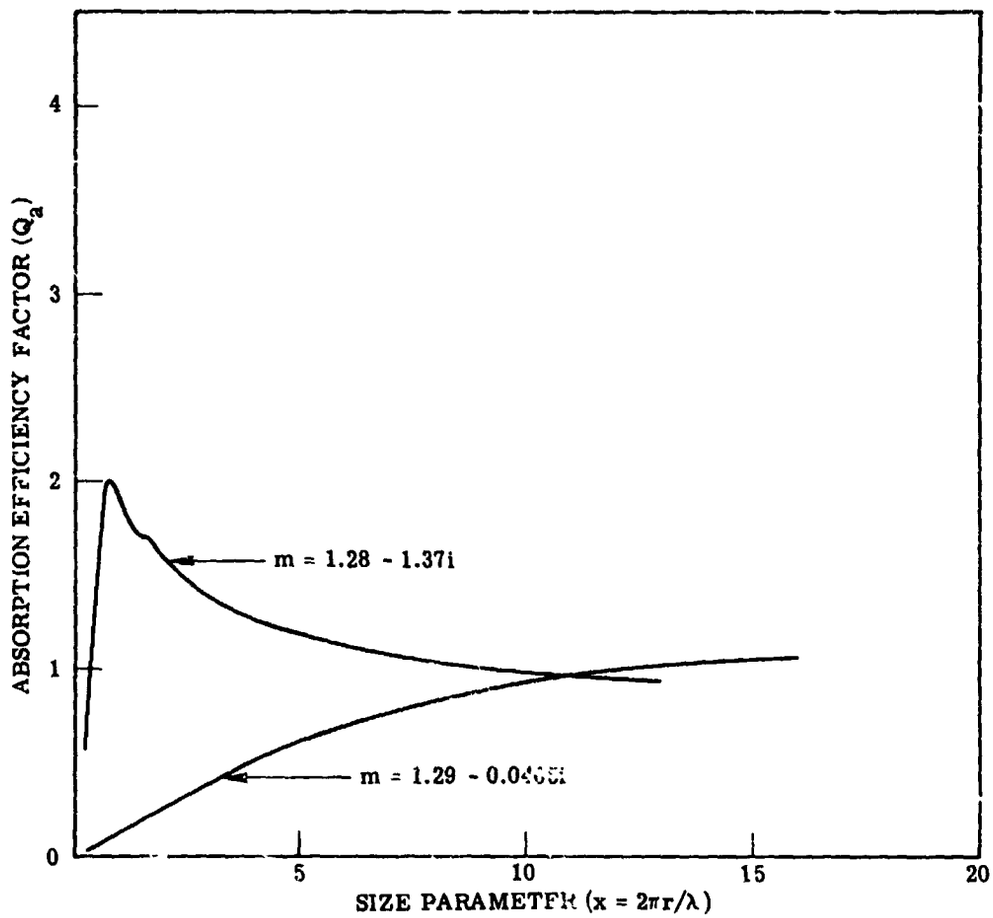

FIGURE 5. ABSORPTION EFFICIENCY FACTOR FOR HOMOGENEOUS SPHERES OF COMPLEX REFRACTIVE INDEX m

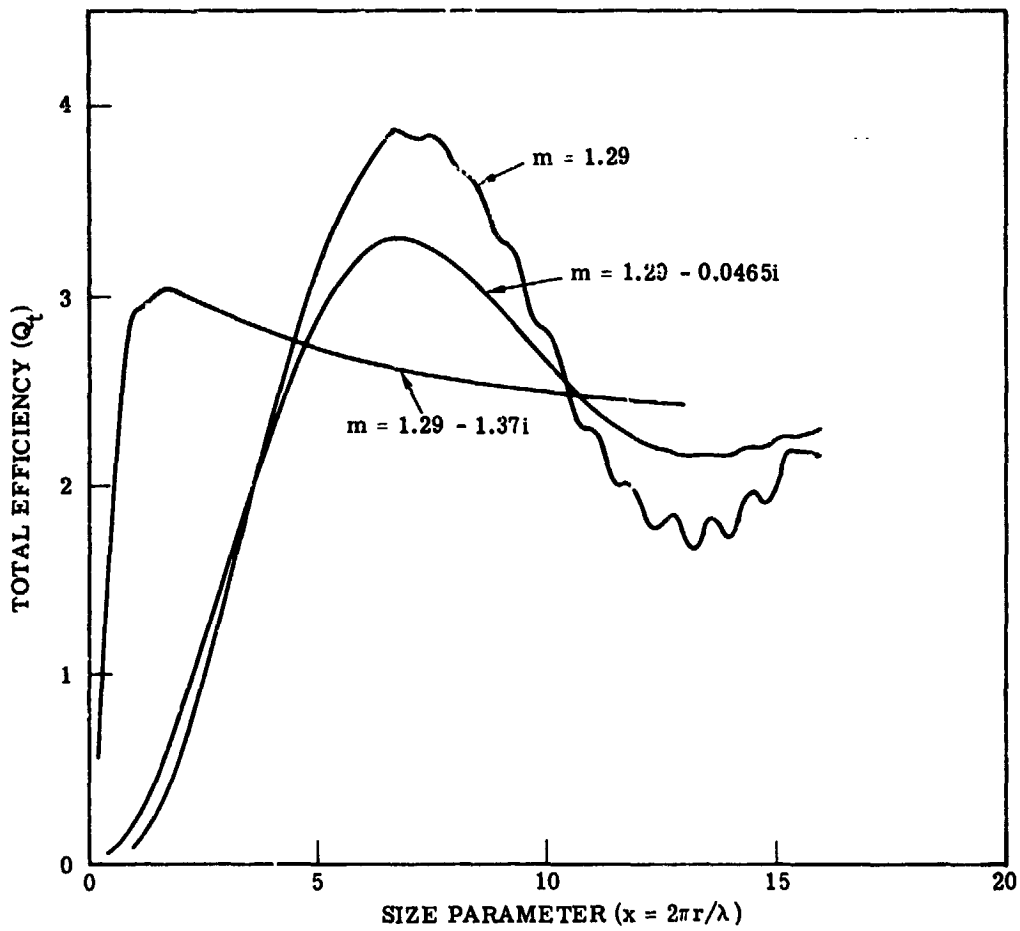

FIGURE 6. TOTAL EFFICIENCY FACTOR FOR HOMOGENEOUS SPHERES OF COMPLEX REFRACTIVE INDEX m

$$\alpha(\lambda, m, s, z) = \alpha_R(\lambda, z) + \alpha_A(\lambda, m, s, z) \tag{33}$$

$$\beta(\lambda, m, s, z) = \beta_R(\lambda, z) + \beta_A(\lambda, m, s, z) \tag{34}$$

$$\kappa(\lambda, m, s, z) = \kappa_R(\lambda, z) + \kappa_A(\lambda, m, s, z) \tag{35}$$

where we have shown the explicit dependence on a complex refractive index m and a particular size distribution s.

It is sometimes useful to deal with an average cross-section for aerosols. Assuming that the size distribution is altitude-independent, we can write Eqs. (29), (30), and (31) as

$$\alpha_A(\lambda, m, z) = N(z)\bar{\alpha}_{a,A}(\lambda, m) \tag{36}$$

$$\beta_A(\lambda, m, z) = N(z)\bar{\sigma}_{s,A}(\lambda, m) \tag{37}$$

$$\kappa_A(\lambda, m, z) = N(z)\bar{\sigma}_{t,A}(\lambda, m) \tag{38}$$

where

$$\bar{\sigma}_{i,A}(\lambda, m) = \int_0^\infty \sigma_{i,A}(\lambda, m, r)\psi(r)\,dr \tag{39}$$

in which the function $\psi(r)$ is normalized to 1 and the index i can indicate a, s, or t. We have computed many values of the average cross-sections for homogeneous spheres of various refractive indices and size distributions. The results of this analysis will be presented later.

4.3 OPTICAL DEPTH

For radiative-transfer calculations it is usually more meaningful to deal with the dimensionless quantity, optical depth in a medium, rather than with actual distances. We define optical depth as

$$\tau(\lambda, h) = \int_h^\infty \kappa(\lambda, z)\,dz \tag{40}$$

and optical thickness as

$$\tau_0(\lambda) = \int_0^\infty \kappa(\lambda, z)\,dz \tag{41}$$

where h is some definite altitude. Thus, at the top of the atmosphere $\tau(\lambda, h{\to}\infty) = 0$, while at the bottom $\tau(\lambda, h{=}0) = \tau_0(\lambda)$. Optical depth can be thought of as the distance into a medium expressed in units of mean free photon paths. A small τ_0 indicates that little attenuation takes

place, whereas a large τ_0 means that the atmosphere is either strongly absorbing or scatters much of the radiation. Optical depths can easily be obtained for Rayleigh atmospheres. Elterman [27] has tabulated the results for all altitudes from 0 to 50 km and for selected wavelengths from 0.27 μm to 4.00 μm. The optical thickness varies from 1.928 at 0.27 μm to 0.001 at 1.67 μm.

Likewise, if the extinction coefficient for aerosols is available, the corresponding aerosol optical depths can be determined. By analyzing many experimentally determined aerosol profiles, Elterman [28] has calculated the extinction coefficients and optical depths for realistic atmospheric conditions. For a 2-km visual range, the aerosol optical thickness is 2.521 at 0.36 μm and 1.053 at 0.90 μm. These results indicate that multiple scattering occurs in Earth's atmosphere since the mean free photon paths are short compared to the actual distances traveled.

4.4 SINGLE-SCATTERING ALBEDO

A very important parameter in radiative-transfer analysis is the single-scattering albedo, defined as

$$\omega_0(\lambda, m, s, z) \equiv \frac{\beta_R(\lambda, z) + \beta_A(\lambda, m, s, z)}{\kappa(\lambda, m, s, z)} \tag{42}$$

where $\kappa(\lambda, m, s, z)$ is the total (Rayleigh plus aerosol) extinction coefficient. The albedo $\omega_0(\lambda, m, s, z)$ is the fraction of scattering which can occur. Thus, if there is neither aerosol absorption nor ozone absorption, then $\omega_0(\lambda, m, s, z) = 1$ and we have a pure scattering atmosphere. For strongly absorbing aerosols, however, $\beta_A(\lambda, m, s, z)$ is small and $\omega_0(\lambda, m, s, z)$ can be as small as 0.09.

In order to construct model atmospheres simulating various degrees of contamination resulting from polluted air masses or varying weather conditions, we shall do the following: (1) use Elterman's values of the total extinction coefficient $\kappa(\lambda, z)$ corresponding to various visibility conditions; (2) calculate from the Mie scattering theory the average cross-sections for several realistic refractive indices and size distributions, and (3) use these results to calculate the single-scattering albedo.

We can define an aerosol absorptivity parameter f as follows:

$$f \equiv \frac{\alpha_A(\lambda, m, s, z)}{\kappa_A(\lambda, m, s, z)} = \frac{N(z)\bar{\sigma}_{a,A}(\lambda, m, s)}{N(z)\bar{\sigma}_{t,A}(\lambda, m, s)} = \frac{\bar{\sigma}_{a,A}(\lambda, m, s)}{\bar{\sigma}_{t,A}(\lambda, m, s)} \tag{43}$$

Also, since

$$f = 1 - \frac{\beta_A(\alpha, m, s, z)}{\kappa_A(\lambda, m, s, z)} \tag{44}$$

we have

$$\omega_o(\lambda, m, s, z) = \frac{\beta_R(\lambda, z) + (1 - f)\kappa_A(\lambda, m, s, z)}{\kappa(\lambda, V, z)} \tag{45}$$

which reduces to

$$\omega_o(\lambda, m, s, V, z) = \frac{f\beta_R(\lambda, z) - (1 - f)\alpha_R(\lambda, z)}{\kappa(\lambda, V, z)} + 1 - f \tag{46}$$

Thus, we have the single-scattering albedo for a realistic atmosphere in terms of wavelength λ, refractive index m, size distribution parameter s, horizontal visual range V, and altitude z. It is interesting to consider special cases. If there is no aerosol absorption, $\alpha_A = 0$ and $f = 0$ or

$$\omega_o(\lambda, V, z) = 1 - \frac{\alpha_R(\lambda, z)}{\kappa(\lambda, V, z)} \tag{47}$$

If there is no gaseous absorption, $\alpha_R = 0$ and

$$\omega_o(\lambda, m, s, V, z) = 1 - f\left(1 - \frac{\beta_R(\lambda, z)}{\kappa(\lambda, V, z)}\right) \tag{48}$$

If there is no aerosol scattering, $\beta_A = 0$, $f = 1$ and

$$\omega_o(\lambda, V, z) = \frac{\beta_R(\lambda, z)}{\kappa(\lambda, V, z)} \tag{49}$$

Finally, if there is no gaseous scattering, $\beta_R = 0$ and

$$\omega_o(\lambda, m, s, V, z) = (1 - f)\left(1 - \frac{\alpha_R(\lambda, z)}{\kappa(\lambda, V, z)}\right) \tag{50}$$

The Mie scattering computer program was run to obtain values of $\bar{\sigma}_{a,A}(\lambda, m, s)$ and $\bar{\alpha}_{t,A}(\lambda, m, s)$, from which the aerosol absorptivity f was calculated. This was done for Deirmendjian's haze L (continental) and haze M (maritime), as well as for complex refractive indices of the following:

$$m = \begin{cases} 1.5 \\ 1.5 - 0.01i \\ 1.5 - 0.10i \\ 1.5 - 1.00i \\ 1.5 - \infty i \end{cases}$$

These correspond to all degrees of absorption by aerosols, from no absorption at $m = 1.5$ to complete absorption at $m = 1.5 - \infty i$. For the former, $f = 0$, and for the latter, $f = 1$. Figure 7 illustrates the spectral dependence of absorptivity for various refractive indices and hazes. To get "exact" values of cross sections using the Mie scattering program, one would have to

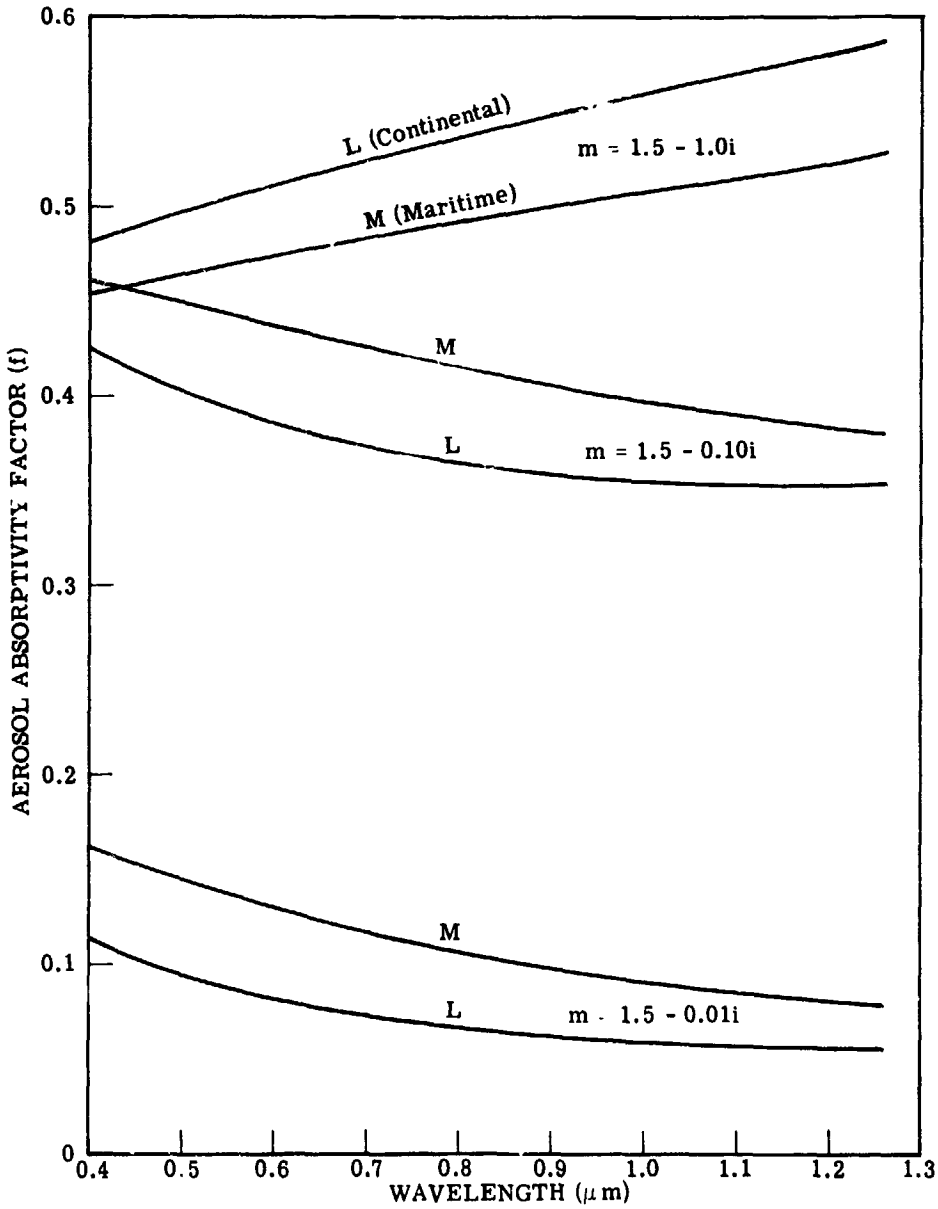

FIGURE 7. DEPENDENCE OF THE AEROSOL ABSORPTIVITY PARAMETER, f, ON WAVELENGTH FOR HAZES L AND M WITH THREE REFRACTIVE INDICES

run the program infinitely long. However, sufficiently accurate values can be obtained after a reasonable amount of calculation since the values tend to an asymptote. Our program was run until the fixed values had only a few percent change as a function of the size parameter x. Details of the computational procedure can be found in Deirmendjian [10].

We can now calculate the single-scattered albedo as a function of wavelength for various size distributions, refractive indices, altitudes, and visual ranges. Figure 8 illustrates the spectral dependence of ω_0 for five altitudes. This is for a refractive index of 1.5, that is, no aerosol absorption. At the surface, ω_0 is unity because the ozone contribution is very small. However, as we go up in the atmosphere, the ozone absorption band near 0.6 μm becomes quite evident. Figure 9 illustrates the same effect for a heavily contaminated atmosphere with high absorption. Here ω_0 is only about 0.5 near the surface, increasing slightly as we go higher into the atmosphere. The low value of ω_0 near the surface is the result of strong aerosol absorption in the dense lower troposphere.

To see the effects of aerosol and ozone absorption throughout the entire atmosphere, we will look at altitude profiles of ω_0. Figure 10 shows the profile for a hypothetical atmosphere, both with no aerosol absorption and with the maximum absorption. Aerosol absorption is especially pronounced in the lower troposphere, and the relatively strong ozone absorption occurring at higher altitudes is quite evident.

The profiles for various wavelengths are portrayed in Fig. 11 for a dense haze. This case represents the maximum amount of absorption (aerosol and ozone) which can occur. It should be noted that in the lower troposphere most absorption occurs at the longer wavelengths, since aerosol absorption increases with wavelength beyond a certain point (as was seen in Fig. 7). At higher altitudes, however, the ozone band near 0.6μm dominates. Figure 12 shows the same effect except that the case is one of no aerosol absorption.

We now turn to the more realistic conditions of partial aerosol absorption. Figure 13 illustrates the altitude profile for three refractive indices: m = 1.5 - 0.01i, or little absorption; m = 1.5 - 0.10i, moderate absorption; and m = 1.5 - 1.0i, heavy absorption. Note that there is quite a variation in ω_0 in the lower troposphere.

The altitude profile for ω_0 in the first 5 km is shown in Fig. 14 for the two hazes L and M and for various amounts of absorption. Varying the size distribution seems to have only a minor effect on the profile, as opposed to changes in the imaginary part of the refractive index.

Finally, we can see the effects of a change in visual range on the single scattering albedo ω_0. Figure 15 shows that ω_0 is essentially constant as a function of visual range for a given haze, increasing rapidly as the amount of aerosol decreases. As any haze (contaminated or

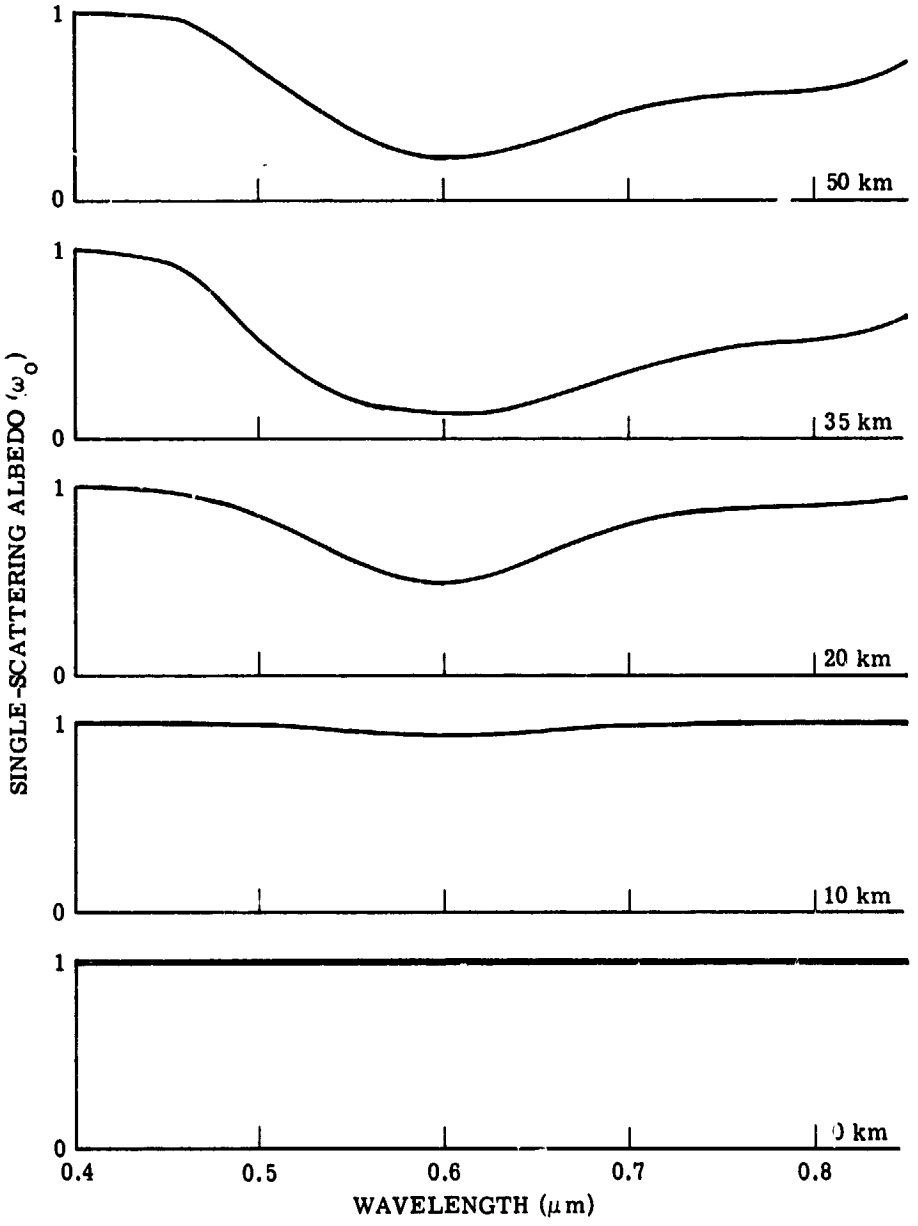

FIGURE 8. DEPENDENCE OF SINGLE-SCATTERING ALBEDO ON WAVELENGTH FOR VARIOUS ALTITUDES—REFRACTIVE INDEX m = 1.5. Visual range = 2 km, haze L.

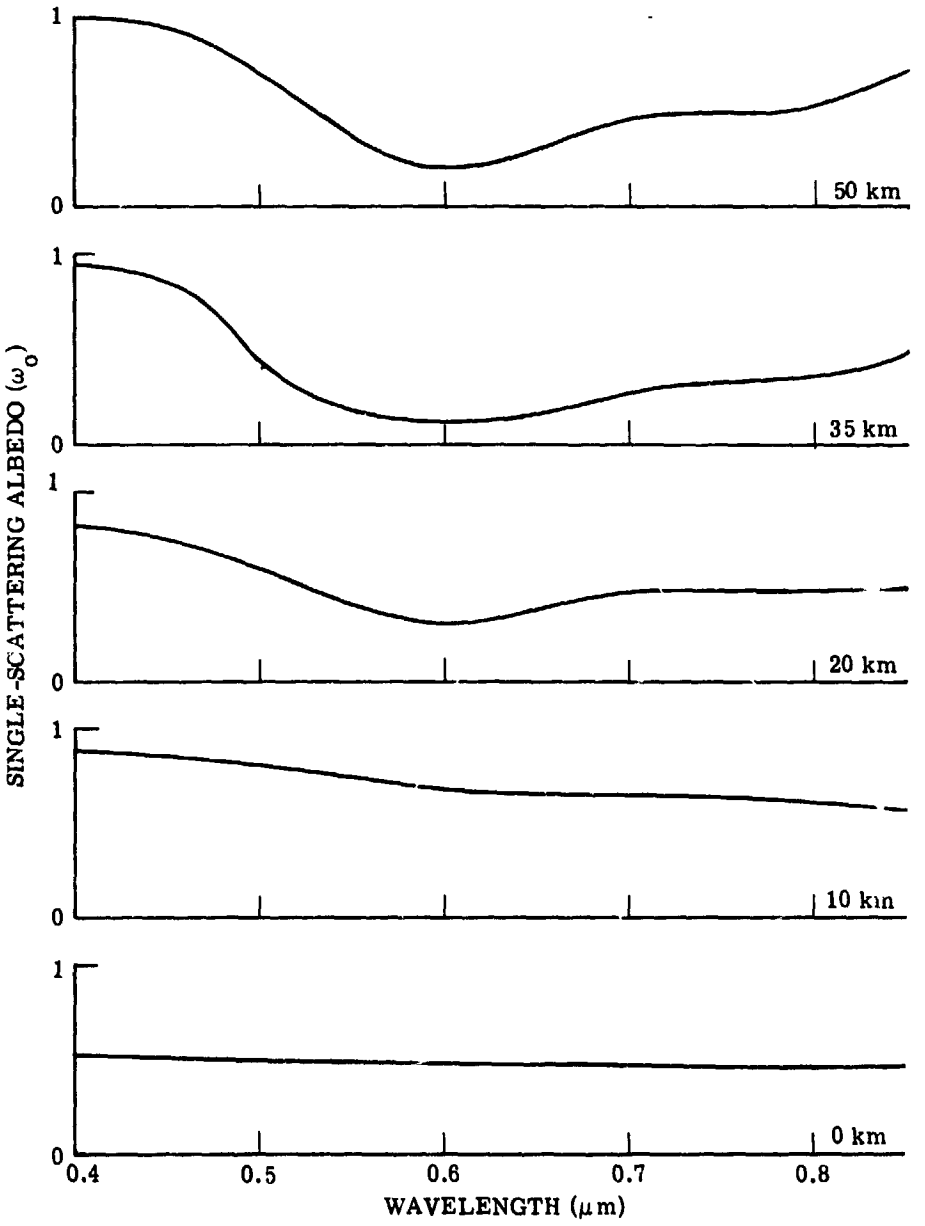

FIGURE 9. DEPENDENCE OF SINGLE-SCATTERING ALBEDO ON WAVELENGTH FOR VARIOUS ALTITUDES—COMPLEX REFRACTIVE INDEX m = 1.5 - 1.0i. Visual range = 2 km, haze L.

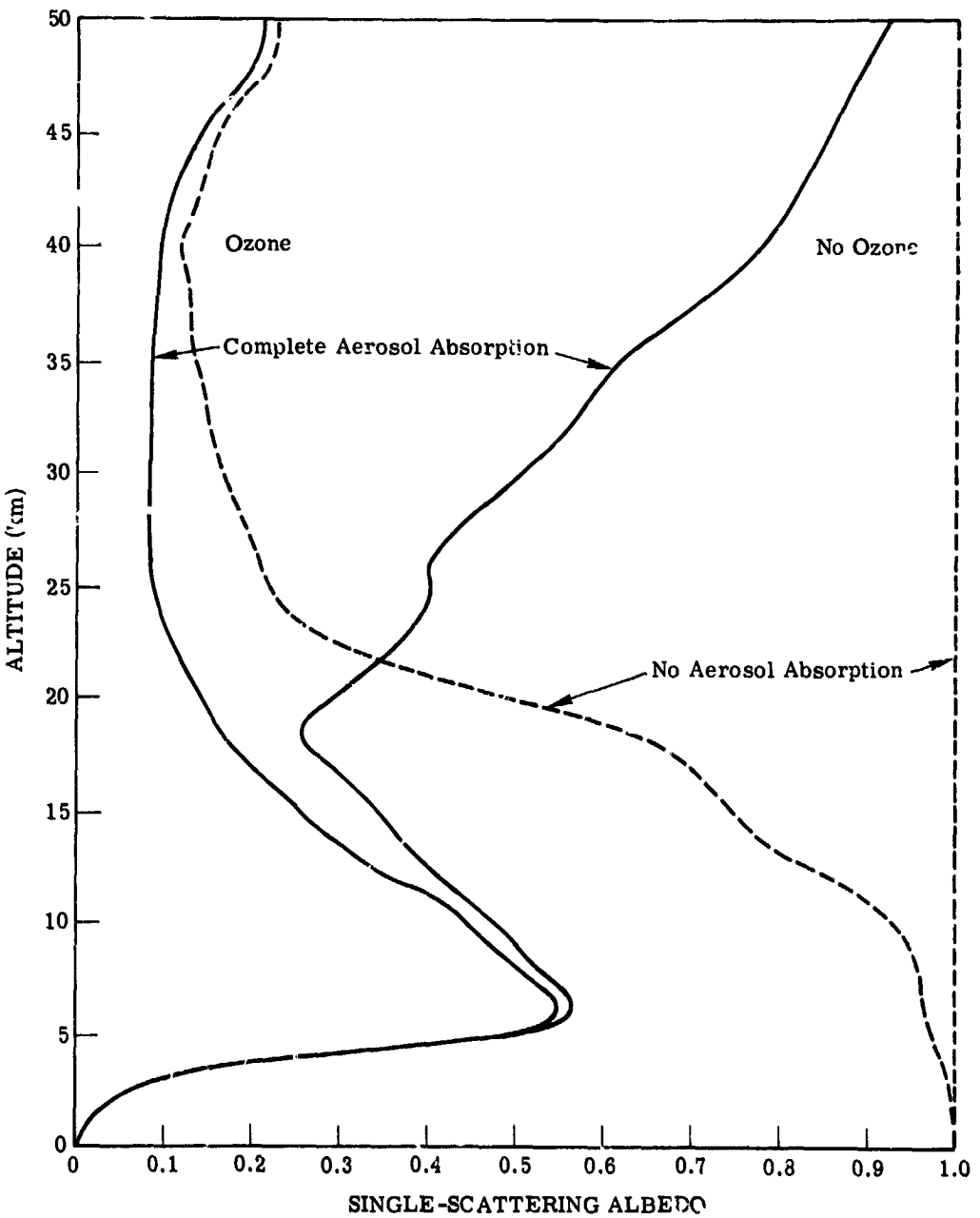

FIGURE 10. ALTITUDE PROFILE OF THE SINGLE-SCATTERING ALBEDO WITH AND WITHOUT OZONE. Wavelength = 0.6μm.

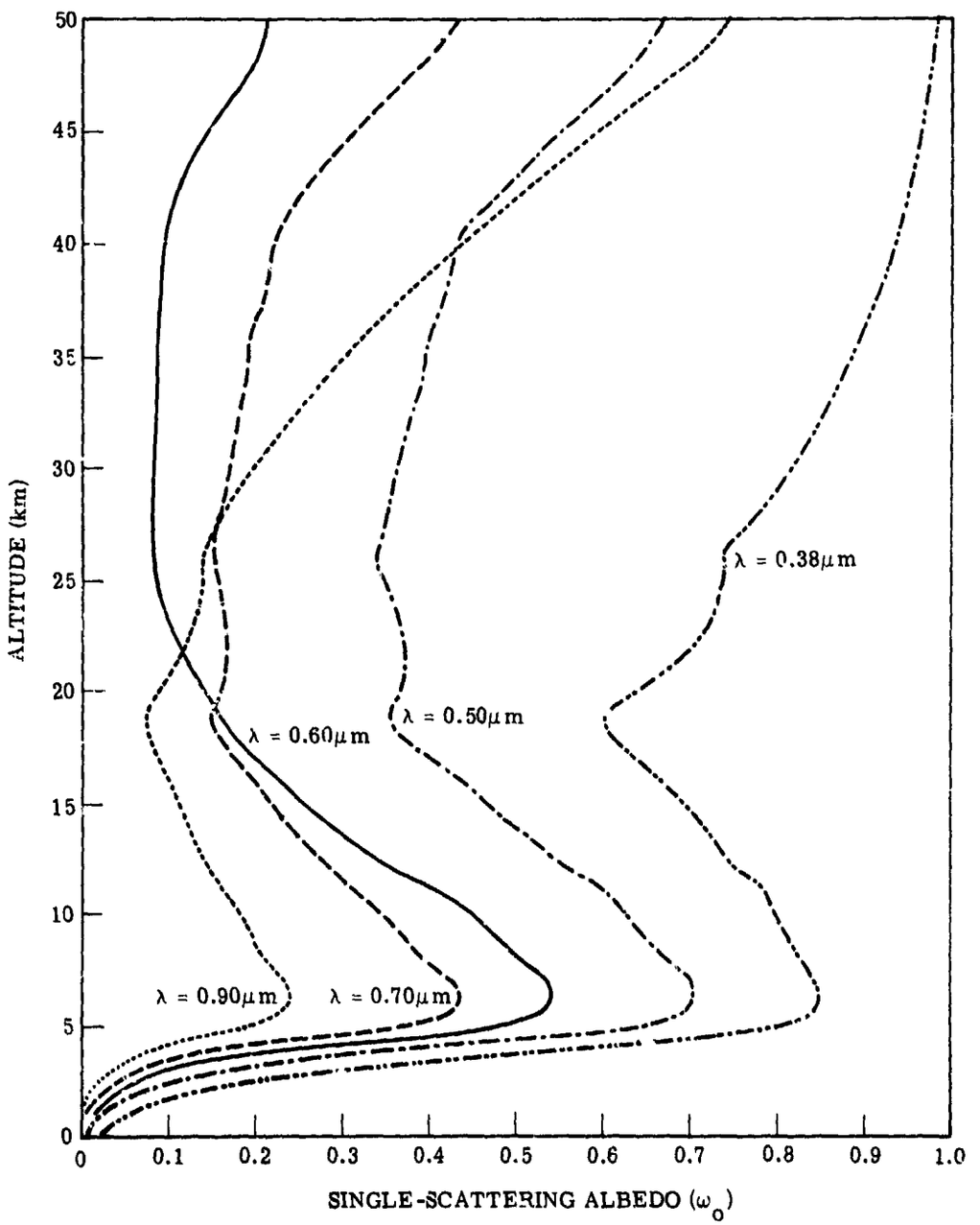

FIGURE 11. ALTITUDE PROFILE OF THE SINGLE-SCATTERING ALBEDO WITH COMPLETE AEROSOL ABSORPTION. Visual range = 2 km.

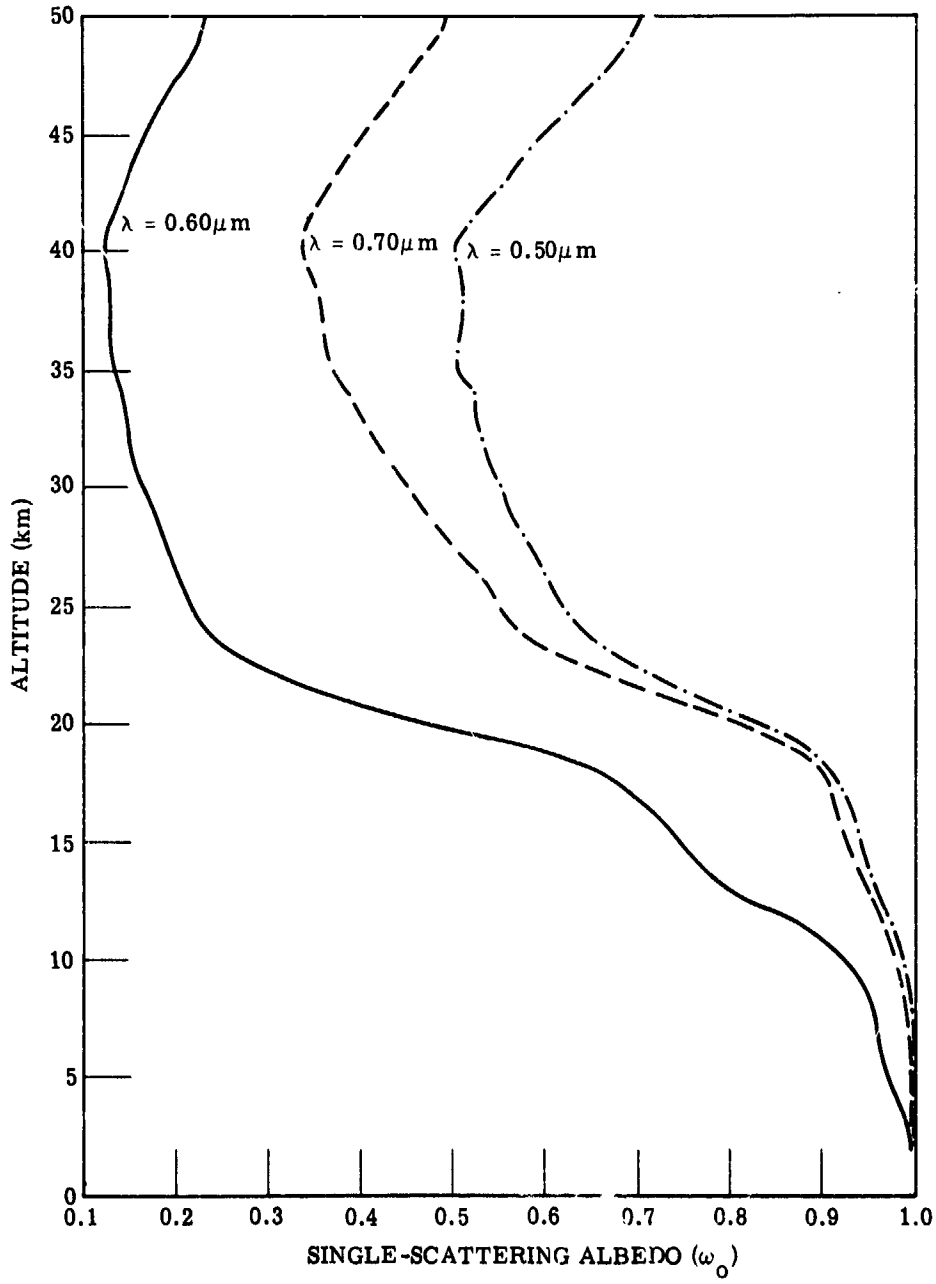

FIGURE 12. ALTITUDE PROFILE OF THE SINGLE-SCATTERING ALBEDO WITH NO AEROSOL ABSORPTION. Visual range = 2 km.

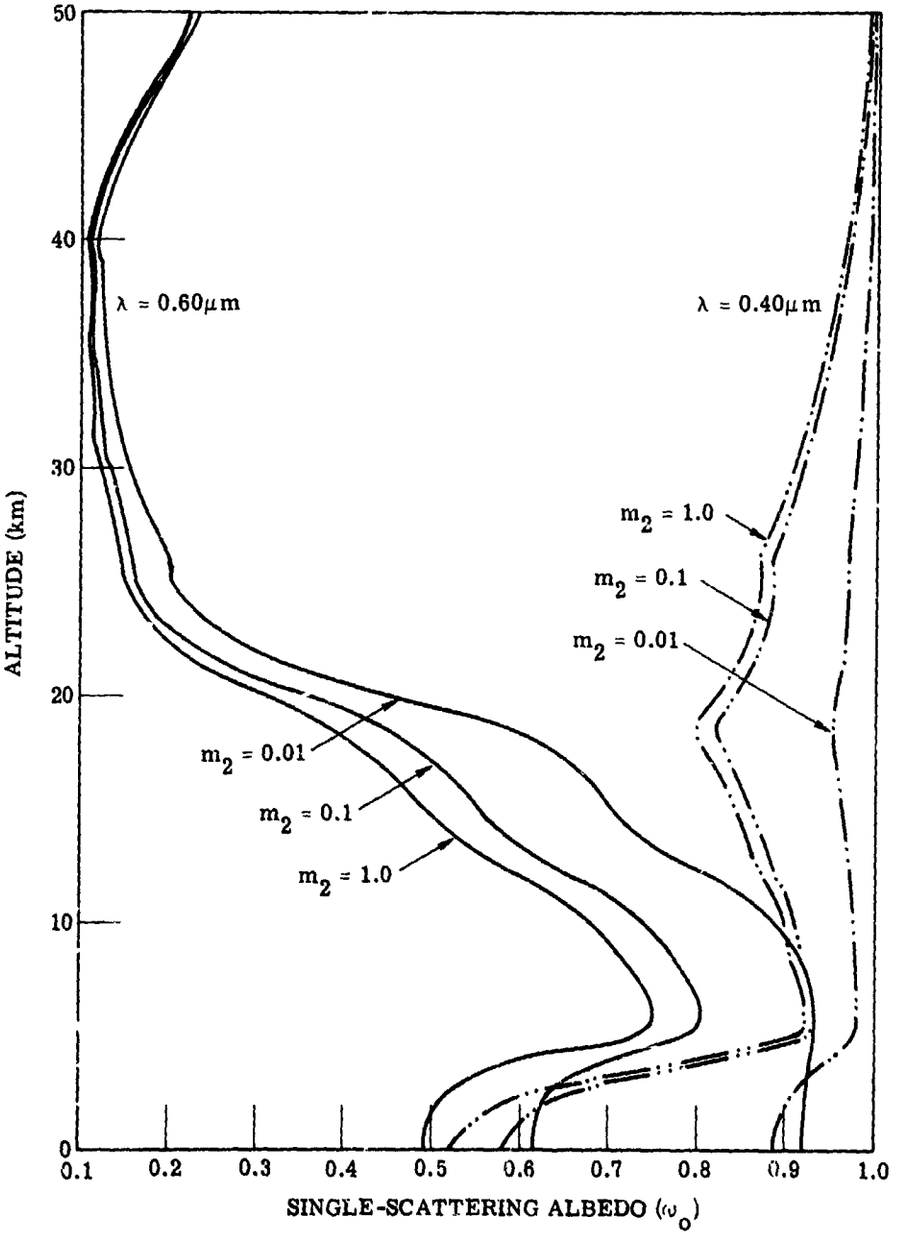

FIGURE 13. ALTITUDE PROFILE OF THE SINGLE-SCATTERING ALBEDO FOR HAZE L. Visual range = 2 km, complex refractive index m = 1.5 - im_2.

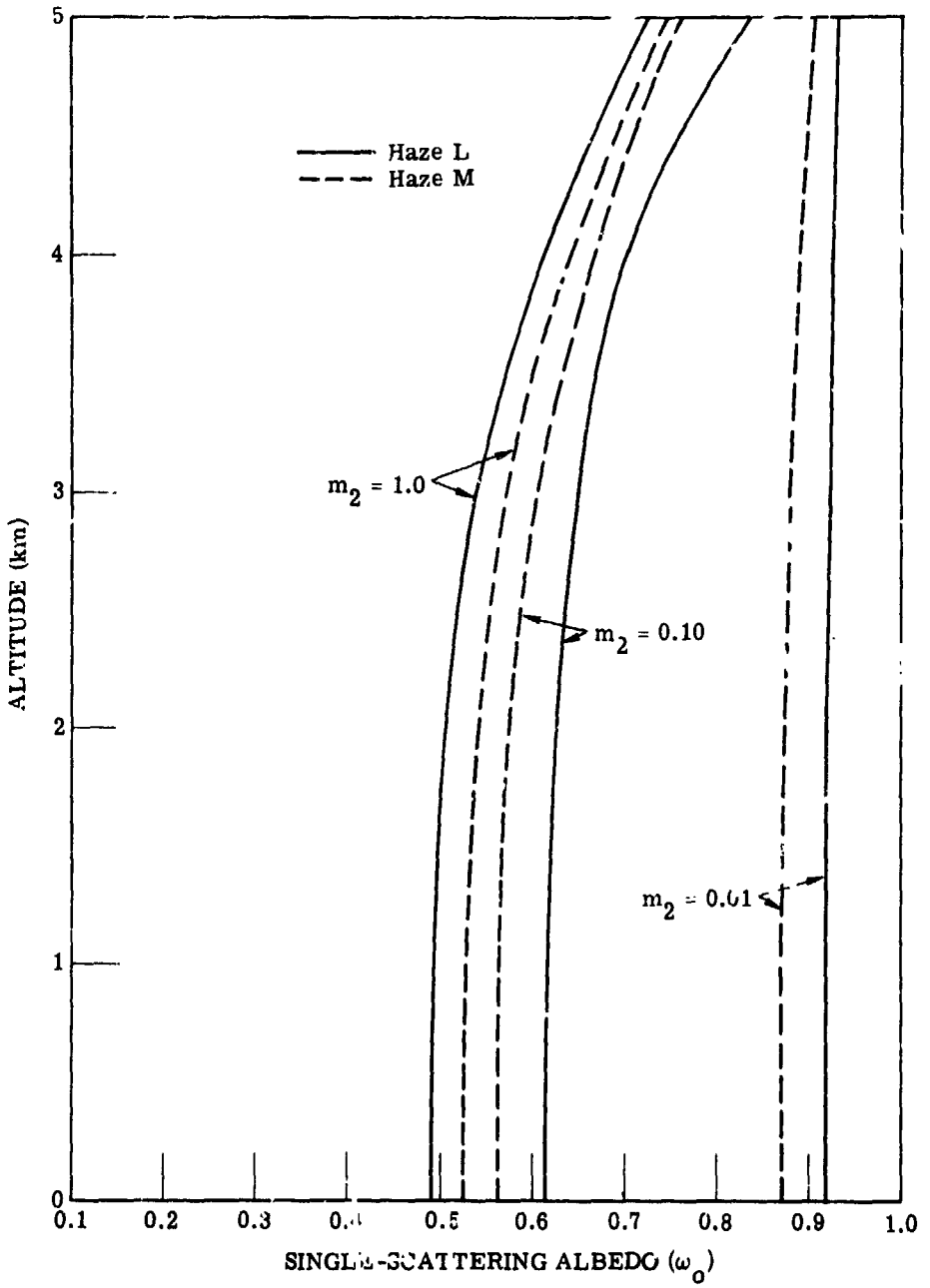

FIGURE 14. ALTITUDE PROFILE OF THE SINGLE-SCATTERING ALBEDO IN THE LOWER TROPOSPHERE. Wavelength = 0.6μm, complex refractive index m = 1.5 - im_2, visual range = 2 km.

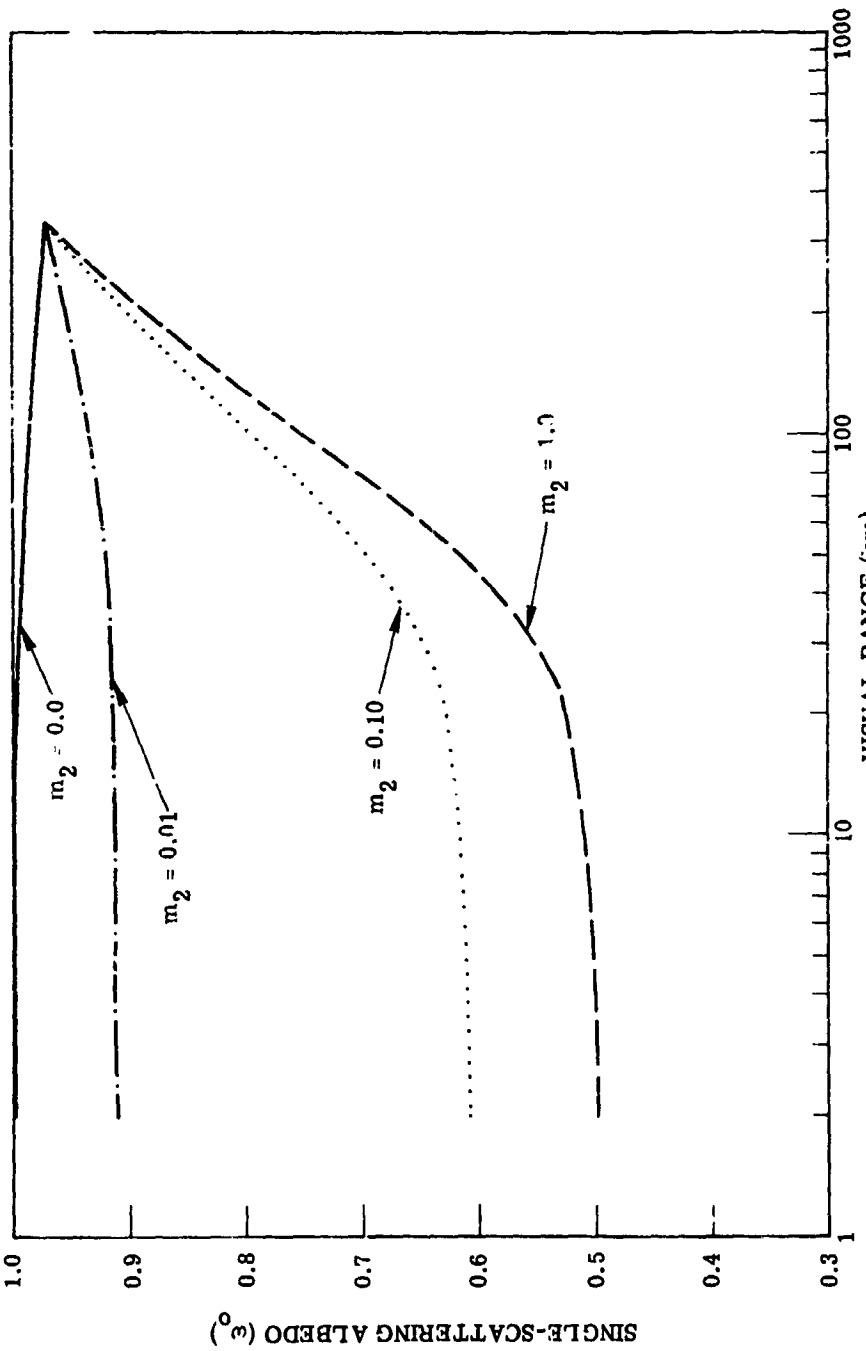

FIGURE 15. DEPENDENCE OF THE SINGLE-SCATTERING ALBEDO ON VISUAL RANGE. Wavelength = 0.55 μm, altitude = 0 km, complex refractive index m = 1.5 - im_2.

not) decreases, the albedo ω_o approaches one characterizing a pure, aerosol-free Rayleigh atmosphere. It is clear that the dominant effect results from a change in refractive index.

4.5 SCATTERING PHASE FUNCTIONS

Besides optical depth and the single-scattering albedo, the radiation field within the atmosphere depends strongly on the single-scattering phase function. Assuming spherical particles, we have used the Mie theory to calculate phase functions for various refractive indices, wavelengths, and size distributions. Figure 16 illustrates the dependence of the phase function on the imaginary part of the refractive index. It is interesting to note that for little or no absorption there is the usual peak in the backward direction. For strong absorption, however, the backward peak disappears and the distribution becomes more anisotropic.

The wavelength-dependence of the phase function is exhibited in Fig. 17 for a weakly absorbing aerosol. The dependence is as one might expect from elementary scattering theory. For shorter wavelengths the function is more peaked than for longer wavelengths. This is also true for the backward part of the function.

The effect of varying particle size distribution can be seen in Fig. 18 for aerosols with no absorption. As in the case of single-scattering albedo, the predominant effect comes not from size distribution but from composition.

Tables of the scattering phase functions for 13 wavelengths, 10 visual ranges, 4 refractive indices, 2 hazes, and a complete range of altitudes from 0 to 50 km have been formulated for use in computer programs to calculate the radiation field. The implementation of these results in our radiative-transfer studies will be presented in Section 5.

To sum up, we can calculate the important basic optical parameters for an atmosphere characterized by scattering and absorbing, spherical aerosol-particles, and by ozone absorption. The single-scattering albedo can be calculated for any refractive index and particle size distribution, and we can model any kind of vertically inhomogeneous atmosphere. Likewise, single-scattering phase functions can be calculated for any composition and size distribution. However, for inhomogeneous, non-spherical particles, actual experimental data on the attenuation coefficients and phase functions must be used.

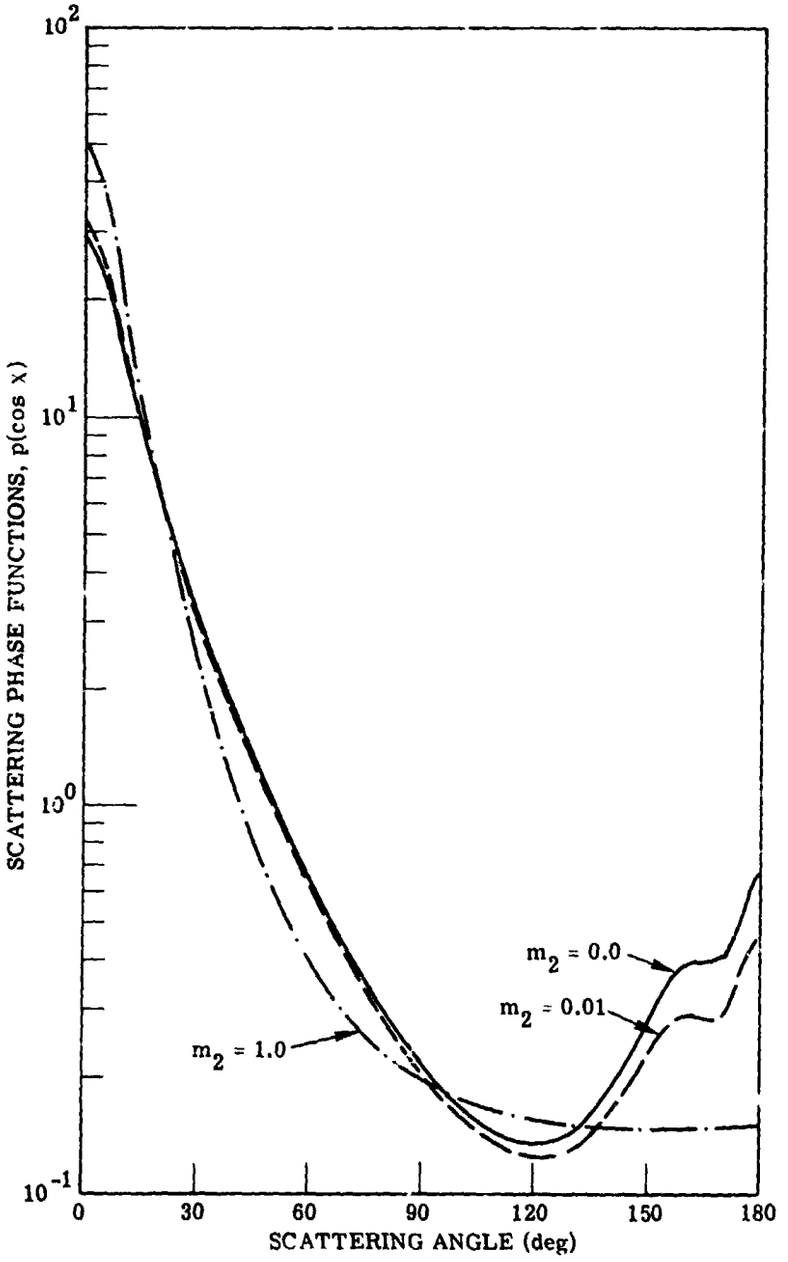

FIGURE 16. SCATTERING PHASE FUNCTIONS AS CALCULATED FROM MIE THEORY FOR HAZE L—COMPLEX REFRACTIVE INDEX m = 1.5 - im_2. Wavelength = 0.55μm.

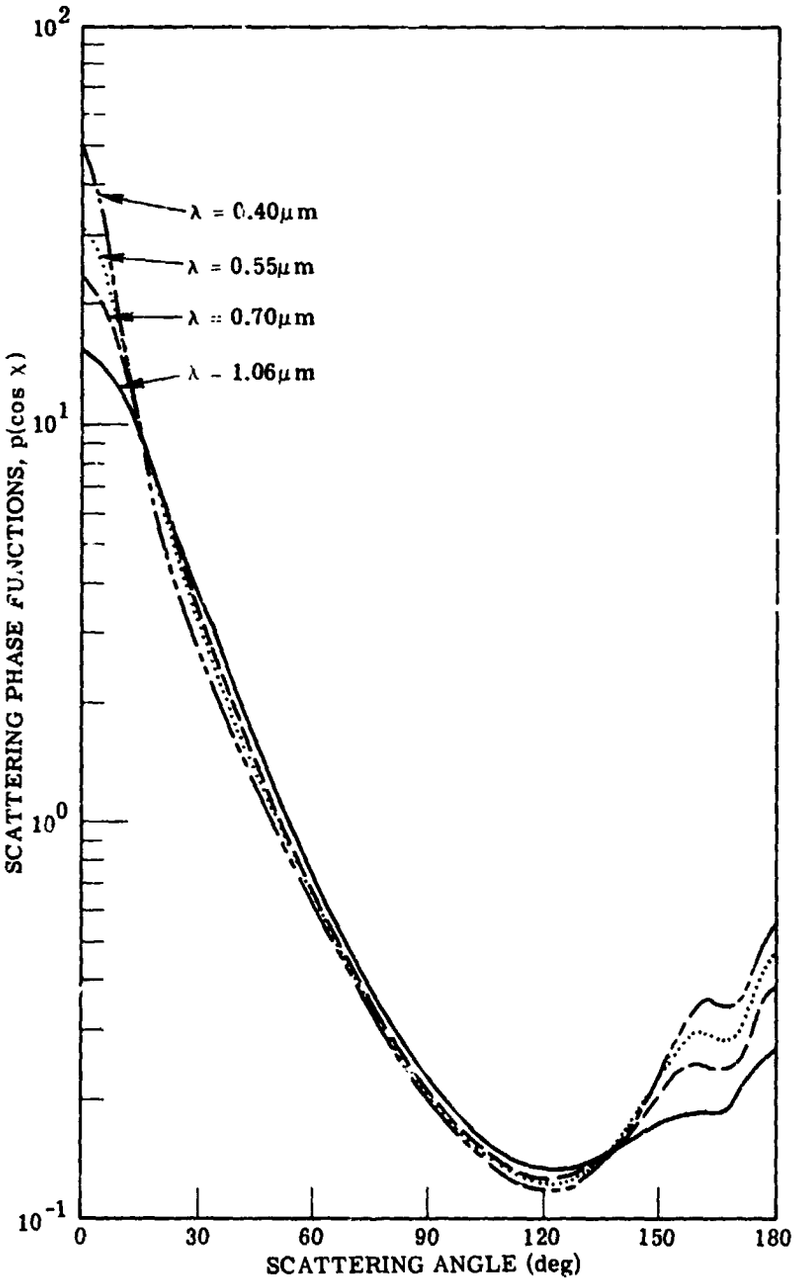

FIGURE 17. SCATTERING PHASE FUNCTIONS AS CALCULATED FROM MIE THEORY FOR HAZE L—COMPLEX REFRACTIVE INDEX m = 1.5 - 0.01i.

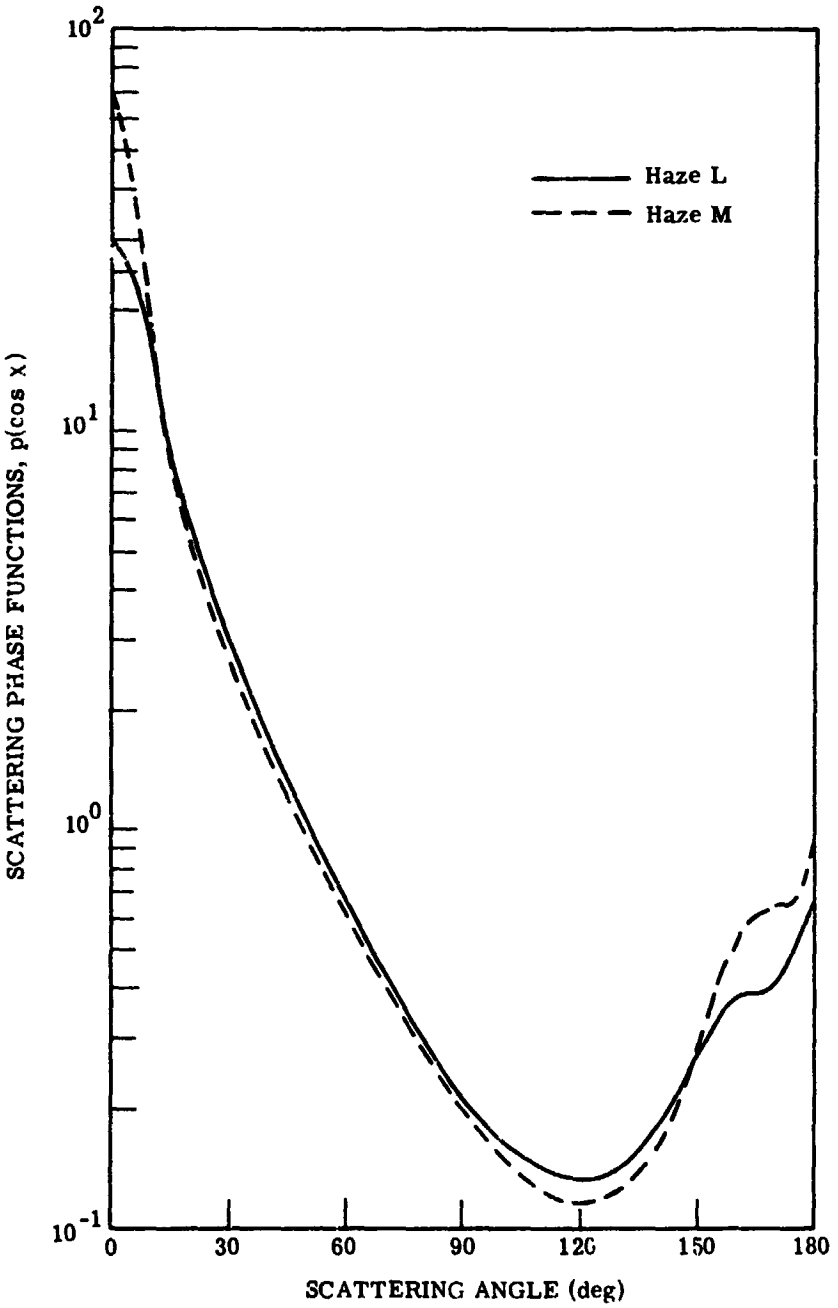

FIGURE 18. SCATTERING PHASE FUNCTIONS AS CALCULATED FROM MIE THEORY FOR HAZE L AND HAZE M. Wavelength = 0.55μm, complex refractive index m = 1.5.

5
INHOMOGENEOUS ATMOSPHERES

We now consider the case of a layered atmosphere in which each layer is homogeneous with regard to atmospheric optical parameters. More exact formulations [29] involving perturbation techniques have dealt with the general inhomogeneous Rayleigh atmosphere, but no one has solved the general problem for anisotropic scattering.

5.1 THE DOUBLE-DELTA APPROXIMATION

The one-dimensional, radiative-transfer equation can be approximately solved for highly anisotropically scattering atmospheres by using the so-called double-delta approximation [30, 31, 32]. The resulting equations, however, are different for $\omega_o \neq 1$, becoming

$$\frac{dE'_+(\tau)}{d\tau} = g(\tau)E'_+(\tau) - h(\tau)E'_-(\tau) - \mu_o h(\tau)E_s(\tau) \tag{51}$$

$$-\frac{dE'_-(\tau)}{d\tau} = g(\tau)E'_-(\tau) - h(\tau)E'_+(\tau) + [\mu_o g(\tau) - 1]E_s(\tau) \tag{52}$$

for the anisotropic field. The functions $g(\tau)$ and $h(\tau)$ are

$$g(\tau) = [1 - \omega_o(\tau)\eta(\tau)]/\mu_o \tag{53}$$

$$h(\tau) = \omega_o(\tau)[1 - \eta(\tau)]/\mu_o \tag{54}$$

where $\eta(\tau)$ is an anisotropy parameter. Similarly, the isotropic field E'' can be represented by

$$-\frac{dE''_+(\tau)}{d\tau} = 2\mu_o[g(\tau)E''_+(\tau) - h(\tau)E''_-(\tau)] \tag{55}$$

$$\frac{dE''_-(\tau)}{d\tau} = 2\mu_o[h(\tau)E''_+(\tau) - g(\tau)E''_-(\tau)] \tag{56}$$

Solving these two sets of coupled differential equations with the appropriate boundary conditions allows us to define the first "iterative" solution. Knowing the irradiances, we can form the function

$$L(\tau, \mu, \phi) = \frac{1}{\mu_0}\left[E'_+(\tau)\delta(\mu - \mu_0)\delta(\pi - \phi_0 - \phi) + E'_-(\tau)\delta(\mu + \mu_0)\delta(\phi - \phi_0)\right]$$

$$+ \frac{E''_+(\tau) + E''_-(\tau)}{2\pi} \tag{57}$$

and insert it into the transfer equation. Representing both the single-scattering albedo $\omega_0(\tau)$ and the scattering phase function, respectively, by the following step functions:

$$\omega_0(\tau) = \sum_{i=1}^{n} \omega_i \chi_{(\tau_i, \tau_{i-1})}(\tau) \tag{58}$$

$$p(\tau, \mu, \phi, \mu', \phi') = \sum_{i=1}^{n} p_i(\mu, \phi, \mu', \phi')\chi_{(\tau_i, \tau_{i-1})}(\tau) \tag{59}$$

we then can easily solve the radiative-transfer equation for each layer.

5.2 CALCULATIONS

We now present some results of our experience in using the inhomogeneous radiative-transfer equation to find aerosol absorption. Figure 19 shows the spectral dependence of path radiance and total radiance for two extreme values of refractive indices. Path radiance for the contaminated atmosphere is about one-half that for the uncontaminated atmosphere, although spectral dependence is nearly the same. Likewise, the total radiance exhibits the same behavior.

In Fig. 20 we see the spectral dependence of path radiance and total radiance for the same conditions as those in Fig. 19, except that the visual range is 2 km instead of 23 km. In this case, the effect of aerosol absorption is quite pronounced in that the "clean" atmosphere has radiance values many times greater than those for the contaminated atmosphere.

Figure 21 illustrates the dependence of path radiance on the single-scattering albedo ω_0. Strictly speaking, the curves should coincide at $\omega_0 = 1$, which implies pure scattering. Because of a limiting procedure in the program, however, we used $\omega_0 = 0.999$. The difference can be accounted for in the different phase functions at m = 1.5 and m = 1.5 - 1.0i. Nevertheless, the main effect, the strong dependence of path radiance on ω_0, is quite evident.

The dependence of both path radiance and total radiance on altitude is exhibited in Fig. 22 for the two refractive indices For all altitudes both the path radiance and the total radiance are greater for the "clean" atmosphere than for the dirty one.

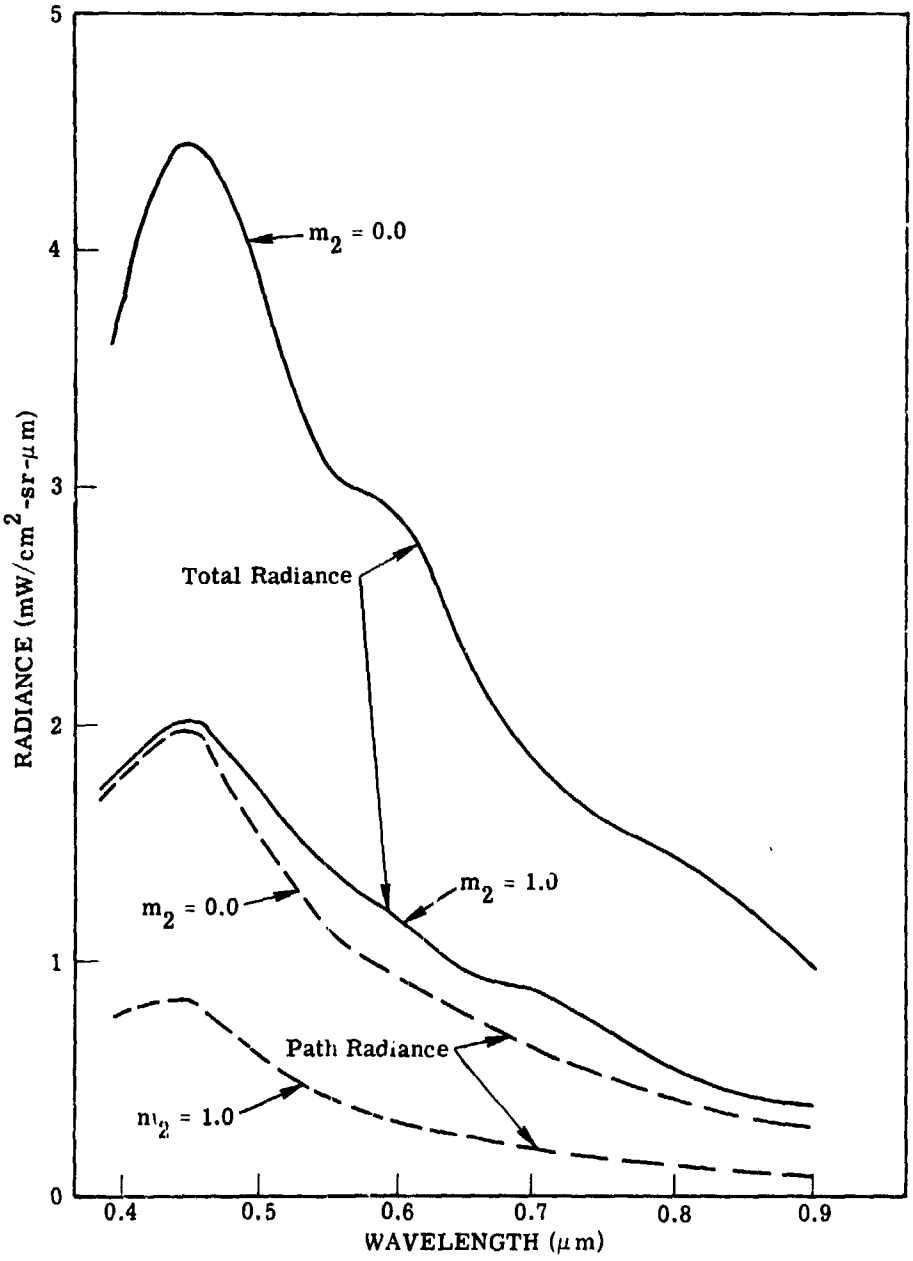

FIGURE 19. DEPENDENCE OF PATH RADIANCE AND TOTAL RADIANCE ON WAVELENGTH FOR HAZE L—VISUAL RANGE = 23 km. Altitude = 1 km, solar zenith angle = 30°, nadir angle = 0°, target reflectance = 0.1, background albedo = 0.1, complex refractive index m = 1.5 - im_2.

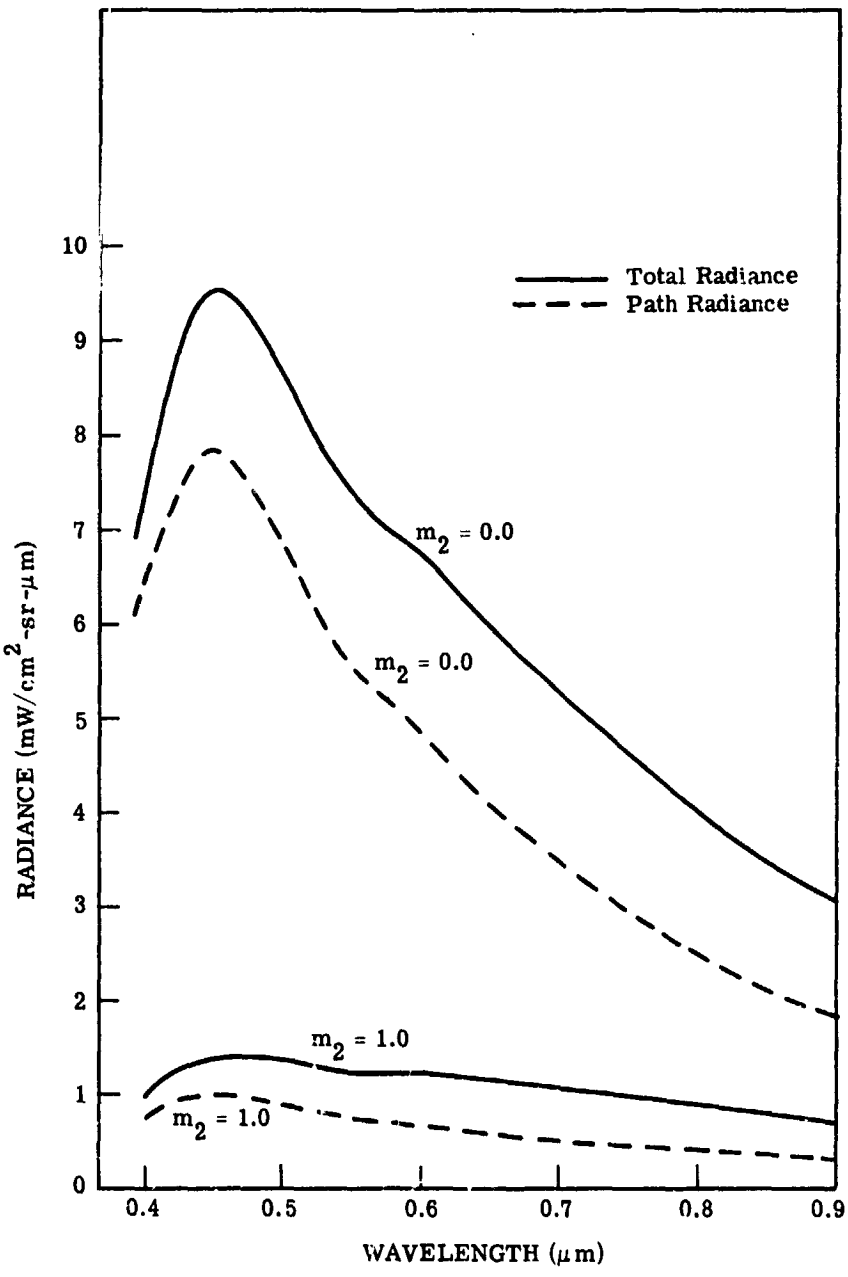

FIGURE 20. DEPENDENCE OF PATH RADIANCE AND TOTAL RADIANCE ON WAVELENGTH FOR HAZE L—VISUAL RANGE = 2 km. Altitude = 1 km, solar zenith angle = 30°, nadir angle = 0°, target reflectance = 0.1, background albedo = 0.1, complex refractive index $m = 1.5 - im_2$.

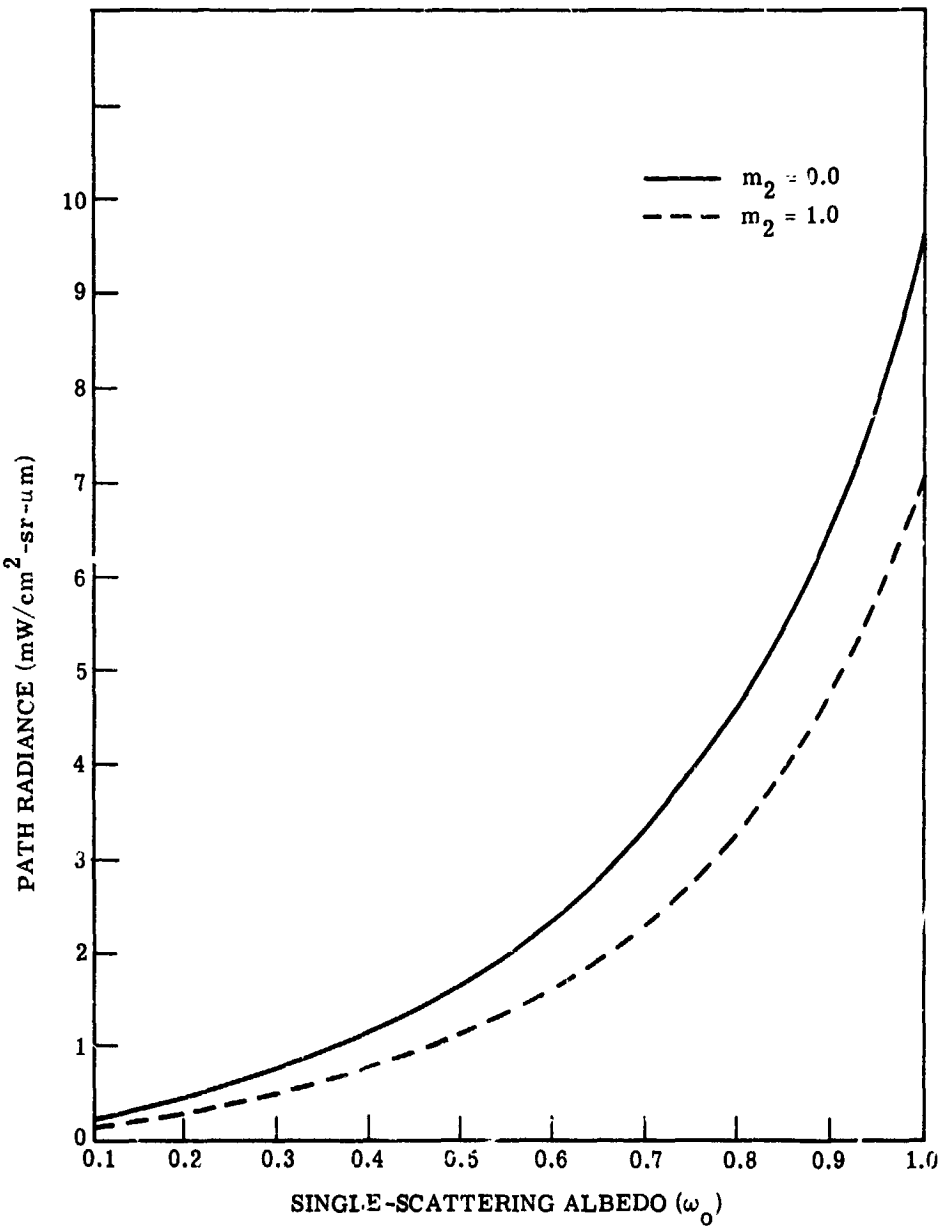

FIGURE 21. DEPENDENCE OF PATH RADIANCE ON SINGLE-SCATTERING ALBEDO FOR HAZE L. Wavelength = 0.4μm, solar zenith angle = 30°, nadir angle = 0°, visual range = 2 km, target reflectance = 0.1, background albedo = 0.1, complex refractive index m = 1.5 - im_2.

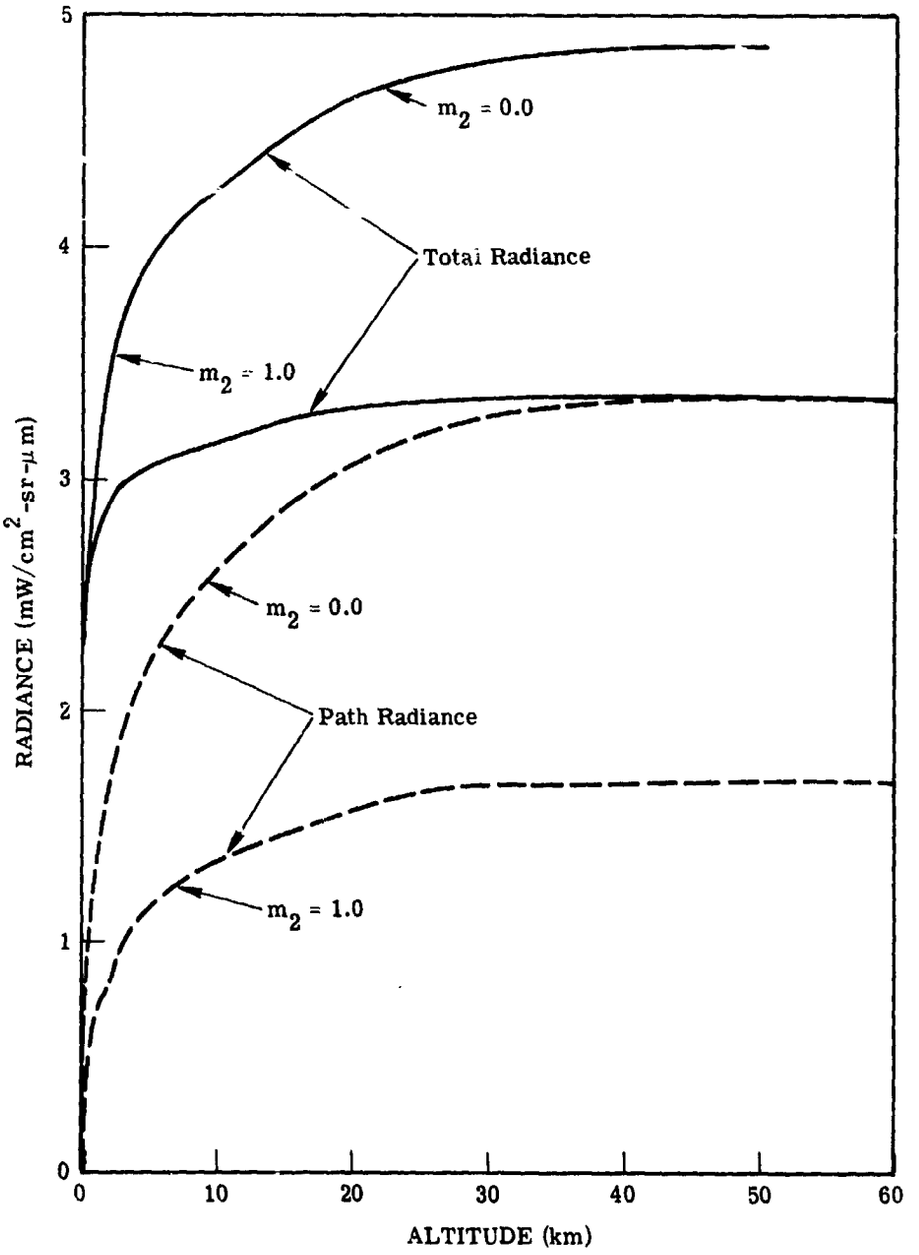

FIGURE 22. DEPENDENCE OF PATH RADIANCE AND TOTAL RADIANCE ON ALTITUDE FOR HAZE L—VISUAL RANGE = 23 km. Wavelength = 0.55μm, solar zenith angle = 30°, nadir angle = 0°, target reflectance = 0.1, background albedo = 0.1, complex refractive index m = 1.5 - im_2.

The same situation is considered in Fig. 23, except that the visual range is 2 km instead of 23 km. In this case, we note a large difference between the path radiances and total radiances for the two refractives indices. Also, one should notice the rapid change in radiance with altitude, an easily understandable effect evident in passage through our heavily contaminated lower troposphere. Figure 24 shows the same conditions as in Fig. 23, except that we consider the variation within the first 5 km.

Figure 25 illustrates the dependence of path radiance on altitude in the lower troposphere for several refractive indices. It is clear that even a small amount of absorption can change the path radiance by a significant amount. The results are quite sensitive to the imaginary part of the refractive index, especially when $0.01 \lesssim m_2 \lesssim 0.10$.

Figure 26 portrays the variations with altitude in path radiance, attenuated radiance, and total radiance for the cases of no absorption and heavy absorption. Recall that

$$L_T = L_A + L_P \tag{60}$$

where L_A, the attenuated radiance, is the product of surface radiance and transmittance. In this case of a heavy haze (that is, for a visual range of 2 km), path radiance increases rapidly with altitude for a "clean" atmosphere, and attenuated radiance decreases rapidly. The combination produces a total radiance which at first decreases, then reaches a minimum, and finally increases to its asymptotic limit. In the case of heavy absorption, all radiances are lower.

Finally, Fig. 27 illustrates the behavior of path radiance as a function of the nadir view-angle for different refractive indices. The peak occurs at an antisolar angle of 30°. Again, contaminated air produces small values of radiance.

These results clearly show the large differences between radiances for "clean" and "dirty" atmospheric conditions. The index of 1.5 represents a silicate haze, not uncommon in various parts of the world. The index of 1.5 - 1.0i is quite similar to that for soot particles found in the contaminated air of urban areas. Typical refractive indices for various aerosols are presented in the work of Kondratyev et al., [33] for the 0.40- to 15.0-μm wavelength region; they confirm our original assumption of a very weak spectral variation in the refractive index, at least for the visible and near-infrared regions.

In conclusion, we now have the ability to model any kind of contaminated atmosphere characterized by aerosol and ozone absorption. The radiation field can vary considerably, depending upon the degree of contamination as represented by refractive index and particle size.

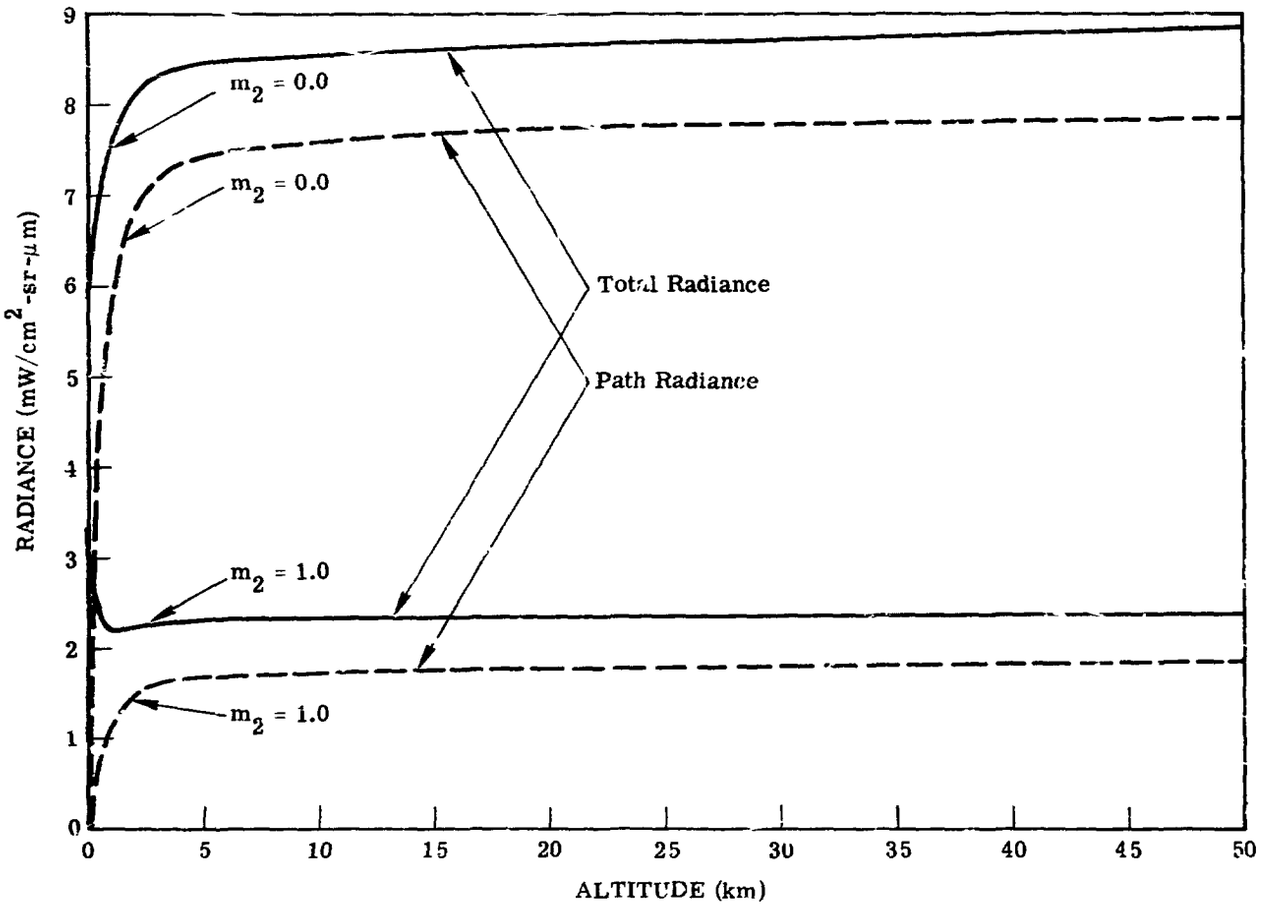

FIGURE 23. DEPENDENCE OF PATH RADIANCE AND TOTAL RADIANCE ON ALTITUDE FOR HAZE L—VISUAL RANGE = 2 km. Wavelength = 0.55μm, solar zenith angle = 30^o, nadir angle = 0^o, target reflectance = 0.1, background albedo = 0.1, complex refractive index m = 1.5 - im_2.

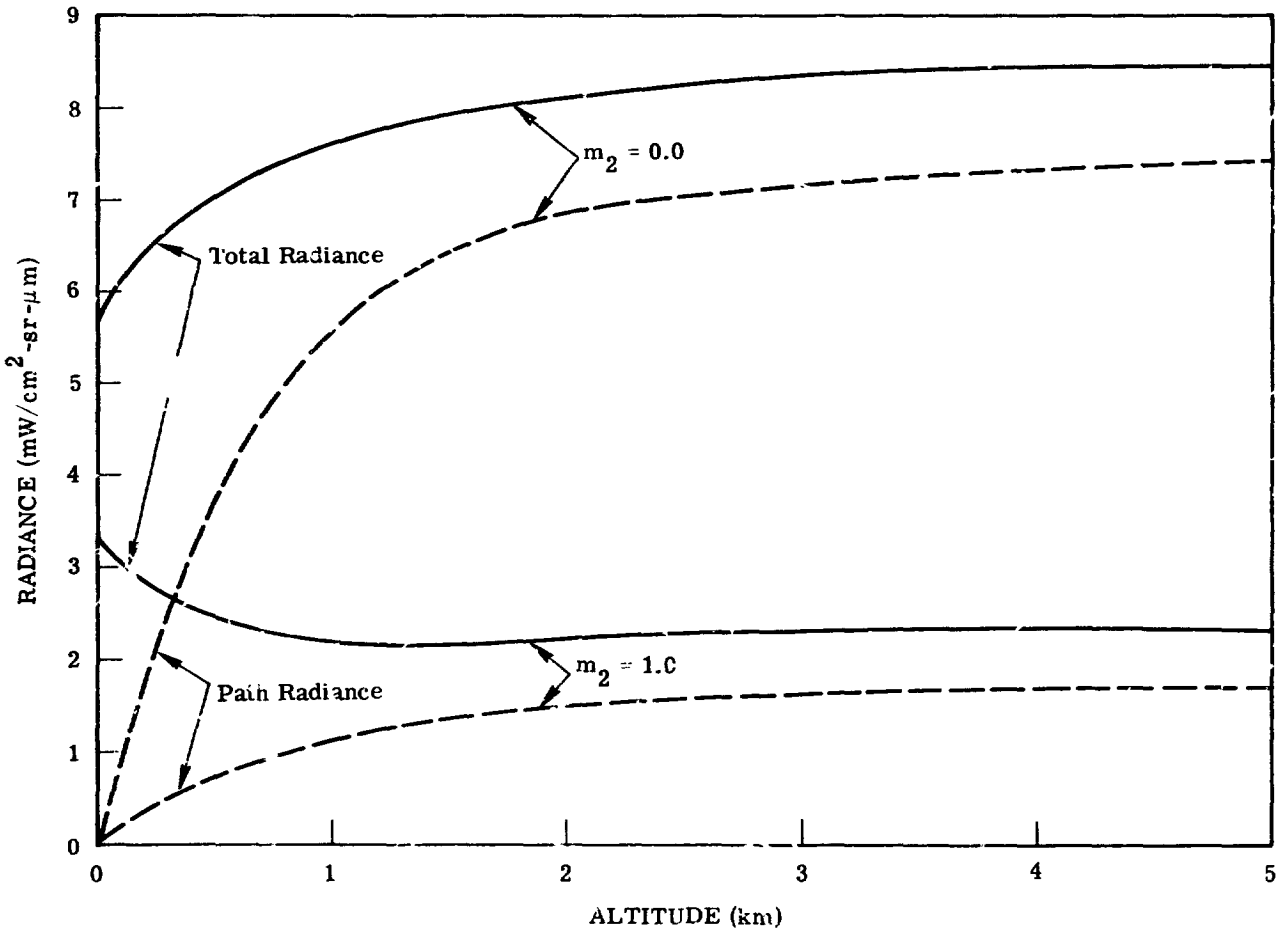

FIGURE 24. DEPENDENCE OF PATH RADIANCE AND TOTAL RADIANCE ON ALTITUDE IN THE LOWER TROPOSPHERE FOR HAZE L. Wavelength = 0.55μm, solar zenith angle = 30°, nadir angle = 0°, visual range = 2 km, target reflectance = 0.1, background albedo = 0.1, complex refractive index m = 1.5 - im_2.

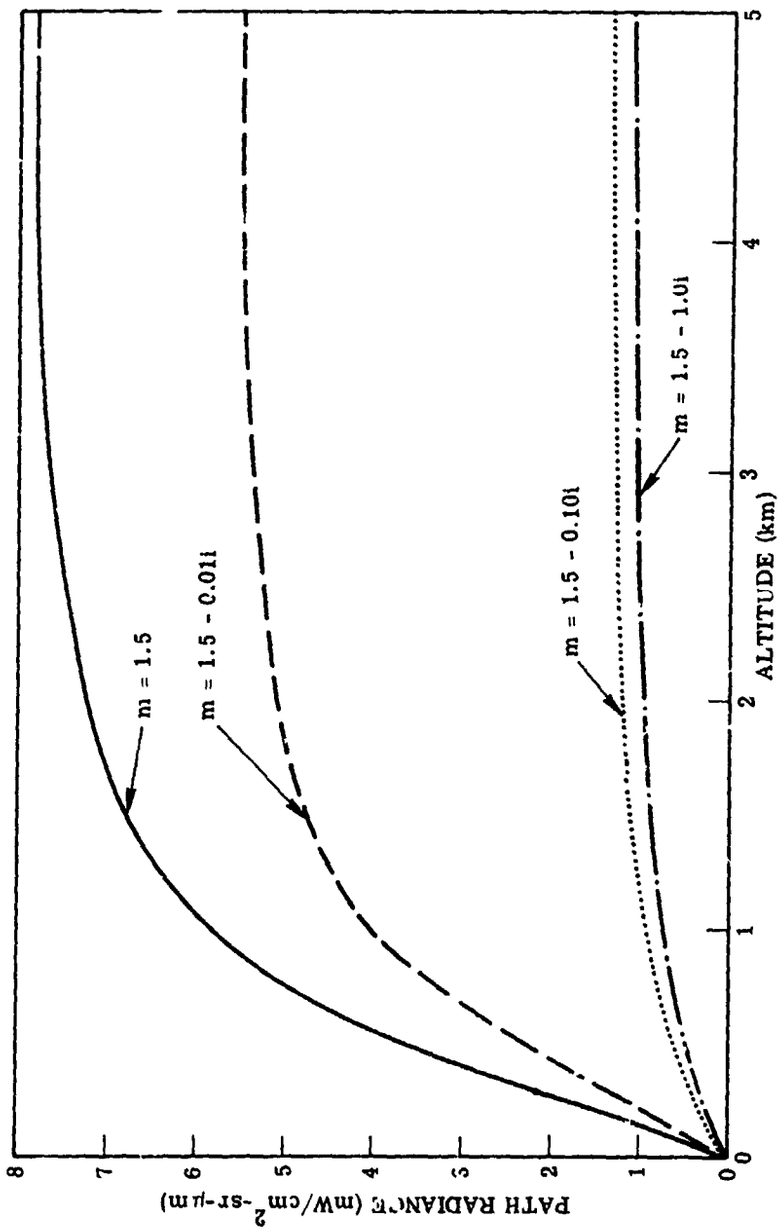

FIGURE 25. DEPENDENCE OF PATH RADIANCE ON ALTITUDE IN THE LOWER TROPOSPHERE FOR SEVERAL REFRACTIVE INDICES. Wavelength = 0.55μm, solar zenith angle = 30°, nadir view angle = 0°, target reflectance = 0.1, background reflectance = 0.1, visual range = 2 km.

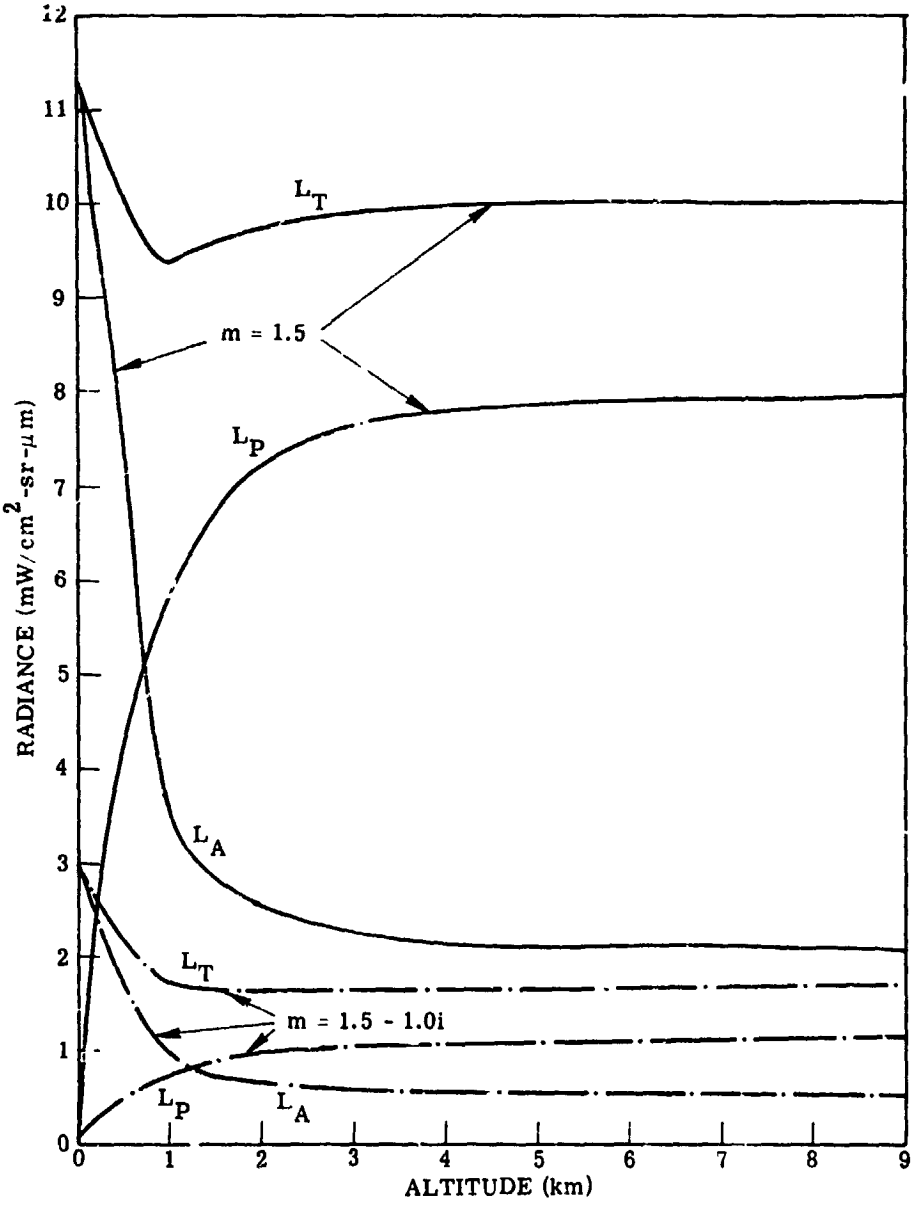

FIGURE 26. DEPENDENCE OF PATH RADIANCE, ATTENUATED RADIANCE AND TOTAL RADIANCE ON ALTITUDE FOR NO ABSORPTION AND HEAVY ABSORPTION. Wavelength = 0.55μm, solar zenith angle = 30^o, nadir view angle = 0^o, target reflectance = 0.1, background reflectance = 0.1, visual range = 2 km.

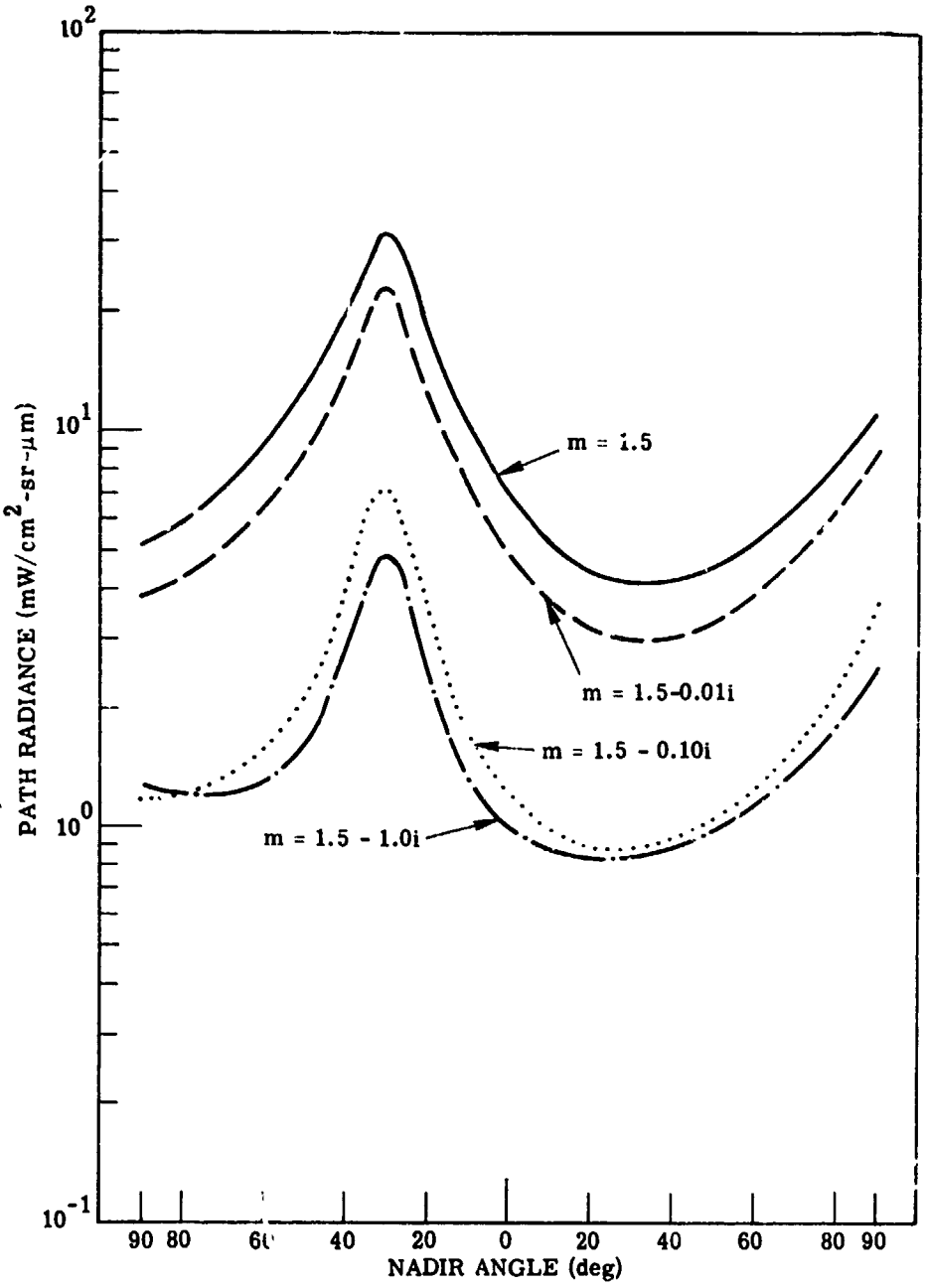

FIGURE 27. DEPENDENCE OF PATH RADIANCE ON NADIR VIEW ANGLE IN THE SOLAR PLANE FOR SEVERAL REFRACTIVE INDICES. Wavelength = 0.55μm, altitude = 2 km, solar zenith angle = 30°, target reflectance = 0.1, background reflectance = 0.1, visual range = 2 km.

For remote sensing applications, in situ measurements of the air would aid in the definition of aerosol content and, hence, would allow us to calculate the basic radiometric quantities, transmittance, irradiance, and radiance. If such measurements are not feasible, then we could look at multispectral scanner data corresponding to the anti-solar direction in order to obtain some knowledge of the phase function. This would help in the estimation of aerosol composition. Also, laser scanning or lidar techniques could be employed to determine the same quantity.

6
MULTIDIMENSIONAL RADIATIVE TRANSFER

In considering the transfer of radiation, we can assume a plane-parallel atmosphere if we exclude satellite remote sensing at very high altitudes. Almost all analysis in radiative-transfer theory has dealt with a one-dimensional plane-parallel atmosphere, that is, one in which the optical parameters, ω_0 and τ, and phase function, $p(\cos \chi)$, vary only in the direction perpendicular to the surface. It has been further assumed that the lower surface is a perfectly diffuse one which is homogeneous in a horizontal plane. These simplifications are sometimes necessary in order to solve the radiative-transfer equation. Although assuming that ω_0, τ, and phase functions vary only in the vertical direction, we will consider the surface to be a non-homogeneous Lambertian type. This set of assumptions will enable us to calculate the influence of background reflectances on the target radiance.

6.1 GENERAL THEORY

The general, three-dimensional, time-independent, radiative-transfer equation for an atmosphere which is plane-parallel, scattering and absorbing, but non-emitting is as follows:

$$\hat{\Omega} \cdot \nabla \bar{L}(\vec{R}, \hat{\Omega}) = -\kappa(\vec{R})\bar{L}(\vec{R}, \hat{\Omega}) + \frac{\beta(\vec{R})}{4\pi} \int_{\Omega'} p(\hat{\Omega} \cdot \hat{\Omega})\bar{L}(\vec{R}, \hat{\Omega}')\, d\hat{\Omega}' \tag{61}$$

where Ω' is the unit vector in the direction of the scattered photon at position $\vec{R}$, and $\bar{L}(\vec{R}, \hat{\Omega})$ is the total spectral radiance, that is, the sum of the direct solar component and the diffuse component.

The first term on the right-hand side represents a loss of energy along a path, whereas the second term represents the sum of all energy scattered into the direction $\hat{\Omega}$. For a one-dimensional atmosphere, this can be written as

$$\mu \frac{dL}{d\tau} = L(\tau, \mu, \phi) - \frac{\omega_0(\tau)}{4\pi} \int_0^{2\pi} \int_{-1}^{1} p(\tau, \mu, \phi, \mu', \phi')L(\tau, \mu', \phi')\, d\mu'\, d\phi'$$

$$- \frac{\omega_0(\tau)}{4\pi} E_0 e^{-\tau/\mu_0} p(\mu, \phi, -\mu_0, \phi_0) \tag{62}$$

where μ, ϕ define the angular coordinates of the scattered radiation

$p(\tau, \mu, \phi, \mu', \phi')$ is the single-scattering phase function

E_0 is the extra-terrestrial solar irradiance of the top of the atmosphere

μ_0, ϕ_0 define the angular coordinates of the sun

One can immediately find a formal solution to the integro-differential equation above by using an integrating factor; the solution is

$$L_D(\tau, \mu, \phi) = L_D(\tau_o, \mu, \phi)e^{-(\tau_o-\tau)/\mu}$$

$$+ \frac{\omega_o}{4\pi\mu}\int_0^{2\pi}\int_{-1}^{1} p(\mu, \phi, \mu', \phi')\int_{\tau}^{\tau_o} e^{-(\tau'-\tau)/\mu} L_D(\tau', \mu', \phi')\,d\tau'\,d\mu'\,d\phi'$$

$$+ \frac{\omega_o\mu_o E_o p(\mu, \phi, -\mu_o, \phi_o)}{4\pi(\mu + \mu_o)}\left[e^{-\tau/\mu_o} - e^{-\tau_o/\mu_o}e^{-(\tau_o-\tau)/\mu}\right] \tag{63}$$

for the upwelling radiance. The downwelling radiance is given by

$$L_D(\tau, -\mu, \phi) = L_D(0, -\mu, \phi)e^{-\tau/\mu}$$

$$+ \frac{\omega_o}{4\pi\mu}\int_0^{2\pi}\int_{-1}^{1} p(-\mu, \phi, \mu', \phi')\int_{0}^{\tau} e^{-(\tau-\tau')/\mu} L_D(\tau', \mu', \phi')\,d\tau'\,d\mu'\,d\phi'$$

$$+ \frac{\omega_o\mu_o E_o p(-\mu, \phi, -\mu_o, \phi_o)}{4\pi(\mu - \mu_o)}\left(e^{-\tau/\mu} - e^{-\tau/\mu_o}\right);\ \mu \neq \mu_o \tag{64}$$

There are two general boundary conditions:

$$L(0, -\mu, \phi) = 0$$

$$L(\tau_o, \mu, \phi) = \int_0^{2\pi}\int_0^{1} \mu'\rho'(\mu, \phi, -\mu', \phi')[L(\tau_o, -\mu', \phi') + L_s(\tau_o, -\mu', \phi')]\,d\mu'd\phi \tag{65}$$

where $\rho'(\mu, \phi, \mu', \phi')$ is the bidirectional reflectance of the surface. Thus, Eq. (62), together with the boundary conditions, can be used to calculate the complete radiation field in a plane-parallel atmosphere having horizontal homogeneity.

6.2 THE UNIFORM DISK PROBLEM

We can study the effects of background on target by considering a uniform disk with a perfectly diffuse reflectance which is surrounded by a Lambertian background surface with a different reflectance. First, we shall consider an isotropic scattering law and calculate the singly-scattered surface radiance, the singly-scattered solar radiance, the doubly-scattered solar radiance, and the attenuated radiance. Secondly, we shall calculate the same quantities for an anisotropic scattering law.

6.2.1 ISOTROPIC SCATTERING

Using the one-dimensional solution of Eqs. (63) and (64), we can impose a coordinate system and obtain a solution for the case of a uniform disk surrounded by a spatially infinite, uniform background surface. The appropriate geometry is illustrated in Fig. 28. Let us assume that an observer is located at altitude h corresponding to optical depth τ and is viewing the origin of the coordinate system, i.e., the center of the disk. Radiation emanates from point S on the surface, is attenuated as it propagates to point Q, is scattered into direction QP, and finally is attenuated to the point of observation at P. Mathematically, we iterate the integral equation once for single scattering. Assuming isotropic scattering that corresponds to a very light haze condition, we have for the result

$$L(\tau, 1) = L(\tau_o, 1)e^{-(\tau_o-\tau)} + \frac{\omega_o\mu_o E_o}{4\pi(1+\mu_o)}\left[e^{-\tau/\mu_o} - e^{-\tau_o/\mu_o}e^{-(\tau_o-\tau)}\right]$$

$$+ \frac{\omega_o}{2\pi}\left[\rho_e\tilde{E}_-(\rho_e) - \rho_i\tilde{E}_-(\rho_i)\right]\left[\int_\tau^{\tau_o}\left\{\mu_c e^{-(\tau_o-\tau')/\mu_c} - (\tau_o-\tau')E_1\left[(\tau_o-\tau')/\mu_c\right]\right\}d\tau'\right]$$

$$+ \frac{\omega_o}{4\pi}\rho_e\tilde{E}_-(\rho_e)\left[1 + (\tau_o-\tau-1)e^{-(\tau_o-\tau)} - (\tau_o-\tau)E_1(\tau_o-\tau)\right]$$

$$+ \frac{\omega_o^2\mu_o E_o}{8\pi}\left\{e^{-\tau_o/\mu_o}\left[\mu_o \ell n\frac{1-\mu_o}{\mu_o} + e^{-(\tau_o-\tau)} - 1 - (\tau_o-\tau+\mu_o)E_1(\tau_o-\tau) - \mu_o Ei\left(\frac{1-\mu_o}{\mu_o}\tau_o\right)\right]\right.$$

$$+ e^{-\tau/\mu_o}\left[\mu_o \ell n\left(\frac{1+\mu_o}{1-\mu_o}\right) + \mu_o E_1\left[(\tau_o-\tau)\left(\frac{1+\mu_o}{\mu_o}\right)\right] + \mu_o Ei\left(\frac{1-\mu_o}{\mu_o}\tau\right)\right]$$

$$\left. + e^{-\tau} - e^{-\tau_o} + (\tau_o-\mu_o)E_1(\tau_o) - (\tau-\mu_o)E_1(\tau)\right\} \qquad (66)$$

where $\mu_c = \dfrac{z}{\sqrt{R^2+z^2}}$

E_1 and Ei are exponential integrals

The first term represents the radiation from the center of the disk attenuated to point P. The second represents the singly-scattered solar radiation. The next two terms represent the surface radiation being singly scattered and attenuated to point P. And the last term is the doubly-scattered solar radiation.

A more advanced case has also been developed for both a finite solid angle of view and small scan angles. The correction term to be added to Eq. (66) is too involved to present here, but results of the analysis will be. The geometry is illustrated in Fig. 29. The view angle of the sensor is Ω steradians, altitude is h (in km), visual range is V, interior Lambertian disk reflectance is ρ_i, and exterior Lambertian background reflectance is ρ_e. In our analysis the solid angle Ω of the sensor is assumed to be 2.5 mrad: the reflectances used are illustrated in Fig. 30. In Fig. 31 we see the singly-scattered surface radiance for black, blue, red, and white disks on a green vegetation background. Radiance with the black disk is essentially that for green vegetation (as expected); radiance with the blue disk is slightly higher for $0.4 \leq \lambda \leq 0.65$ μm because of the higher reflectance of the disk. For a red panel with a peak in the reflectance curve near 0.65μm, the radiance is slightly higher than for a black disk at longer wavelengths. For short wavelengths (i.e., $0.4 \leq \lambda \leq 0.55$ μm) it is essentially zero. Finally, for a white disk the radiance is much higher than for a black or colored disk, but it generally follows the spectral shape for green vegetation.

We can now examine the effect of ever-increasing disk size on singly-scattered surface radiance. Figure 32 illustrates this effect for a black disk on green vegetation for disk radii of 10m, 500m, 1000m, and 5000m. For the smallest disk the radiance is similar to that for green vegetation, whereas for a disk of 100 times that radius, the radiance decreases by a factor of 8. This illustrates the strong dependence of surface radiance on disk size. Visual range is 2 km.

Figure 33 is the same situation, except that we now have a white disk on a green vegetation background. It should be noted that the effect is just the opposite from that of the black disk. As disk size increases, the radiance increases because it is dominated by the high reflectance of the white disk relative to the lower reflectance of the background. Also, for small disks the curves are similar to those for green vegetation, while for large disks the curves approach the spectrally flat white reflectance, biased (of course) by the intrinsic spectral properties of the atmosphere.

These effects are illustrated in a more meaningful way in Fig. 34. Here the singly-scattered surface radiance is presented as a function of disk radius for several wavelengths by the lower reflectance of the disk. At the peak of red reflectance ($\lambda = 0.7$ μm), however, radiance increases because the disk reflectance is higher than that for green vegetation at that wavelength. After a radius of about 5 km, the interference effect hardly changes.

We can now consider the relative magnitudes of various components of the total spectral radiance received by a sensor. Figure 35 illustrates the relative magnitude for a black disk on a green vegetation background. L_{sur} is the singly-scattered surface radiance, L_{ss} is the singly-scattered sky radiance, L_{ds} is the doubly-scattered sky-radiance, and L_{tot} is the sum

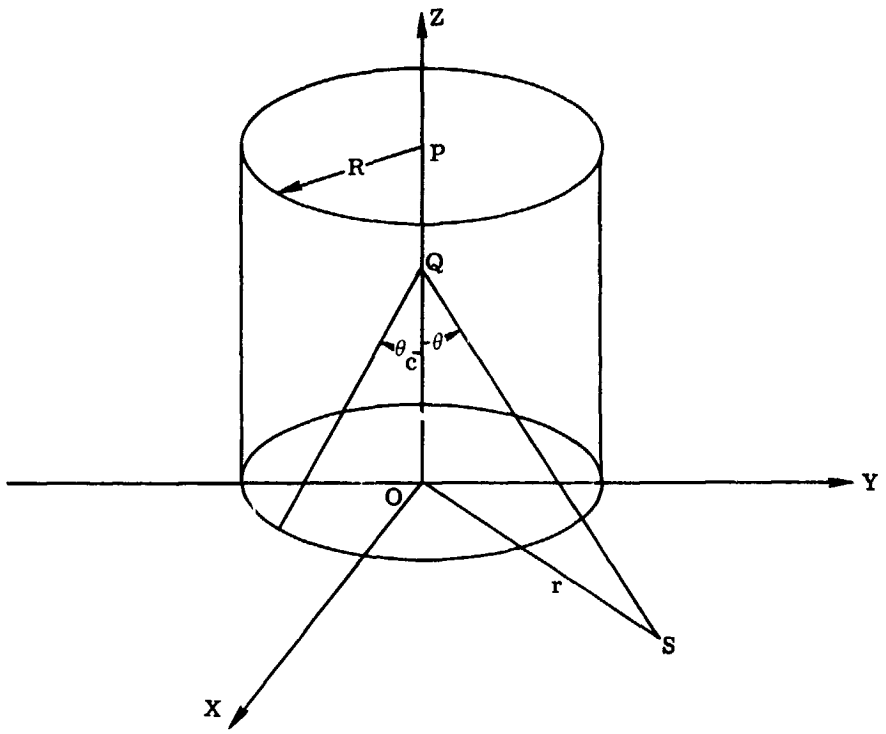

FIGURE 28. GEOMETRY FOR ISOTROPIC SCATTERING WITH A UNIFORM SURFACE

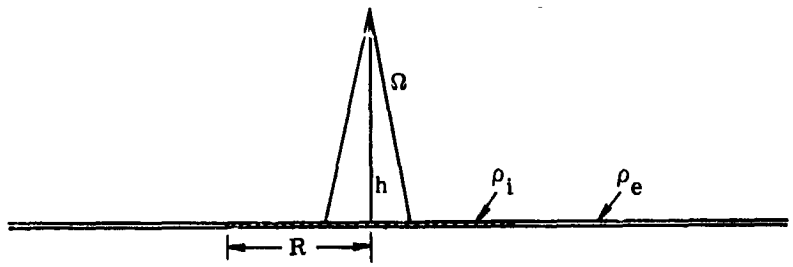

FIGURE 29. DISK GEOMETRY FROM EQUATION (66)

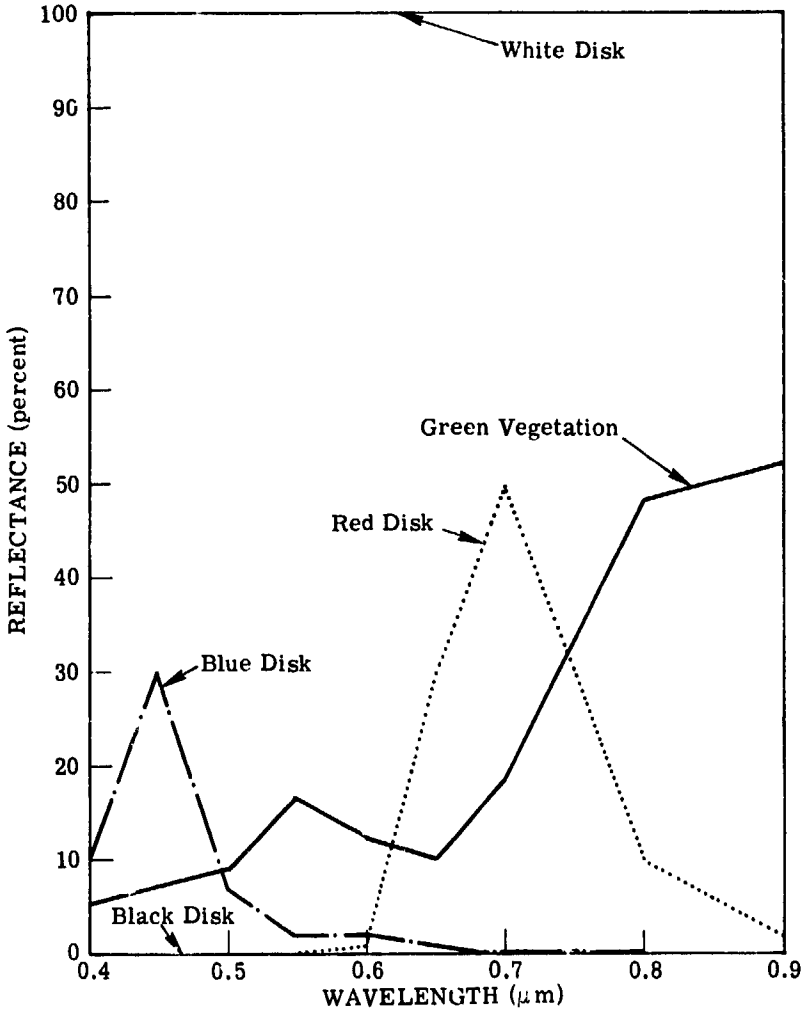

FIGURE 30. TARGET REFLECTANCES

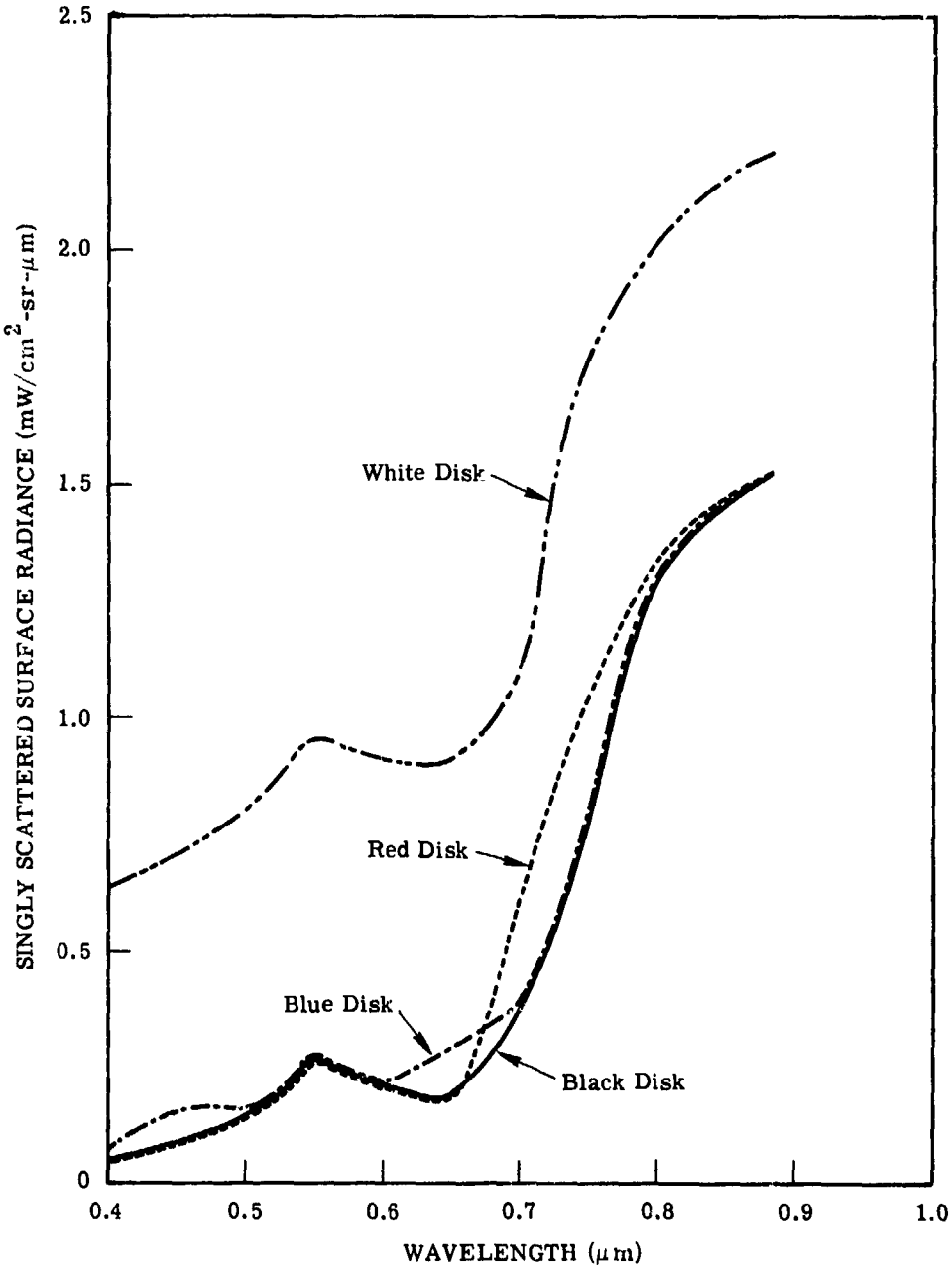

FIGURE 31. SINGLY SCATTERED SURFACE RADIANCES OF COLORED DISKS ON GREEN VEGETATION BACKGROUND. Disk radius = 10m, visual range = 2 km, altitude = 1 km.

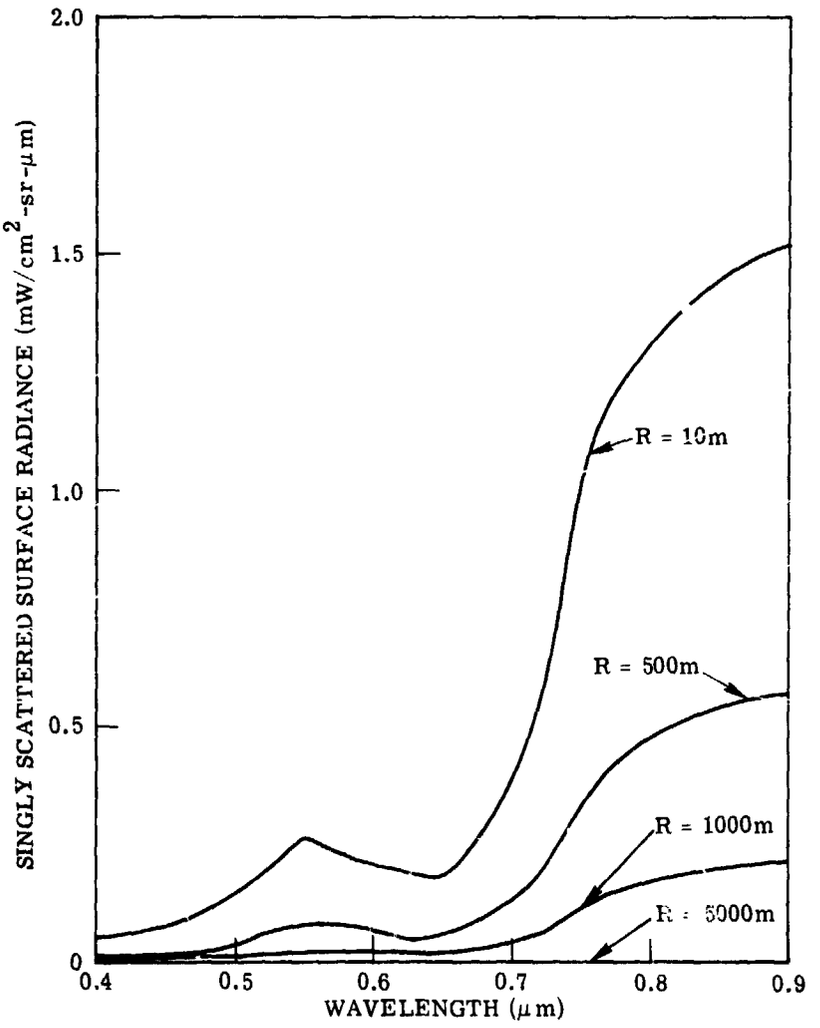

FIGURE 32. SINGLY SCATTERED SURFACE RADIANCE FOR BLACK DISK WITH GREEN VEGETATION BACKGROUND. Visual range = 2 km, altitude = 1 km.

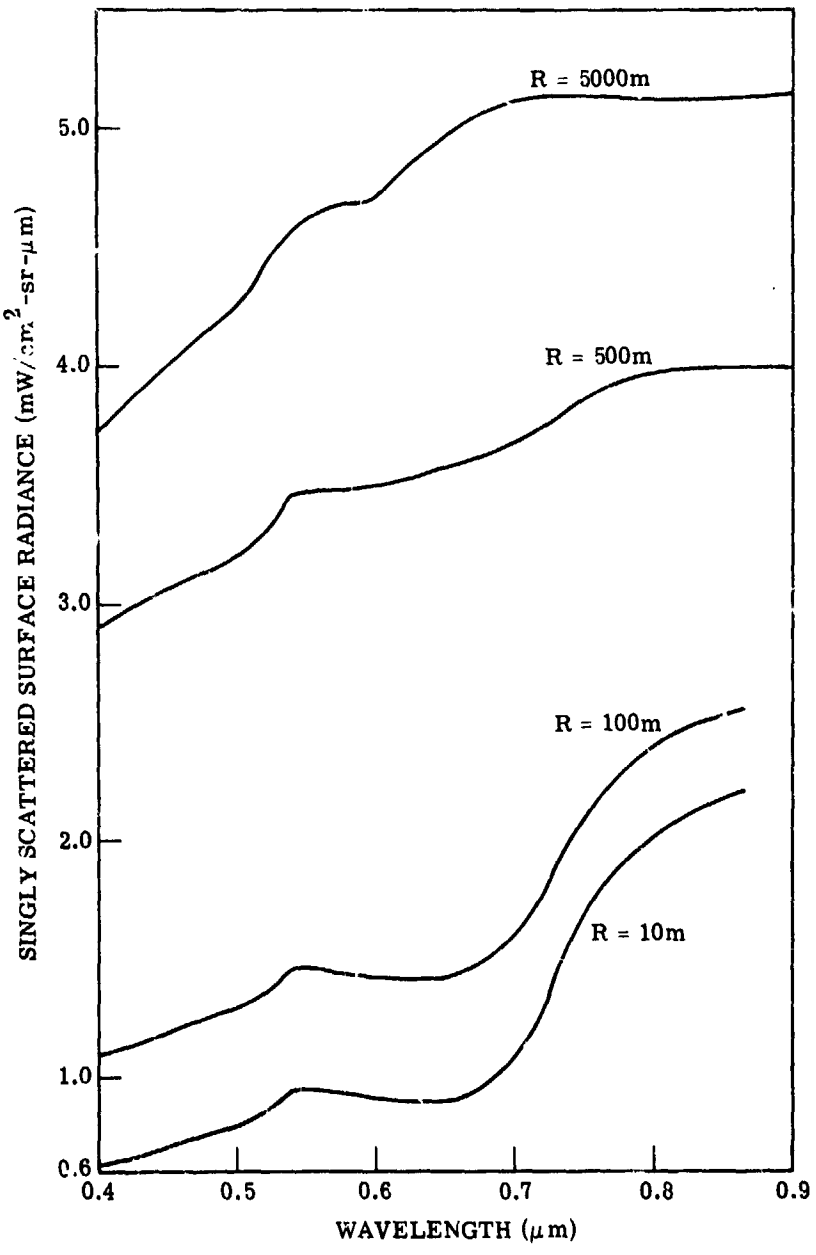

FIGURE 33. SINGLY SCATTERED SURFACE RADIANCE FOR WHITE DISK WITH GREEN VEGETATION BACKGROUND. Visual range = 2 km, altitude = 1 km.

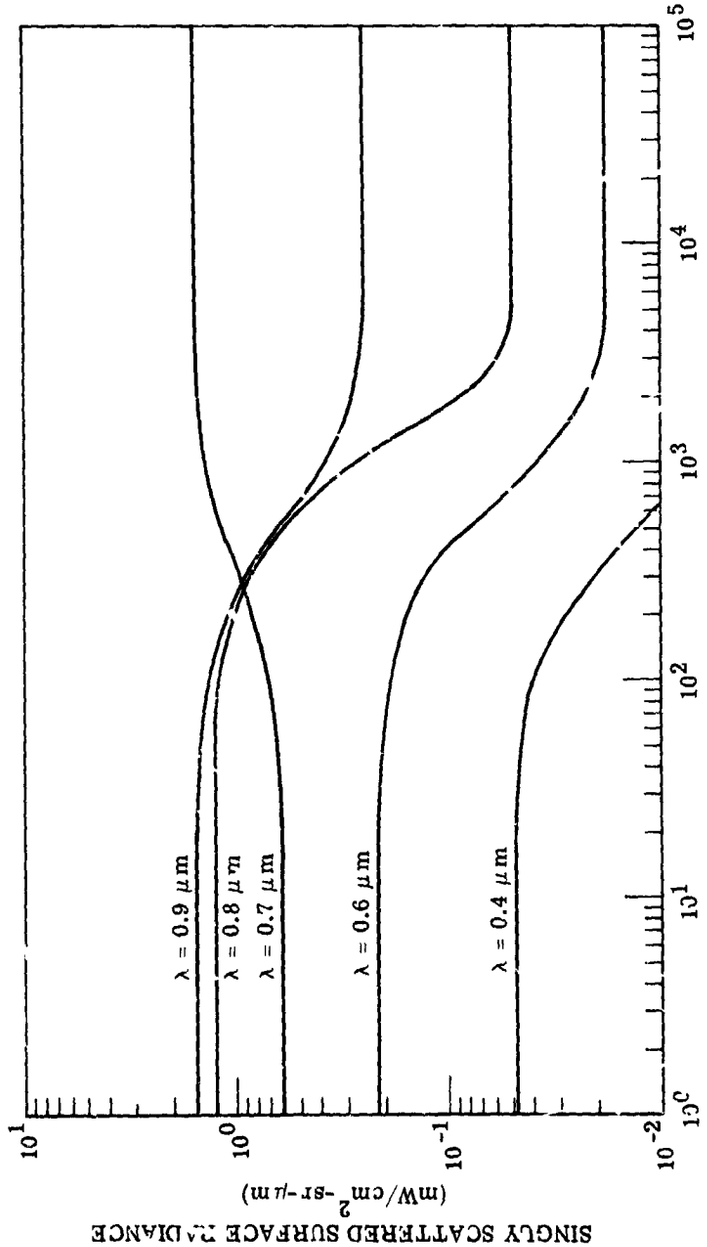

FIGURE 34. SINGLY SCATTERED SURFACE RADIANCE FOR RED DISK WITH GREEN VEGETATION BACKGROUND. Visual range = 2 km, altitude = 1 km.

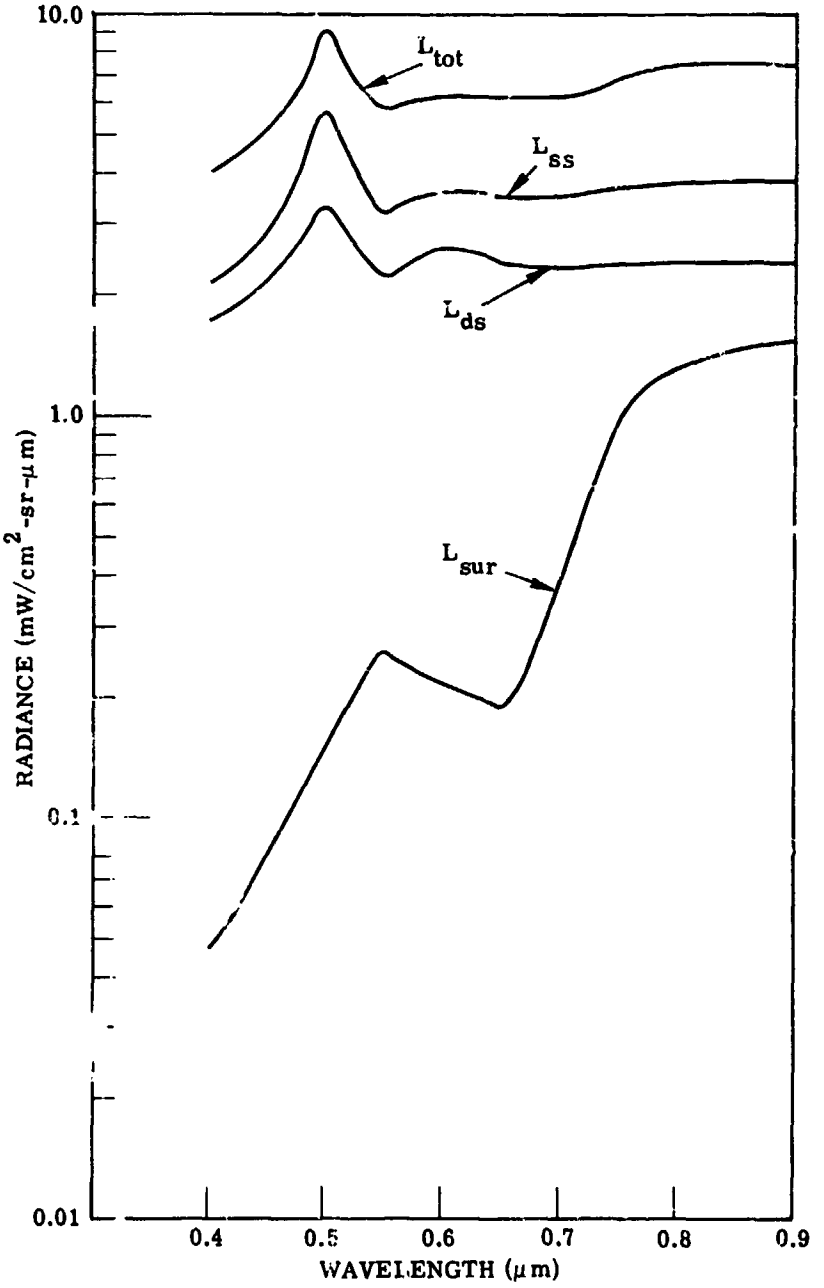

FIGURE 35. RADIANCE VALUES FOR BLACK DISK WITH GREEN VEGETATION BACKGROUND. Disk radius = 10m, visual range = 2 km, altitude = 1 km.

of these components. L_{att}, the directly attenuated component, is zero in this case because the resolution element lies entirely within the black disk. The peak at 0.5μm results primarily from the peak in extraterrestrial irradiance at the top of the atmosphere. Dominating everything is the singly-scattered sky radiance.

Now we can examine the case of a white disk on a green vegetation background (see Fig. 36). Here L_{att} is not negligible; in fact, it is the dominant term. The singly-scattered surface radiance is also not negligible, compared to sky radiance (at least for long wavelengths).

In all of the analysis so far, only isotropic scattering has been considered—which probably tends to overemphasize the surface contribution. In a more advanced treatment we consider anistropic scattering, as well as various geometries.

6.2.2 ANISOTROPIC SCATTERING

We can now consider the more realistic, but also more complicated, case of anisotropic scattering. Iterating the formal solution for upwelling radiance produces the following:

$$L(\tau, \mu, \phi) = L(\tau_o, \mu, \phi)e^{-(\tau_o-\tau)/\mu} + \frac{\omega_o \mu_o E_o}{4\pi(\mu+\mu_o)} p(\mu, \phi, -\mu_o, \phi)\left[e^{-\tau/\mu_o} - e^{-\tau_o/\mu_o}e^{-(\tau_o-\tau)/\mu}\right]$$

$$+ \frac{\omega_o}{4\pi\mu}\int_0^{2\pi}\int_{-1}^{1} p(\mu, \phi, \mu', \phi') \int_{\tau}^{\tau_o} e^{(\tau'-\tau)/\mu} L(\tau_o, \mu', \phi')e^{-(\tau_o-\tau)/\mu'} \, d\tau' \, d\mu' \, d\phi'$$

$$+ \frac{\omega_o}{4\pi\mu}\int_0^{2\pi}\int_{-1}^{1} p(\mu, \phi, \mu', \phi') \int_{\tau}^{\tau_o} \frac{\omega_o \mu_o E_o}{4\pi(\mu'+\mu_o)} p(\mu'\phi', -\mu_o, \phi_o) \times$$

$$\left[e^{-\tau'/\mu_o} - e^{-\tau_o/\mu_o}e^{-(\tau_o-\tau')/\mu}\right] d\tau' \, d\mu' \, d\phi' \qquad (67)$$

The first term on the right-hand side represents the directly attenuated surface radiance; the second is the singly scattered solar radiance; the third is the singly-scattered surface radiance; and the last represents the doubly-scattered solar radiance. We can immediately evaluate the first and second terms by using actual phase functions; for the last term we can make use of the isotropic scattering law. For the third term, however, we must consider an approximation for the phase function.

Let us represent the phase function by the following:

$$p(\mu) = \sum_{i=1}^{n-1} C_i e^{-a_i/\mu} + C_n \qquad (68)$$

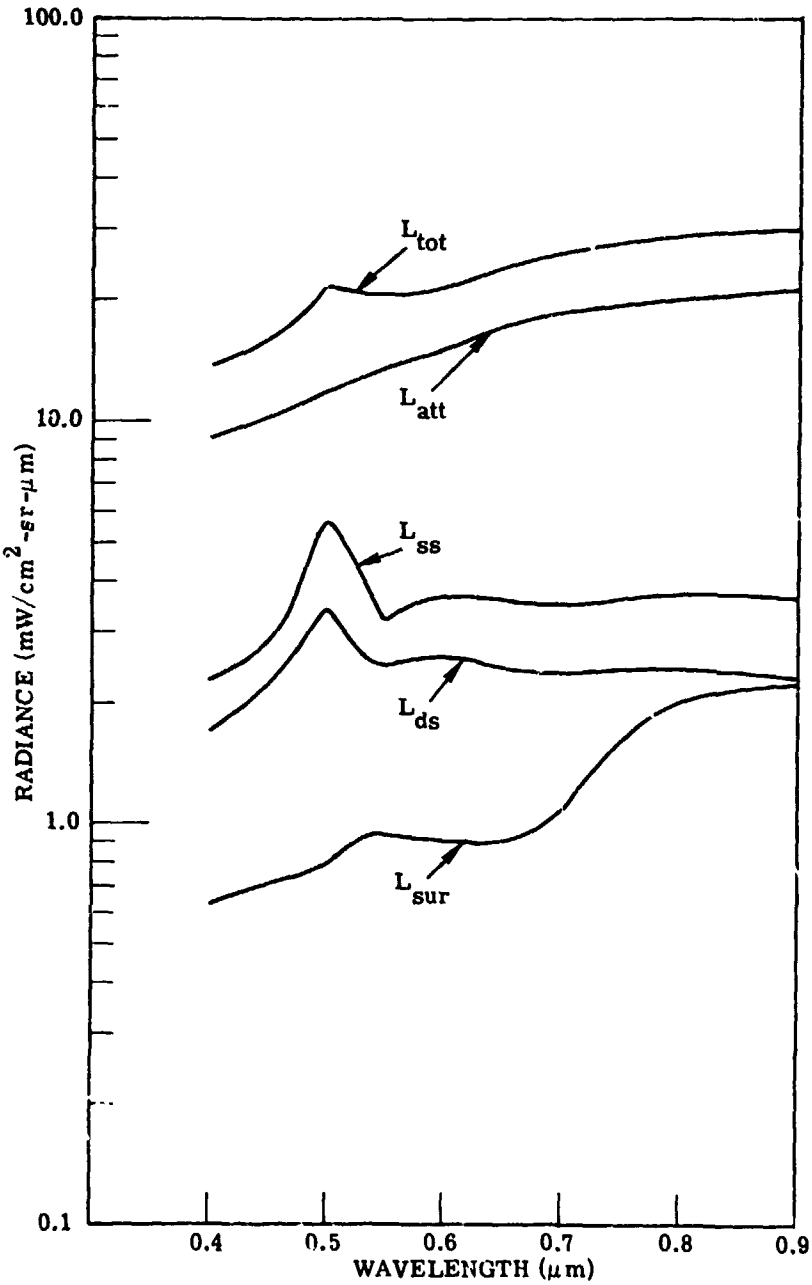

FIGURE 36. RADIANCE VALUES FOR WHITE DISK WITH GREEN VEGETATION BACKGROUND. Disk radius = 10m, visual range = 2 km, altitude = 1 km.

where C_i C_n, and a_i are constants to be determined. We will attempt to fit the phase function in the region 0^o to 90^o with the first part of this function and the last half from 90^o to 180^o with the constant term C_n. This is reasonable since (1) only the first half of the phase function is used in the disk problem, and (2) the last half of the phase function is almost constant anyway. At the origin, or when $\theta = 0^o$

$$p(1) \quad p_o = \sum_{i=1}^{n-1} C_i e^{-a_i} + C_n \tag{69}$$

Since the phase function is azimuthally symmetric, we have the normalization

$$1, 2\int_{-1}^{1} p(\mu)\, d\mu = 1 \tag{70}$$

This becomes

$$1/2 \sum_{i=1}^{n-1} C_i E_2(a_i) + C_n = 1 \tag{71}$$

when $E_2(a_i)$ is the exponential integral, that is,

$$E_2(z) = \int_1^{\infty} \frac{e^{-zt}}{t^2}\, dt \tag{72}$$

The a_i can be determined by using an iteration scheme. The results of this fitting procedure are illustrated in Figs. 37-40 for $\lambda = 0.40$ and $0.90\ \mu m$ and for $m = 1.5$; and $m = 1.5 - 1.0i$.

Taking $\theta = 0^o$, or $\mu = 1$, we have for the singly-scattered surface radiance:

$$L_{sur}(\tau, 1, \mu) = \frac{\omega_o}{2\pi} \tilde{E}_-(\tau_o) \sum_{i=1}^{n} C_i (\rho_E - \rho_I) \left\{ \int_{\tau}^{\tau_o} e^{-(\tau' - \tau)/\mu_c} e^{-(a_i + \tau_o - \tau')/\mu_c} \right.$$

$$\left. - \int_{\tau}^{\tau_o} e^{-(\tau' - \tau)} (a_i + \tau_o - \tau') E_1\left[(a_i + \tau_o - \tau')/\mu_c\right] d\tau' \right\}$$

$$+ \frac{\omega_o}{2\pi} \tilde{E}_-(\tau_o) \sum_{i=1}^{n} C_i \rho_I \left[-(a_i + \tau_o - \tau - 1) E_1(a_i + \tau_o - \tau) \right.$$

$$\left. + (a_i - 1) E_1(a_i) e^{-(\tau_o - \tau)} + e^{-(a_i + \tau_o - \tau)} \ln\left(\frac{a_i + \tau_o - \tau}{a_i}\right) \right] \tag{73}$$

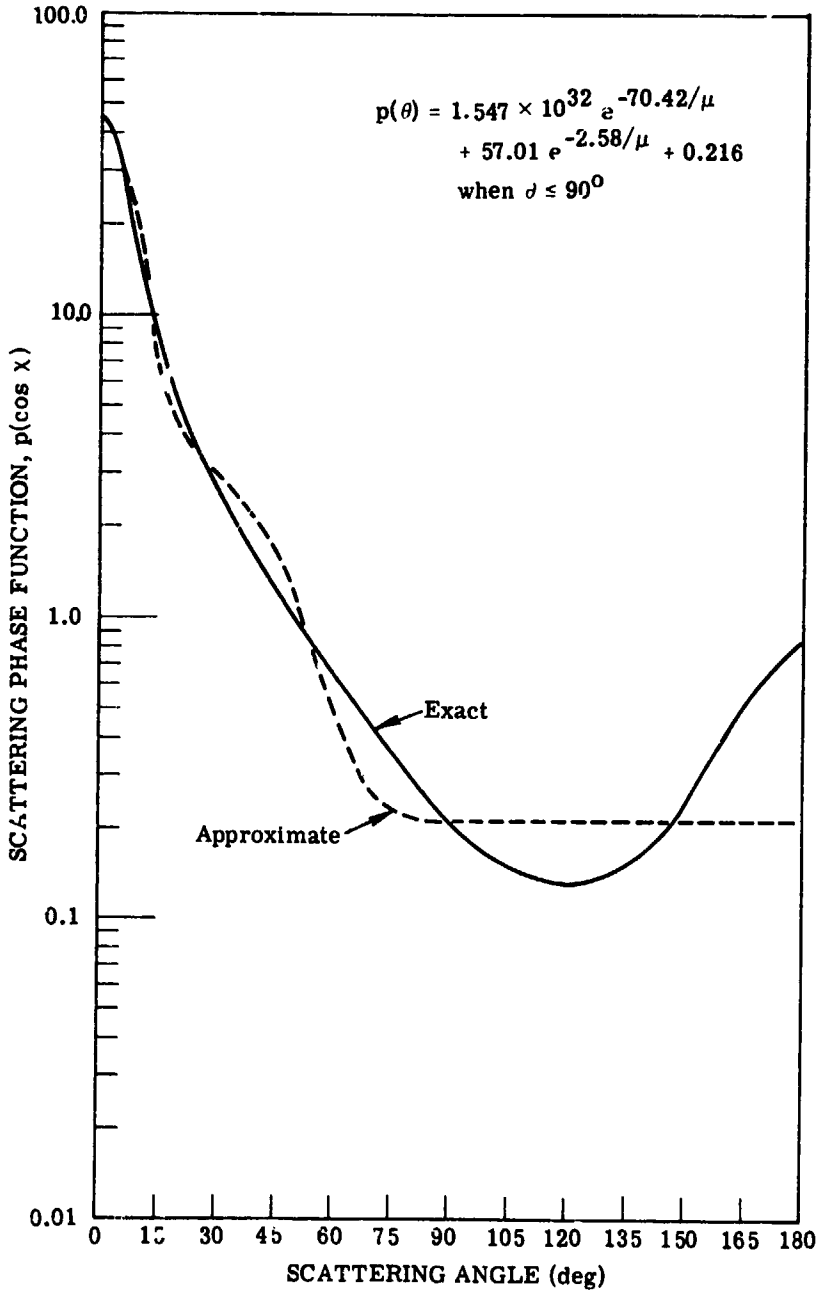

FIGURE 37. EXACT AND APPROXIMATE SCATTERING PHASE FUNCTIONS FOR HAZE L AT A WAVELENGTH OF 0.4μm AND REFRACTIVE INDEX OF 1.5

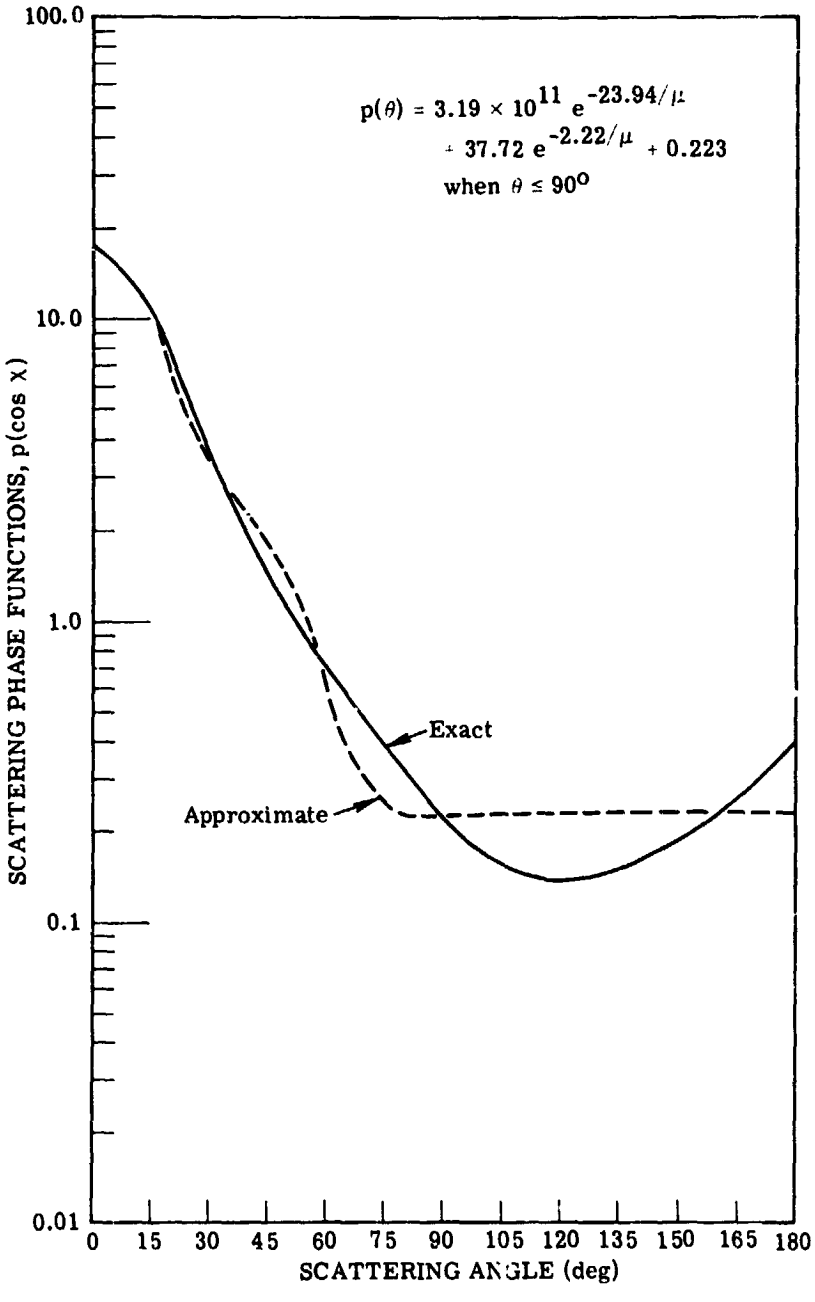

FIGURE 38. EXACT AND APPROXIMATE SCATTERING PHASE FUNCTIONS FOR HAZE L AT A WAVELENGTH OF 0.9μm AND REFRACTIVE INDEX OF 1.5

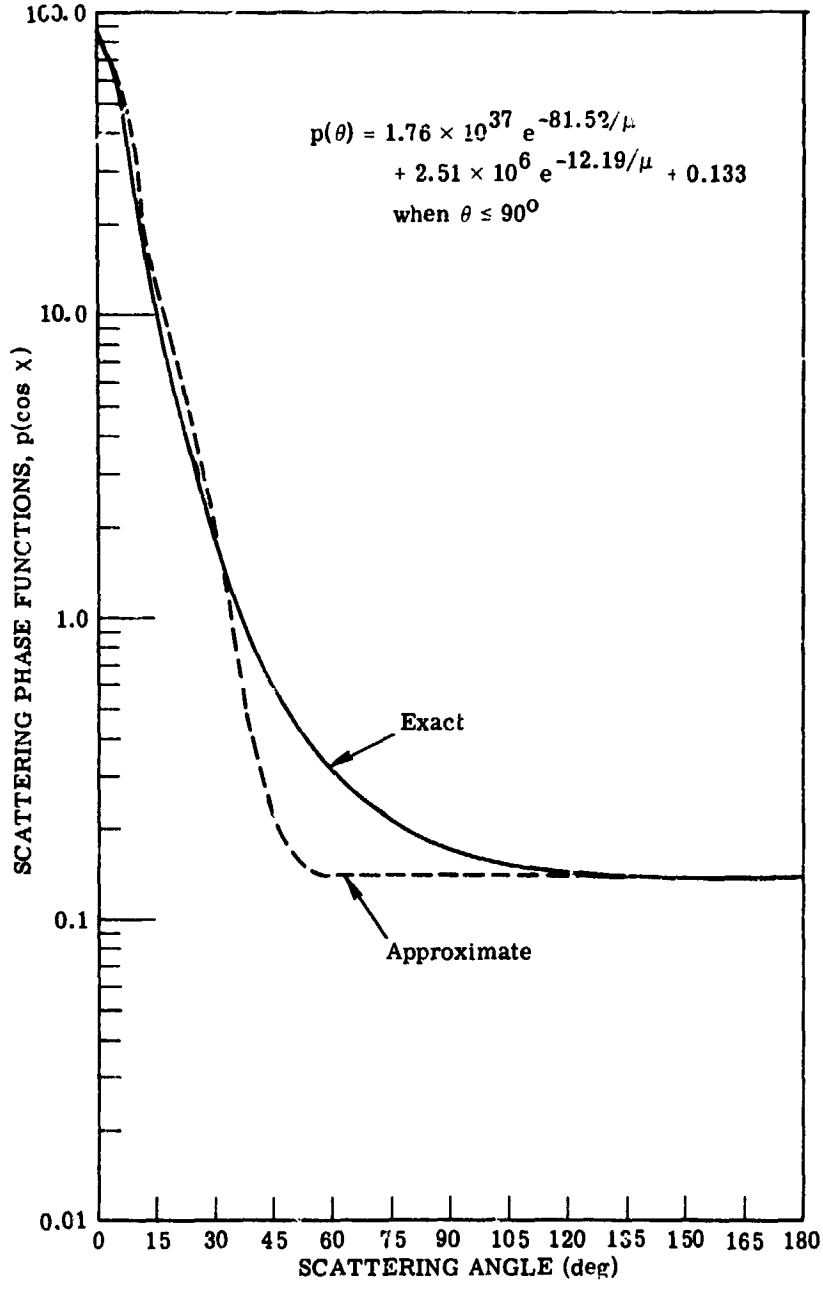

FIGURE 39. EXACT AND APPROXIMATE SCATTERING PHASE FUNCTIONS FOR HAZE L AT A WAVELENGTH OF 0.4μm AND COMPLEX REFRACTIVE INDEX m OF 1.5 - 1.0i

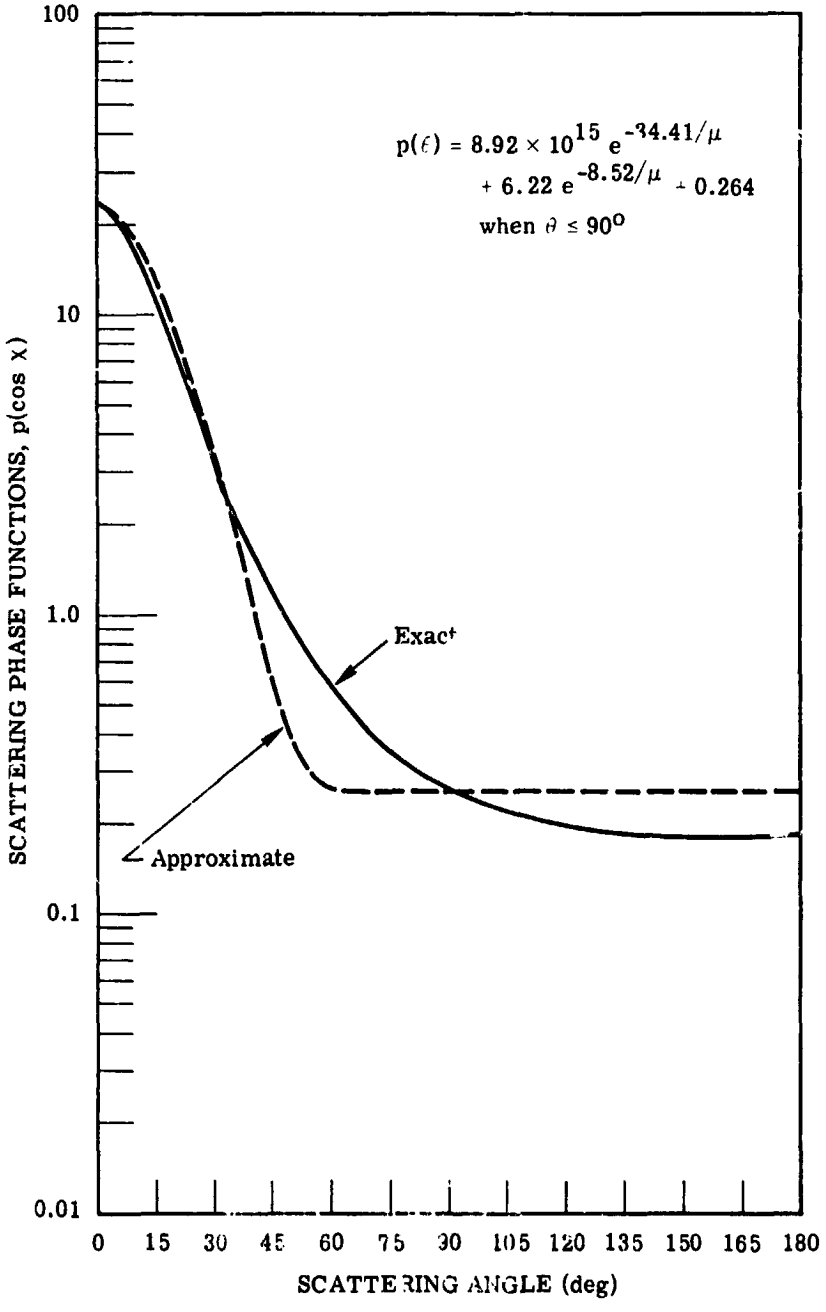

FIGURE 40. EXACT AND APPROXIMATE SCATTERING PHASE FUNCTIONS FOR HAZE L AT A WAVELENGTH OF 0.9μm AND COMPLEX REFRACTIVE INDEX m OF 1.5 - 1.0i

where $\mu_c = \dfrac{z}{\sqrt{z^2 + R^2}}$ (74)

Equation (73) has been used to calculate the singly-scattered surface radiance for combinations of spectrally black, gray, and white disks with black, gray, white, and green vegetational backgrounds. A black surface is assumed to have a reflectance of 0 at all wavelengths, the gray surface a reflectance of 0.5, and the white surface a reflectance of 1.0. The green vegetation background has a reflectance as given in Fig. 41 [30]. For comparison, Fig. 41 also shows the spectral dependence of the extraterrestrial solar irradiance at the top of the atmosphere and the product of that irradiance with the reflectance of green vegetation. The resulting curve represents the spectral dependence of the intrinsic radiance for a green vegetation surface with no atmosphere. As expected, it is dominated by the spectral character of the vegetation, at least for the visible part of the spectrum.

We will now consider the case of black and white surfaces for varying disk radii. It will be assumed that the instantaneous field of view is a circle subtending a half angle of 2.5 mrad at the detector. Thus, at an altitude of 1 km the field of view on the surface is a circle with a radius of 2.5m. The variation in singly-scattered surface radiance with disk radius is illustrated in Fig. 42 for an atmosphere with a light haze. For the case of a white disk and a black background, the sensor "sees" both a small white disk at R = 1m and also a larger circular ring of black surface; in addition, the radiance is low. As disk radius increases, radiance increases until it reaches a value appropriate to a complete white surface. This occurs at a radius of 1 km. The opposite case is also presented, that is when there is a black disk and a white background. At small radii the strong influence of the white background is quite evident, even when the disk has a radius of 10m, or four times the field of view.

The same situation is shown in Fig. 43 for the case of a very hazy atmosphere. Note that the radiances here are almost an order of magnitude greater.

Next, we can see the effect of changing the surface field of view by varying the altitude and keeping the disk radius constant at 12.5m. Consider the case of a white disk with a black background (see Fig. 44): as the altitude increases the radiance increases, since more surface is being observed. However, at an altitude of 5 km the sensor "sees" the beginning of a black surface and the radiance decreases. At an altitude of 10 km the black area is four times the white area and the radiance falls to a very low value. For the case of a black disk and a white background, the radiance gradually increases as a function of altitude up to an altitude of 5 km, indicating the influence of the white background outside the field of view. Beyond 5 km altitude, the sensor "sees" a white surface and the radiance increases rapidly.

In Fig. 45, the same situation is represented, except that the atmosphere is quite hazy An interesting effect becomes evident in this case. As the altitude increases, the radiance

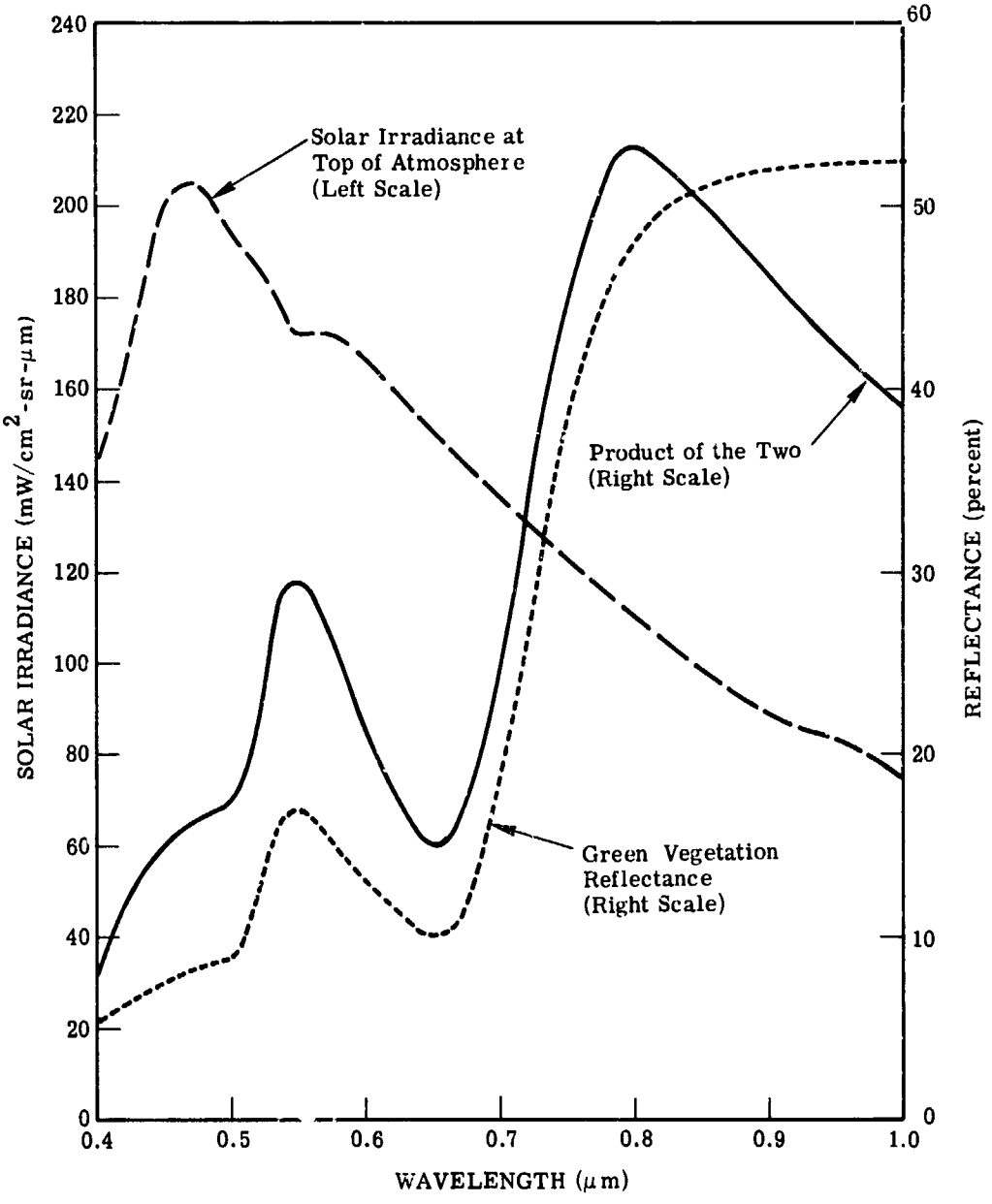

FIGURE 41. WAVELENGTH DEPENDENCE OF SOLAR IRRADIANCE AT TOP OF ATMOSPHERE, GREEN VEGETATION REFLECTANCE, AND THE PRODUCT OF THE TWO

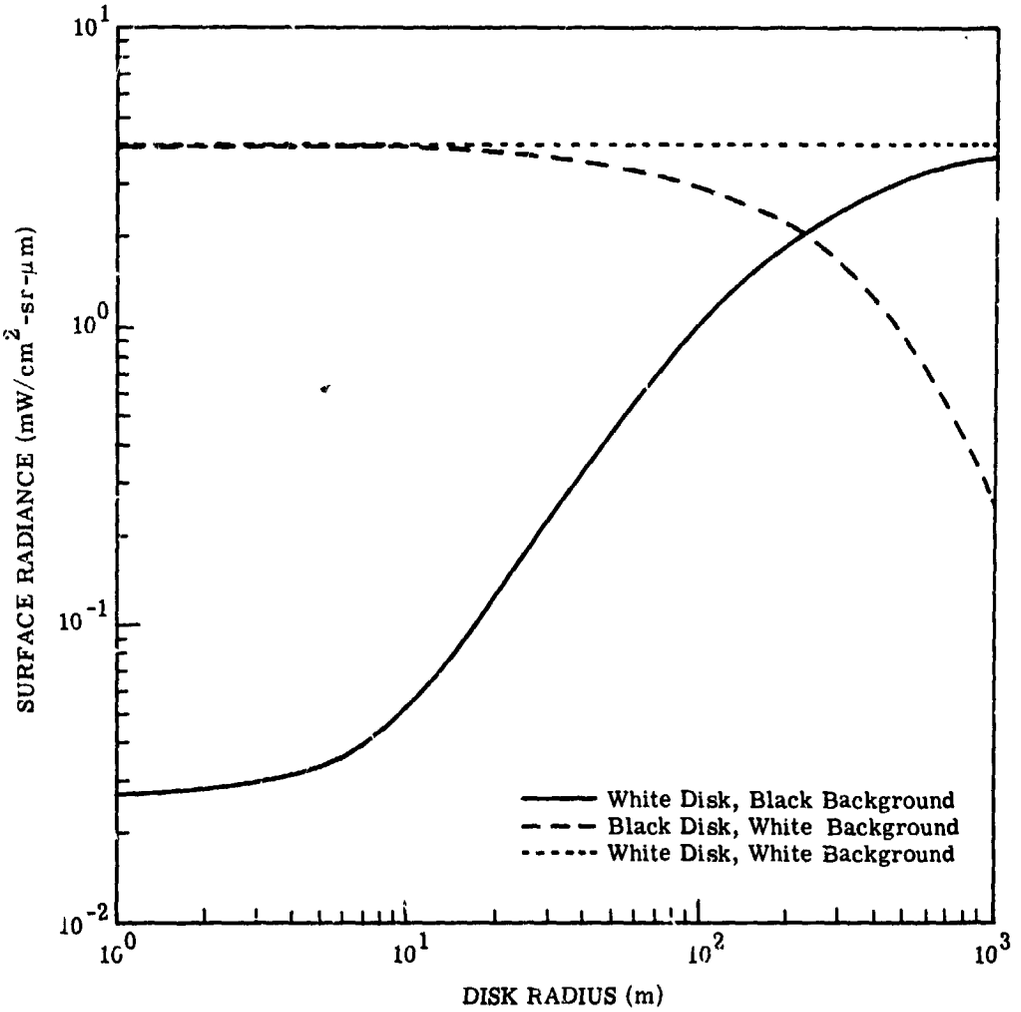

FIGURE 42. DEPENDENCE OF SINGLY SCATTERED SURFACE RADIANCE ON DISK RADIUS. Visual range = 23 km, altitude = 1 km, wavelength = 0.55μm, solar zenith angle = 45°, nadir view angle = 0°.

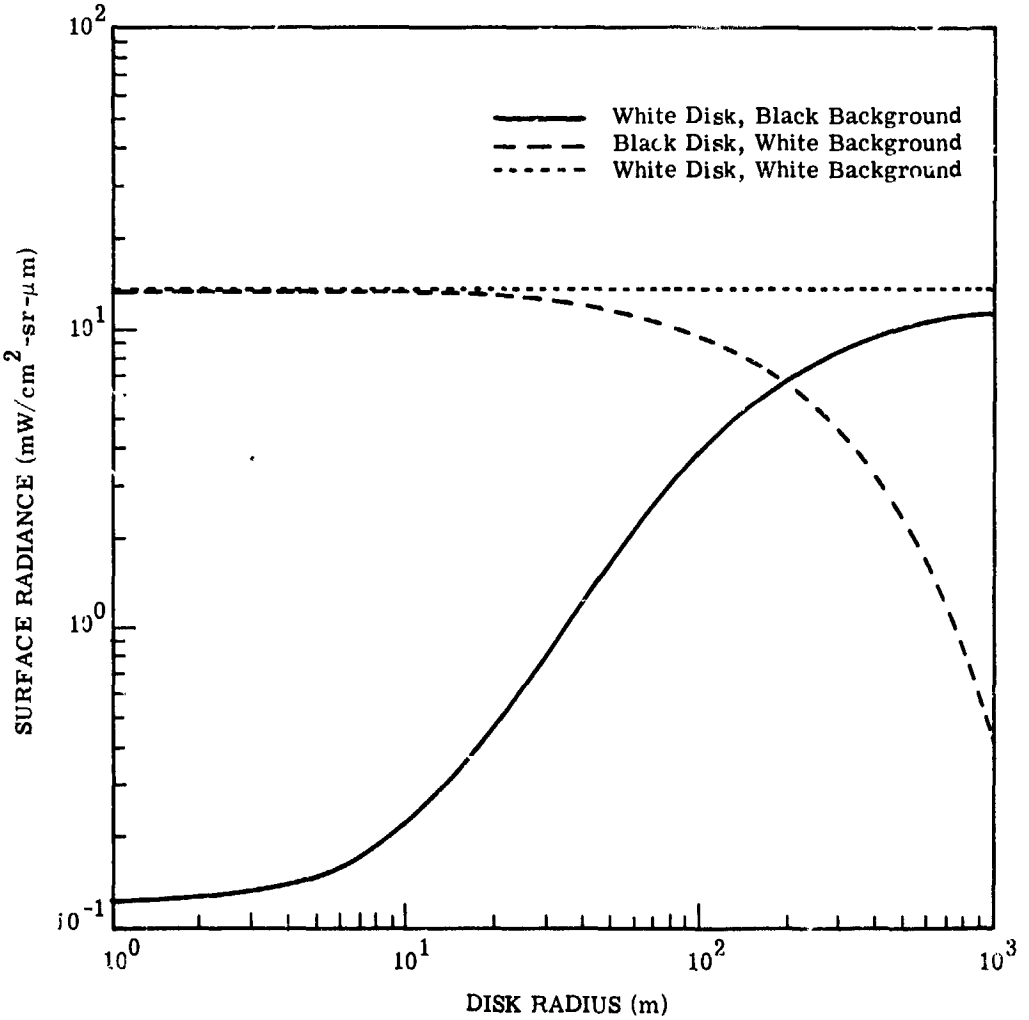

FIGURE 43. DEPENDENCE OF SINGLY SCATTERED SURFACE RADIANCE ON DISK RADIUS. Visual range = 2 km, altitude = 1 km, wavelength = 0.55μm, solar zenith angle = 45^o, nadir view angle = 0^o.

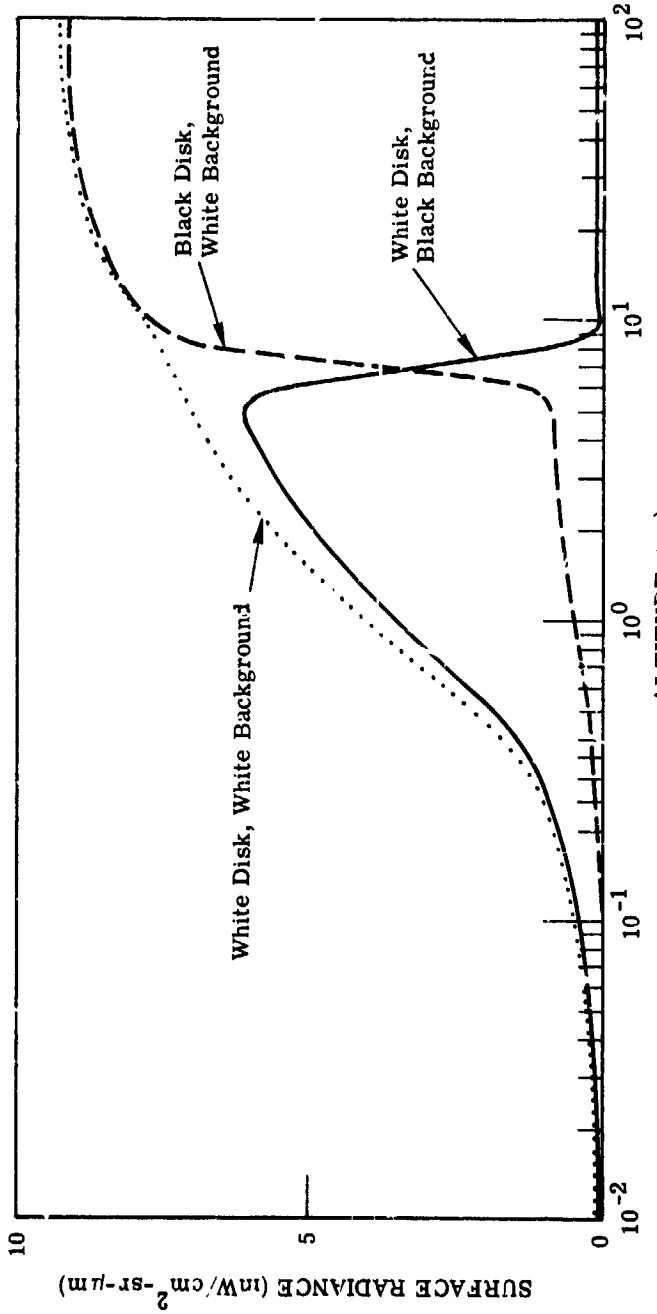

FIGURE 44. DEPENDENCE OF SINGLY SCATTERED SURFACE RADIANCE ON ALTITUDE. Visual range = 23 km, wavelength = 0.55μm, no absorption, solar zenith angle = 45°, nadir view angle = 0°, disk radius = 12.5m.

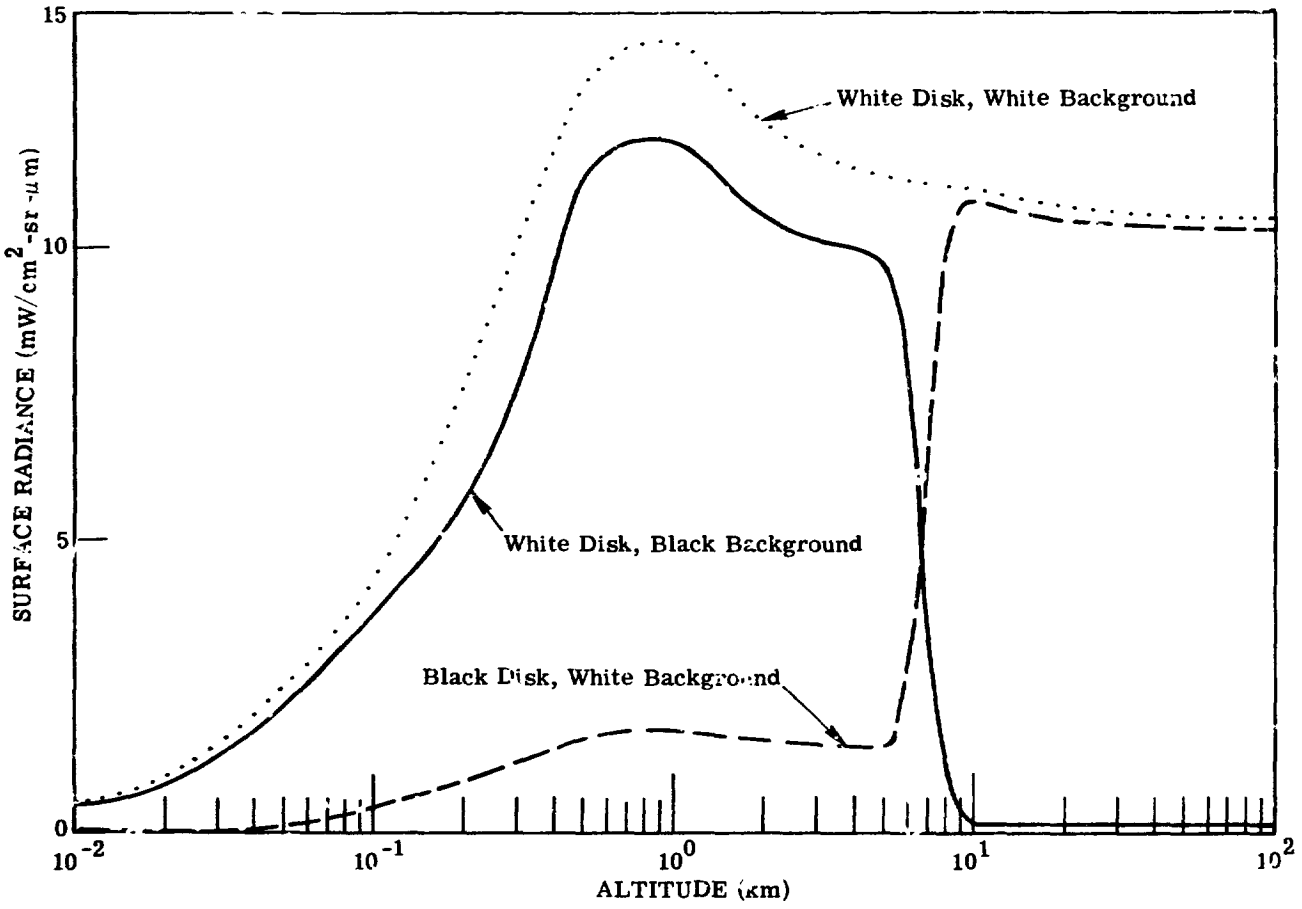

FIGURE 45. DEPENDENCE OF SINGLY SCATTERED SURFACE RADIANCE ON ALTITUDE. Visual range = 2 km, wavelength = 0.55μm, no absorption, solar zenith angle = 45°, nadir view angle = 0°, disk radius = 12.5m.

from a white disk increases up to an altitude of about 0.9 km, after which it gradually decreases. This is due to the fact that as altitude increases, more radiation is included in the acceptance cone of the sensor. However, attenuation is also taking place. As a result, after a certain altitude more radiation is lost by scattering out of the field of view than is being scattered into the field of view. At an altitude of 5 km, for example, the sensor "sees" the black surface and the radiance decreases more rapidly. A similar effect is noted for the case of a black disk with a white background.

We now turn to the cases of black, gray, and white disks with a background of green vegetation. Figure 46 illustrates the variation in singly-scattered radiance with wavelength for the case of a black disk. Referring to Fig. 41, we see that the radiance essentially has the spectral dependence of the product curve for all disk radii. For radii of 10m and 100m, the actual scattering phase function is greater than the isotropic phase function for all angles appropriate to those disks; hence the radiances are greater. For a disk radius of 1000m, however, the maximum angle of scattering at the edge of the disk is 45°. At this angle the actual phase function is almost the same as the isotropic phase function; therefore, the radiances for the isotropic and the anisotropic cases are almost equal.

Figure 47 illustrates the same situation, except for a white disk. Here the curves are reversed as far as radius is concerned. For large radii the curves have a general behavior characteristic of the solar spectrum because the effect of the vegetation background is small; for a radius of 10m, however, the effect of the vegetation becomes noticeable. The anisotropic case has more spectral variation than the isotropic because the actual scattering phase functions of the former are dependent upon wavelength, whereas the isotropic phase function of the latter has no spectral dependence.

We can now simulate the case of a sensor in space or at an altitude of 50 km, which for all practical purposes is at the top of the atmosphere. Figure 48 illustrates the spectral dependence of singly-scattered surface radiance as a function of disk radius for a gray disk. Here the effect of background on target is clear. The field of view is a circle with a radius of 125m. For radii smaller than this, green vegetation as well as the gray disk can be seen; in addition, the curve has the spectral dependence of green vegetation. At a radius of 1000m the dependence is more closely related to the solar spectrum.

Figure 49 shows the same effect as for the previous figure, except that the atmosphere is very hazy. In this case the radiance is lower at shorter wavelengths because of the greater probability of scattering out of the field of view.

In Fig. 50 we see the variation of singly-scattered surface radiance with wavelength for black, gray, and white disks, each with a radius of 1000m. For a black disk the only spectral variation that can arise is from the green vegetation background. The rather large 50-percent

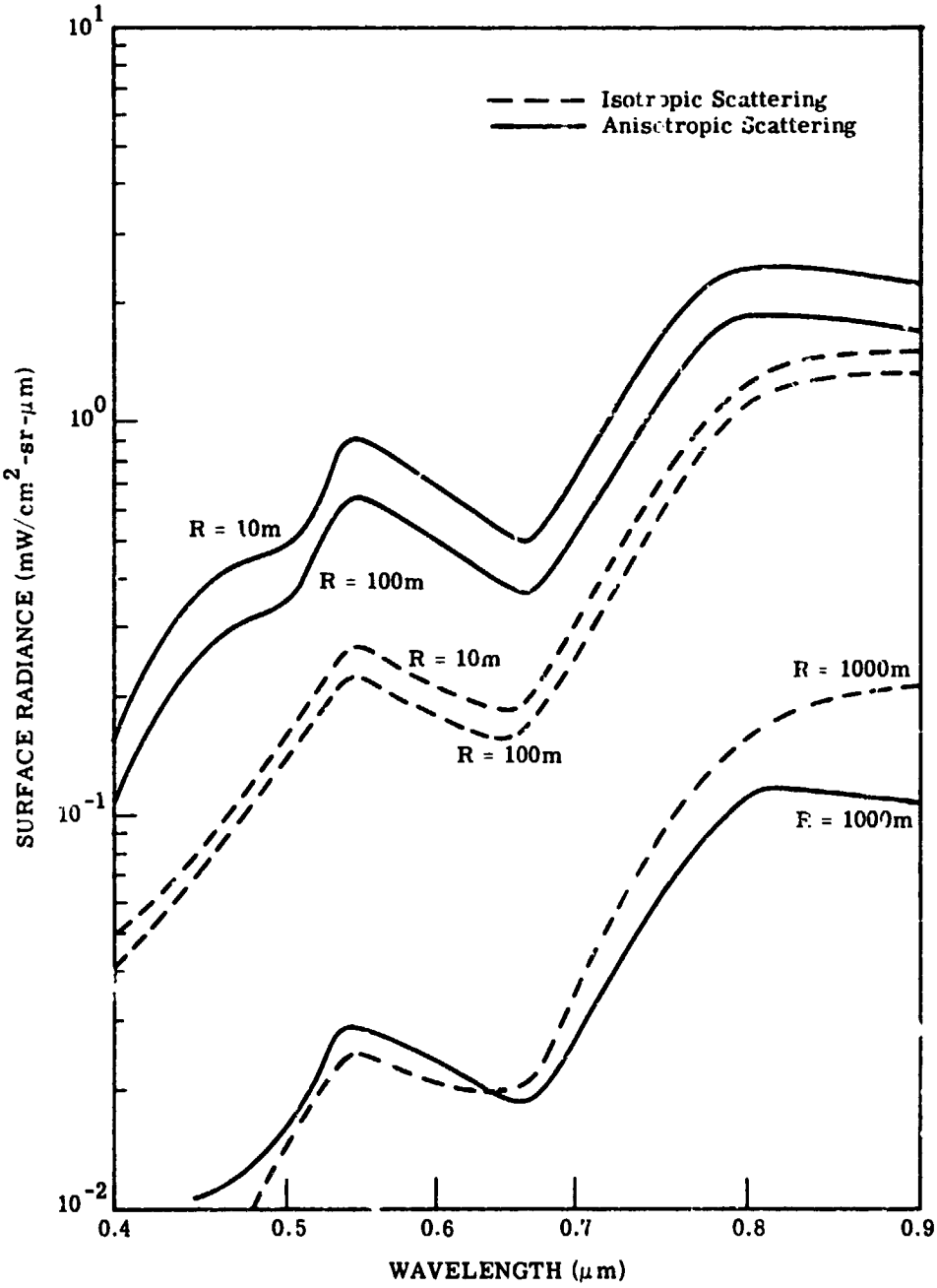

FIGURE 48. DEPENDENCE OF SINGLY SCATTERED SURFACE RADIANCE ON WAVELENGTH FOR A BLACK DISK AND GREEN VEGETATION. No absorption, solar zenith angle = 45°, nadir viewing, ϕ = 0°, visual range = 2 km, altitude = 1 km.

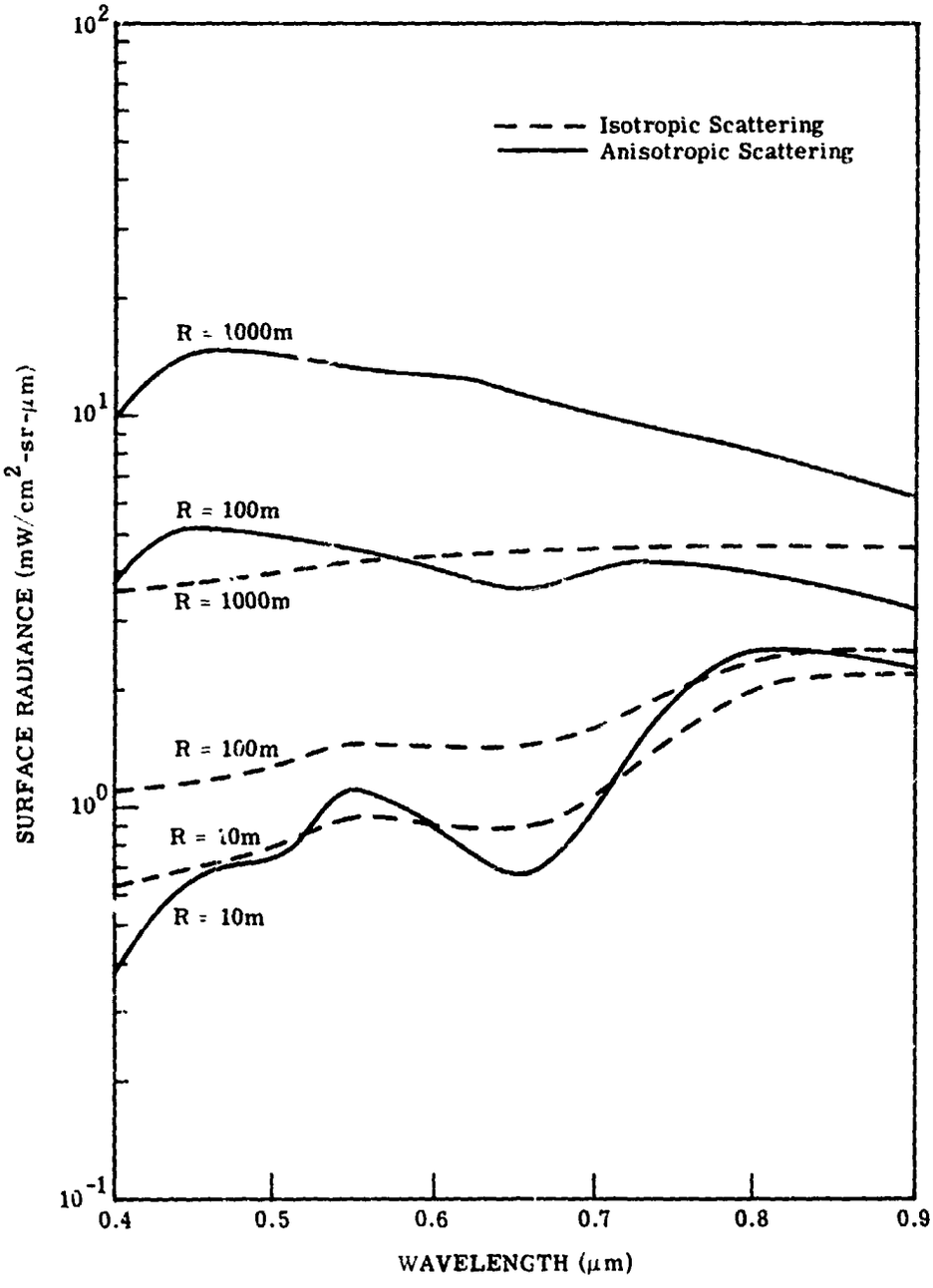

FIGURE 47. DEPENDENCE OF SINGLY SCATTERED SURFACE RADIANCE ON WAVELENGTH FOR A WHITE DISK AND GREEN VEGETATION BACKGROUND. No absorption, solar zenith angle = 45°, nadir view angle = 0°, visual range = 2 km, altitude = 1 km.

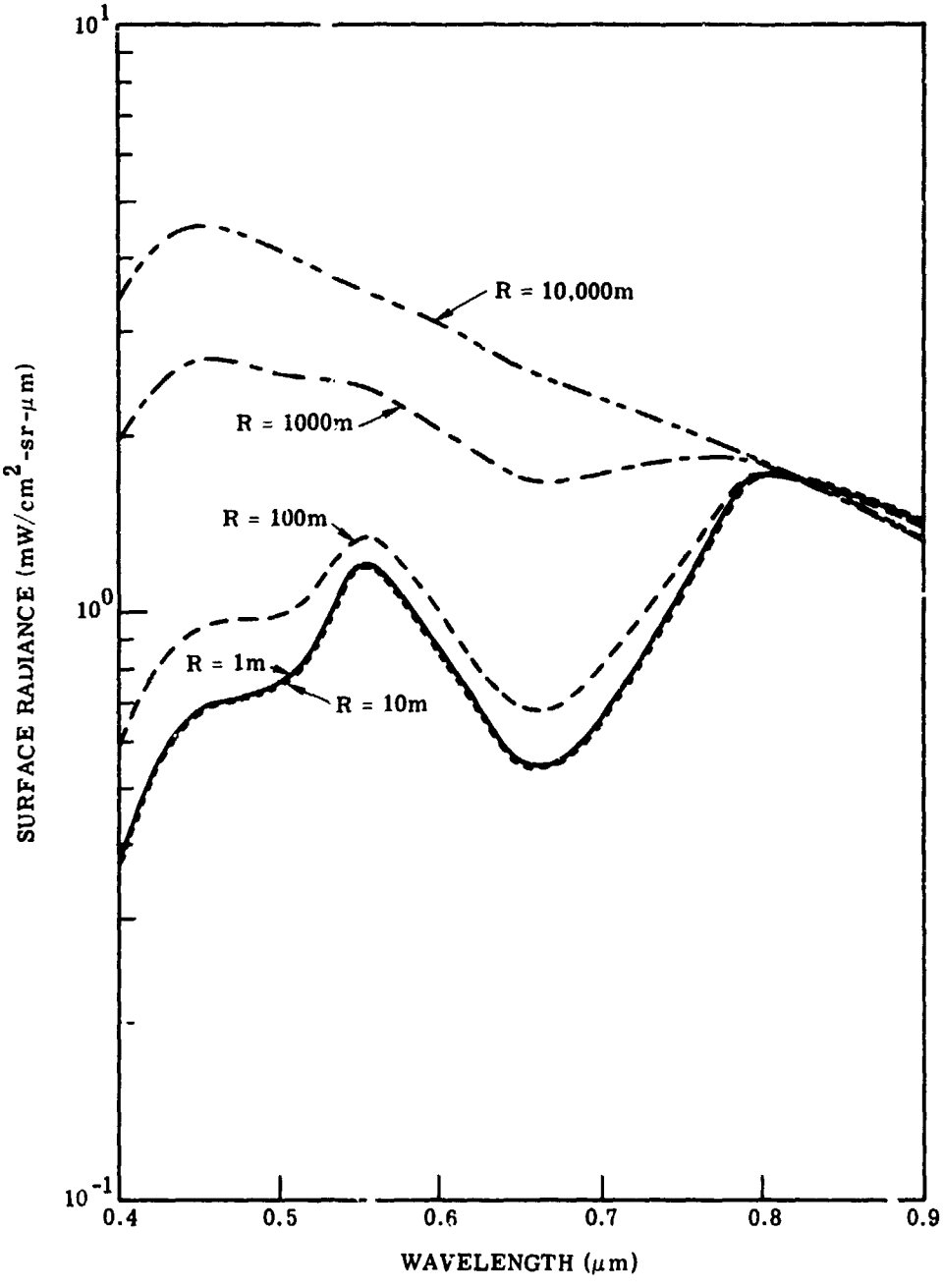

FIGURE 48. DEPENDENCE OF SINGLY SCATTERED SURFACE RADIANCE ON WAVELENGTH AT 50 km ALTITUDE FOR VARIOUS DISK RADII. Visual range = 23 km, no absorption, solar zenith angle = 45°, nadir view angle = 0°, disk reflectance = 0.5, background reflectance = green vegetation.

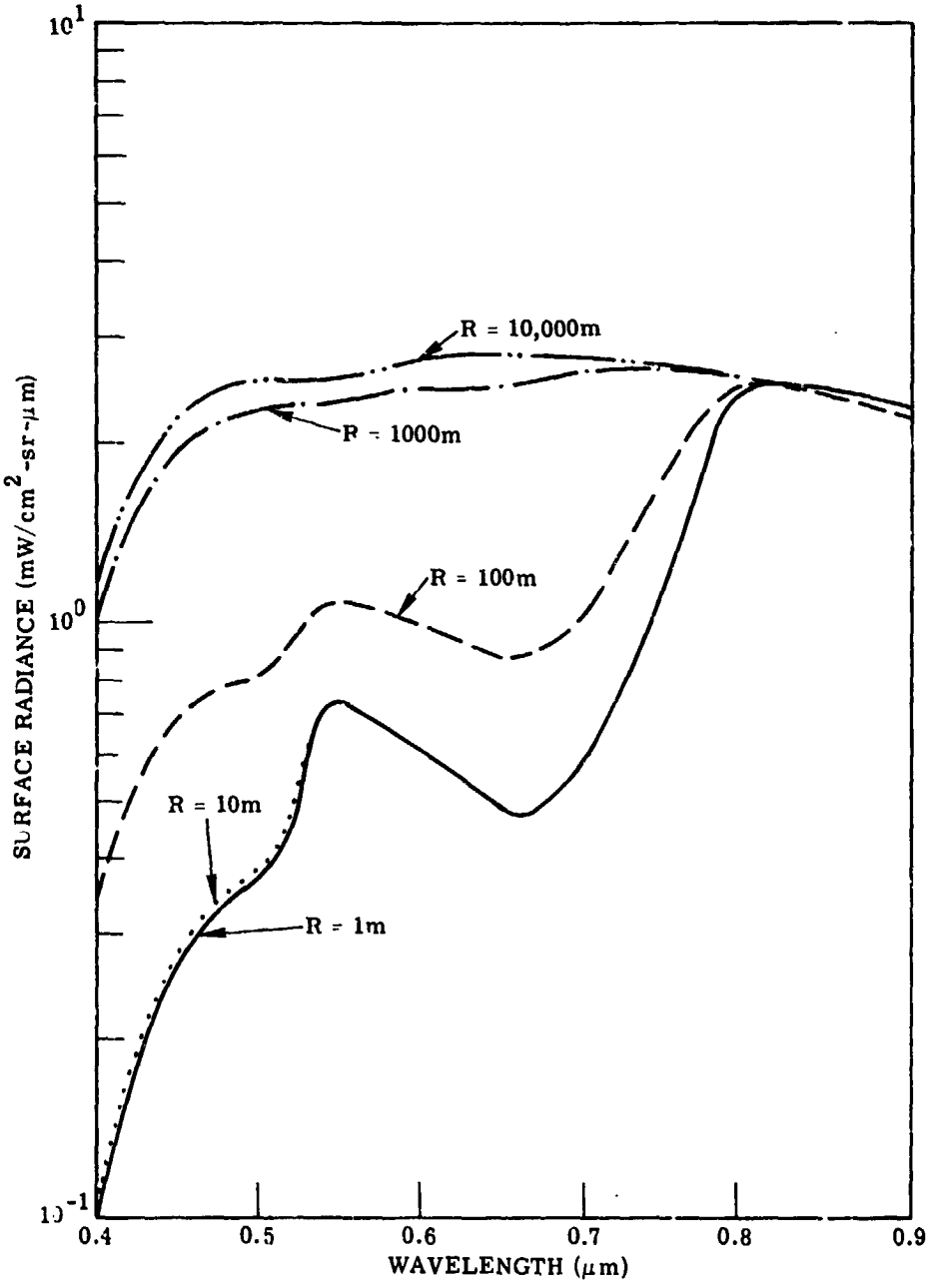

FIGURE 49. DEPENDENCE OF SINGLY SCATTERED SURFACE RADIANCE ON WAVELENGTH AT 50 km ALTITUDE FOR VARIOUS DISK RADII. Visual range = 2 km, no absorption, solar zenith angle = 45°, nadir view angle = 0°, disk reflectance = 0.5, background reflectance = green vegetation.

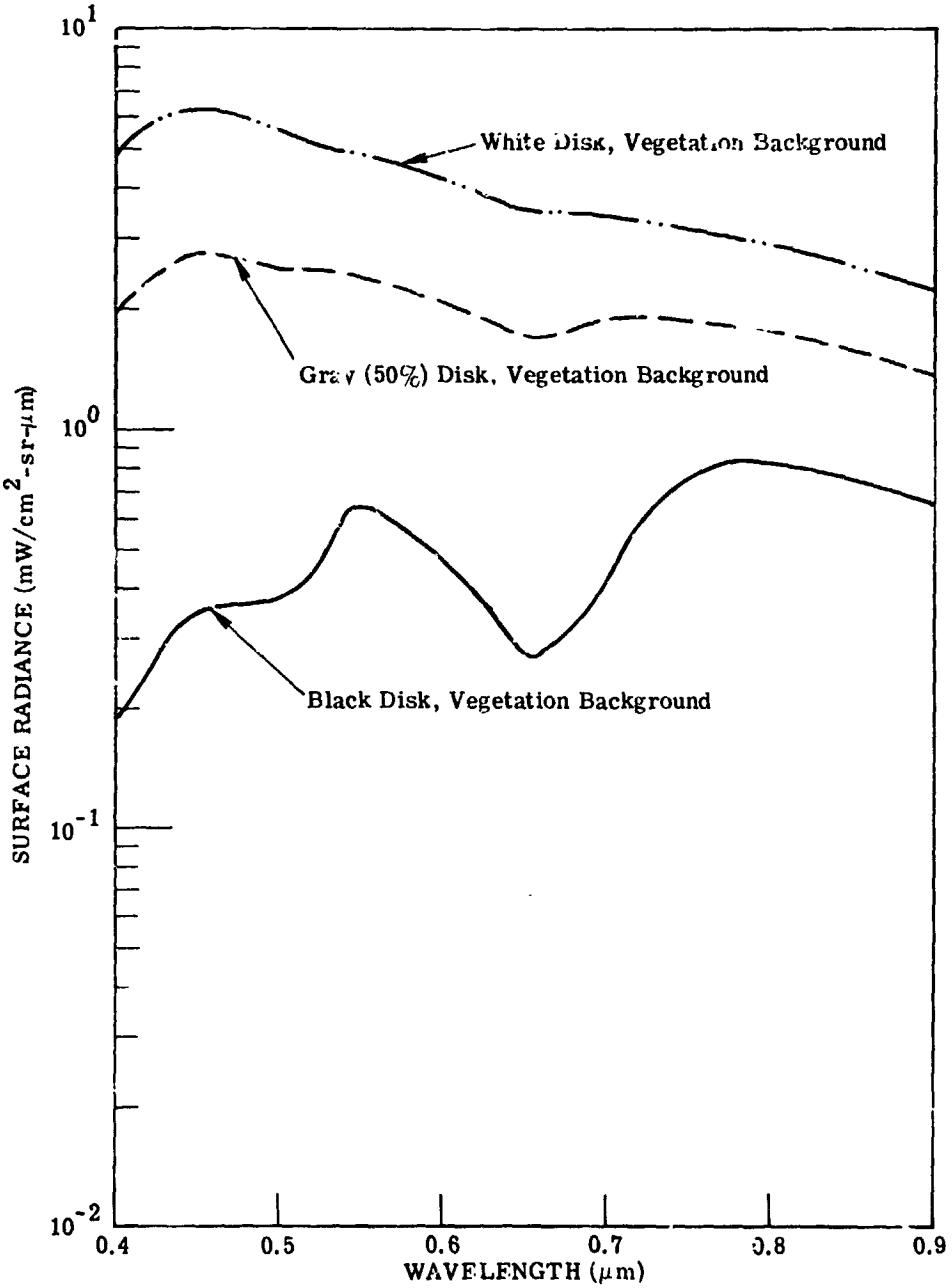

FIGURE 50. DEPENDENCE OF SINGLY SCATTERED SURFACE RADIANCE ON WAVELENGTH FOR VARIOUS DISK REFLECTANCES. Visual range = 23 km, no absorption, altitude = 50 km, solar zenith angle = 45°, nadir view angle = 0°, disk radius = 1000 m.

gray disk removes this spectral variation and therefore the radiance is essentially the same as that for a white disk except for magnitude.

Figure 51 illustrates the same situation, except for a very hazy atmosphere. Again, the radiance at shorter wavelengths is lower due to high attenuation.

Finally, we can compare the various radiance components (that is, the singly-scattered sky radiance, the doubly-scattered sky radiance, the singly-scattered surface radiance, and the sum of these three components) for a black disk and a green vegetation background (Fig. 52). The singly-scattered sky radiance is calculated using the actual scattering phase function; the doubly-scattered sky radiance is determined using the isotropic phase function; and the singly-scattered surface radiance found via the exponential phase-function approximation. The only spectral variation in the sky radiances arises from the solar spectrum. The surface term is small compared to the other radiances, but this is true only because the black disk is so large. For smaller disks the surface radiance increases (as was seen in Fig. 46). Thus, the influence of outside reflectance is significant for various disk reflectances and sizes.

Figure 53 illustrates the same condition, except for a very hazy atmosphere. In this case, the surface term is less important—an effect which is surprising. However, this is for a sensor at a 50 km-altitude, where the sky radiances are larger than at lower altitudes.

In conclusion, we can say that background surface definitely affects target radiance, the amount depending upon the relative size of the target and the field of view. For most cases, the anisotropy of scattered radiation is not too important as far as magnitudes of radiance are concerned; it is important, however, for the consideration of spectral dependence.

6.3 THE INFINITE STRIP PROBLEM

Only in the last few years have investigators tried to find solutions to the multidimensional transport equation. Approximate methods using Fourier transforms have been developed by Williams [34], Garrettson and Leonard [35], Kuper [36], Erdmann and Sotoodehnia [37], and Rybicki [38]. We shall use a similar technique to solve the two-dimensional radiative-transfer equation for an infinite strip.

Consider an infinite strip with a reflectance ρ and a background with reflectance $\bar{\rho}$, as illustrated in Fig. 54. The position vector $\vec{R}$ is

$$\vec{R} = (x, y, z) = R(\sin\eta\cos\psi, \sin\eta\ \sin\psi, \cos\eta) \tag{75}$$

and the unit vector $\hat{\Omega}$ is

$$\hat{\Omega} = (\Omega_x, \Omega_y, \Omega_z) = (\sin\theta\cos\phi, \sin\theta\sin\phi, \cos\theta) = (\xi, \nu, \mu) \tag{76}$$

The radiative-transfer equation becomes

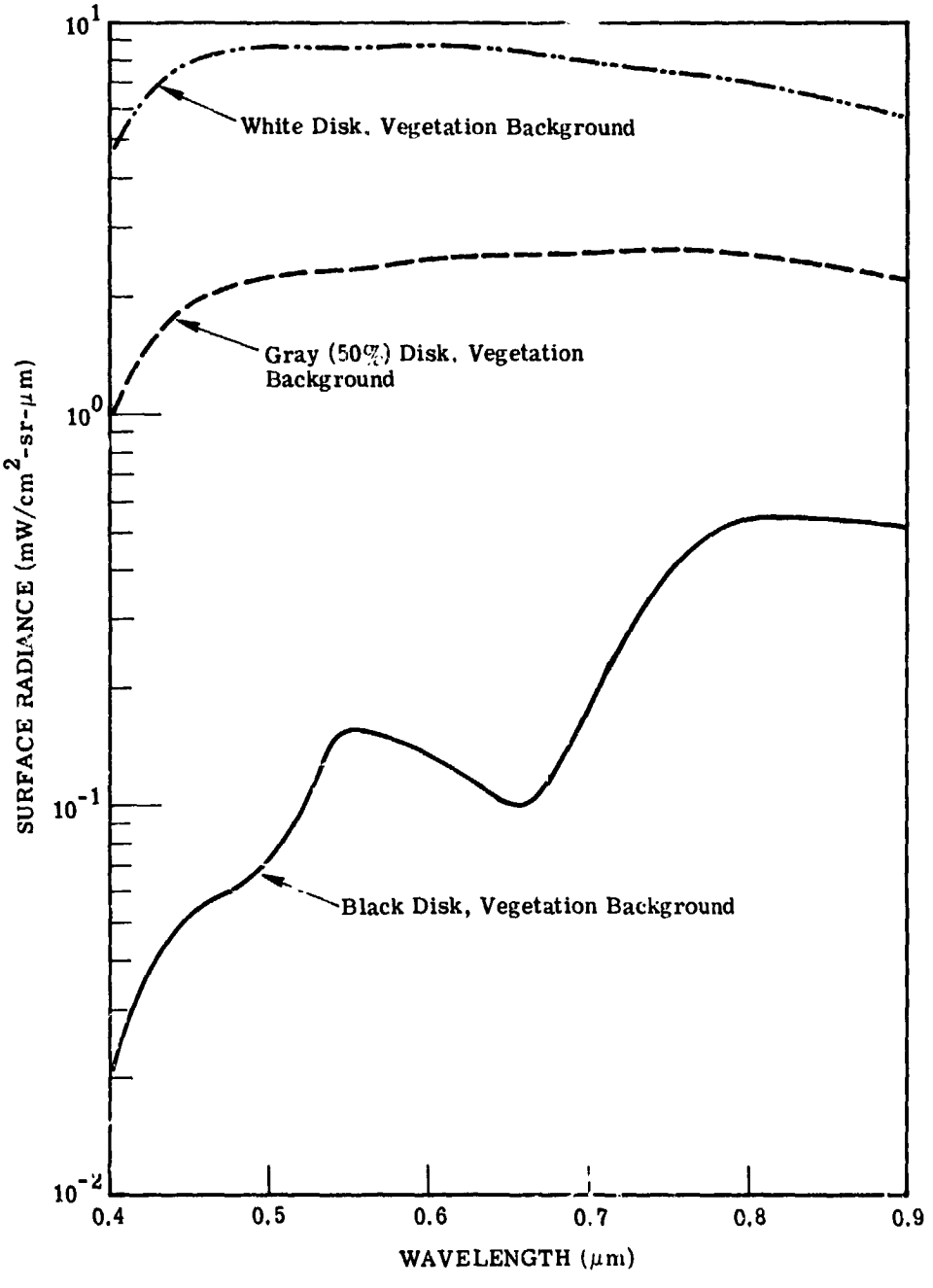

FIGURE 51. DEPENDENCE OF SINGLY SCATTERED SURFACE RADIANCE ON WAVELENGTH FOR VARIOUS DISK REFLECTANCES. Visual range = 2 km, no absorption, altitude = 50 km, solar zenith angle = 45°, nadir view angle = 0°, disk radius = 1000m.

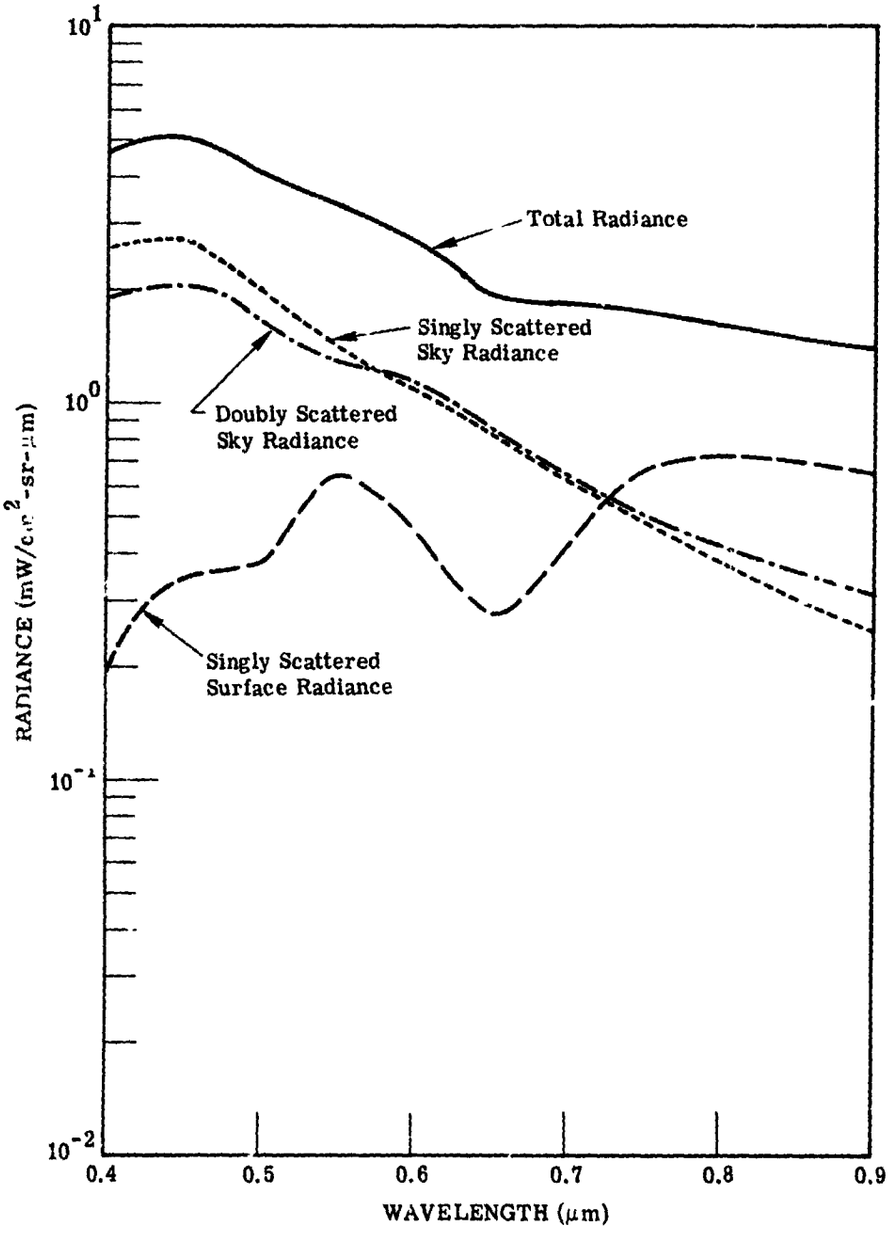

FIGURE 52. DEPENDENCE OF RADIANCES ON WAVELENGTH. Visual range = 23 km, no absorption, solar zenith angle = 45°, nadir view angle = 0°, disk reflectance = 0, background reflectance = green vegetation, disk radius = 1000m, altitude = 50 km.

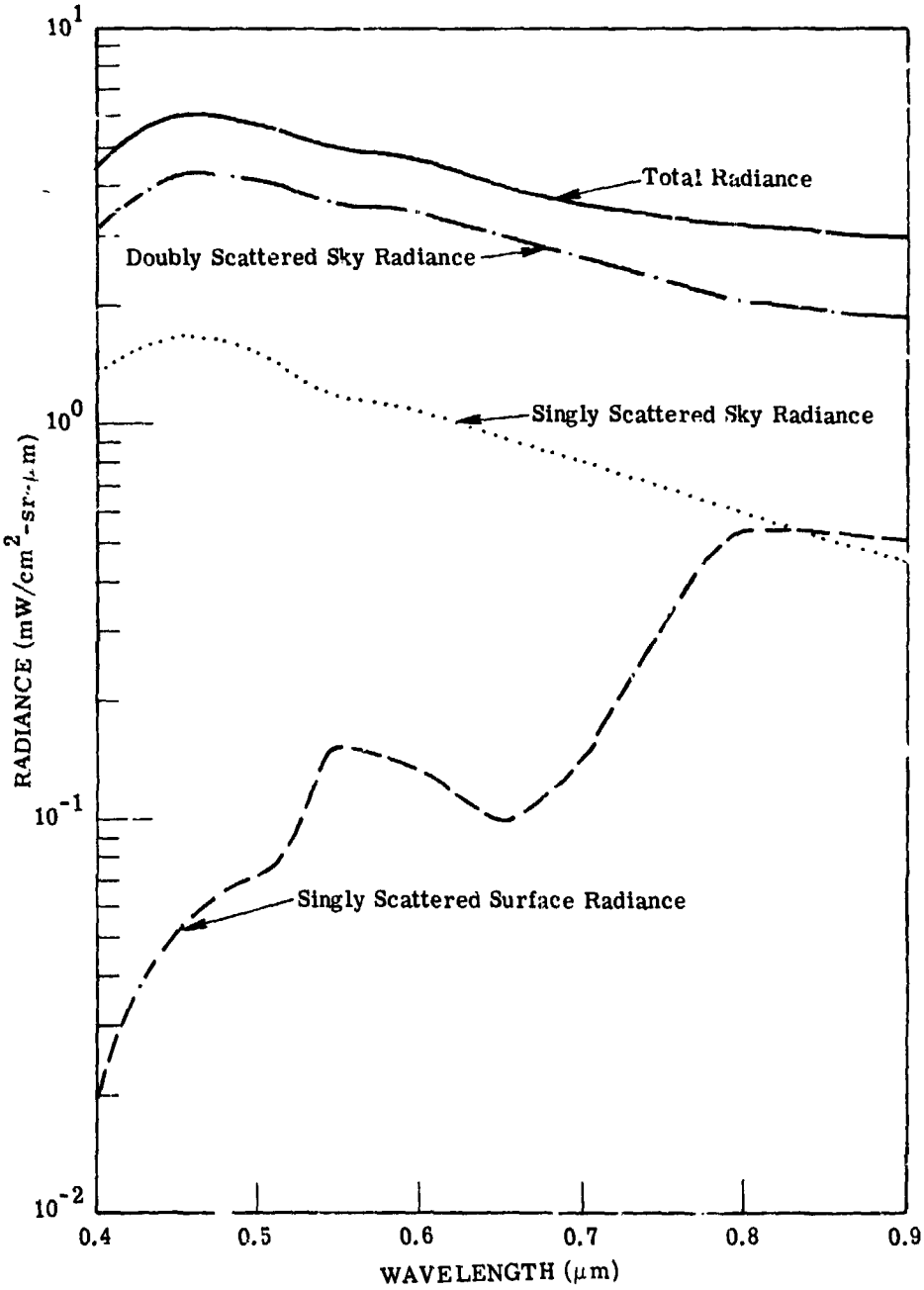

FIGURE 53. DEPENDENCE OF RADIANCES ON WAVELENGTH. Visual range = 2 km, no absorption, solar zenith angle = 45°, nadir view angle = 0°, disk reflectance = 0, background reflectance = green vegetation, disk radius = 1000m, altitude = 50 km.

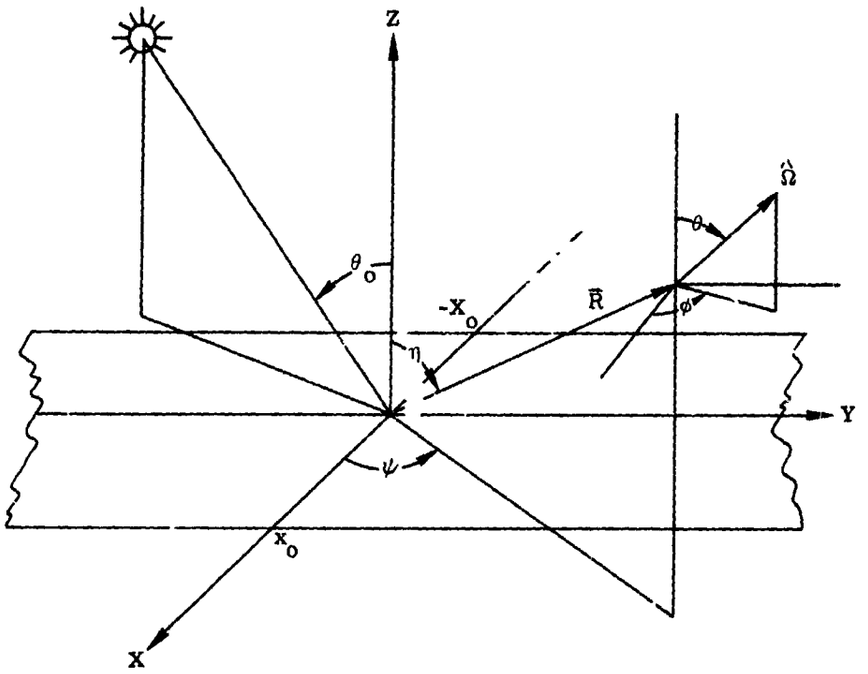

FIGURE 54. INFINITE STRIP APPROXIMATION

$$\xi\frac{\partial L}{\partial x} + \mu\frac{\partial L}{\partial z} = -\kappa(z)L(x, z, \mu, \phi) + \frac{\beta(z)}{4\pi}E_o e^{-\tau/\mu_o} p(\mu, \phi, -\mu_o, \phi_o)$$

$$+ \frac{\beta(z)}{4\pi}\int_0^{2\pi}\int_{-1}^{1} p(\mu, \phi, \mu', \phi')L(x, z, \mu', \phi')\,d\mu'\,d\phi' \qquad (76)$$

We can now define a Fourier transfer for the x coordinate,

$$\tilde{L}(k, z, \mu, \phi) = \int_{-\infty}^{\infty} e^{ikx} L(x, z, \mu, \phi)\,dx \qquad (78)$$

with an inverse

$$L(x, z, \mu, \phi) = \frac{1}{2\pi}\int_{-\infty}^{\infty} e^{-ikx}\tilde{L}(k, z, \mu, \phi)\,dk \qquad (79)$$

Taking the Fourier transform of Eq. (77) leads to the following equations:

$$\tilde{L}(k, z, \mu, \phi) = \tilde{L}(k, 0, \mu, \phi)e^{-(\tau_o - \tau - \epsilon z)/\mu}$$

$$- \frac{2\pi\epsilon}{\mu}\delta(k)\int_0^z e^{[\tau - \tau' + \epsilon(z - z')]/\mu} L(\infty, z', \mu, \phi)\,dz'$$

$$+ \frac{\delta(k)}{2\mu}E_o p(\mu, \phi, -\mu_o, \phi_o)\int_0^z \beta(z')e^{-\tau'/\mu_o} e^{[\tau - \tau' + \epsilon(z - z')]/\mu}\,dz'$$

$$+ \frac{1}{4\pi\mu}\int_0^{2\pi}\int_{-1}^{1} p(\mu, \phi, \mu', \phi')\int_0^z \beta(z')e^{[\tau - \tau' + \epsilon(z - z')]/\mu}\tilde{L}(k, z', \mu', \phi')\,d\mu'\,d\phi'\,dz' \qquad (80)$$

$$\tilde{L}(k, z, -\mu, \phi) = -\frac{2\pi\epsilon}{\mu}\delta(k)\int_z^{\infty} e^{[\tau' - \tau + \epsilon(z' - z)]/\mu} L(\infty, z', -\mu, \phi)\,dz'$$

$$+ \frac{\delta(k)E_o p(-\mu, \phi, -\mu_o, \phi_o)}{2\mu}\int_z^{\infty} \beta(z')e^{-\tau'/\mu_o} e^{[\tau' - \tau + \epsilon(z' - z)]/\mu}\,dz'$$

$$+ \frac{1}{4\pi\mu}\int_0^{2\pi}\int_{-1}^{1} p(-\mu, \phi, \mu', \phi')\int_z^{\infty} \beta(z')e^{[\tau' - \tau + \epsilon(z' - z)]/\mu}\tilde{L}(k, z', \mu', \phi')\,d\mu'\,d\phi'\,dz' \qquad (81)$$

where $\epsilon = ik\xi = ik\sqrt{1-\mu^2}\cos\phi$, and $L(\infty, z, \mu, \phi)$ and $L(\ , z, -\mu, \phi)$ are the asymptotic solutions which coincide with solutions for the one-dimensional problem. By iterating the above equations, applying the boundary conditions, and then by taking the inverse Fourier transform, one obtains the solution for the two-dimensional equation. This has been done, but the resulting mathematical expressions are too involved to be presented here, except for the most interesting part dealing with the surface term. Let us consider that term.

For a Lambertian surface, $\tilde{L}(k, 0, \mu, \phi) = \tilde{L}(k, 0)$, and the iterated (first) term becomes

$$\tilde{L}(k, z, \mu, \phi) = \frac{1}{4\pi\mu}\int_0^{2\pi}\int_0^1 p(\mu, \phi, \mu', \phi')\int_0^z \beta(z')\exp\left[\tau - \tau' + \epsilon(z - z')\right]/\mu\, \tilde{L}(k, 0)$$

$$\times \exp\left[-\tau_o - \tau' - \epsilon' z'\right]/\mu'\, d\mu'\, d\phi'\, dz' \tag{82}$$

The integration over ϕ' is

$$\int_0^{2\pi} \exp(\epsilon' z'/\mu')\, d\phi' = 2\pi J_o\left[\frac{z' k\sqrt{1-\mu'^2}}{\mu'}\right] \tag{83}$$

where J_o is the zero-th order Bessel function. Now, let us represent the scattering phase function by

$$p(\mu, \phi, \mu', \phi') = \sum_{j=1}^{n} C_j \frac{e^{-\lambda_j/\mu'}}{\mu'}; \quad \mu \to 1 \tag{84}$$

Hence,

$$\tilde{L}(k, z, 1, \phi) = \frac{\tilde{L}(k, 0)}{2}\sum_{j=1}^{n} C_j \int_0^z \beta(z') e^{\tau - \tau'} \int_0^1 \frac{e^{-\alpha/\mu'}}{\mu'^2} J_o\left[\frac{kz'\sqrt{1-\mu'^2}}{\mu'}\right] d\mu'\, dz' \tag{85}$$

where $\alpha = \lambda_j + \tau_o - \tau'$

The integration over μ' can easily be accomplished by using a Laplace transform:

$$\tilde{L}(k, z, 1, \phi) = \frac{\hat{L}(k, 0)}{2}\sum_{j=1}^{n} C_j \int_0^z \beta(z') e^{\tau - \tau'} \frac{e^{-\sqrt{\alpha^2 + k^2 z'^2}}}{\sqrt{\alpha^2 + k^2 z'^2}}\, dz' \tag{86}$$

It can be shown* that

*See Appendix A.

$$\tilde{L}(k, 0) = 2\pi\left\{\frac{\bar{\rho}E(\bar{\rho})\delta(k)}{\pi} + [\rho E(\rho) - \bar{\rho}E(\bar{\rho})]\frac{\sin kx_o}{k}\right\} \tag{87}$$

Taking the inverse Fourier transform of Eq. (86) then leads to the following:

$$L(x, z, 1, \psi) = \frac{\bar{\rho}E(\bar{\rho})}{2\pi}e^{-(\tau_o-\tau)}\sum_{j=1}^{n}C_j e^{-\lambda_j}\int_0^z \frac{\beta(z')}{\lambda_j + \tau_o - \tau'}dz'$$

$$+ \frac{[\rho E(\rho) - \bar{\rho}E(\bar{\rho})]}{2\pi}\sum_{j=1}^{n}C_j\int_0^z \frac{\beta(z')}{z'}e^{\tau-\tau'}[M(z', x + x_o) - M(z', x - x_o)]\,dz' \tag{88}$$

where

$$M(z', \zeta) = \int_0^{\zeta} K_o\left[\alpha\sqrt{(\zeta/z')^2 + 1}\right]d\zeta \tag{89}$$

in which K_o is the modified Bessel function. The limits for M are

$$M(z', 0) = 0; \quad M(z', \infty) = \pi e^{-\alpha z'} \tag{90}$$

Therefore, the numerical integration of Eq. (88) will give the spectral radiance for a downward-looking observer at any point in the atmosphere. In particular, we would be able to simulate the response of a sensor as it passes over a natural boundary between two dissimilar surfaces

7
CONCLUSIONS AND RECOMMENDATIONS

As explained in Section 3, Earth's atmosphere has a high degree of variability. In the lower part of the atmosphere (that is, for altitudes less than 5 km, aerosol density can be very high and quite variable in both composition and distribution of particle sizes. Visual range allows estimation of the aerosol content of the atmosphere but not of composition nor distribution of particle sizes. It is recommended that the atmosphere's spectral optical depth at the altitude of the sensor be measured and that the spectral optical thickness also be measured. This can be done by monitoring solar irradiance at the sensor altitude and the surface. Optical depth is a more meaningful parameter than visual range in radiative-transfer studies. In investigations of large-scale remote sensing by satellites, another quantity which can be used is atmospheric turbidity values of which are becoming available from many measuring sites in the United States.

In Section 4 we investigated the effect of composition and size distribution of aerosols on the single-scattering albedo and the single-scattering phase function. Changes in aerosol composition characterized by the imaginary part of the refractive index can considerably alter the single-scattering albedo. Of less importance is the change in size distribution. The single-scattering albedo is relatively insensitive to visual range up to about 20 km. This is true regardless of the degree of contamination (as expressed in terms of the refractive index).

Similar effects were found for the single-scattering phase functions. The change in size distribution did not have much effect on the shape of the phase function, but changes in the imaginary part of the refractive index did produce significant differences in the phase function at large angles. This suggests that lidar techniques might be employed to measure the backscatter coefficient (or the phase function at 180°). In turn, this would be useful in estimating the composition of aerosols.

In Section 5 we extended the current radiative-transfer model to include absorption. The single scattering albedos and phase functions calculated in Section 4 were then used in the radiative-transfer equations to determine spectral path radiance and total spectral radiance for various degrees of contamination. Radiances can change by at least a factor of six between a "clean" atmosphere and a strongly absorbing one. The actual atmosphere probably lies between these limiting cases. The variation in path radiance with nadir view angle is not greatly affected by degree of contamination, but the magnitude can differ by factors of four or five.

In Section 6 we considered the effect of background reflectance on radiance from a target element. First, a number of colored disks were chosen as the target with green vegetation as the background. Since this was done assuming isotropic scattering, the spectral variation actually was not realistic.

(-2

We also considered the more realistic case of anisotropic scattering by fitting actual calculated phase functions to an approximate exponential formula. The fit was surprisingly good, particularly for the angles of importance. These phase functions were then used in the single-scattering formulas to calculate singly-scattered surface radiance for a variety of situations. We found that background definitely influences the target and that the amount of influence depends upon the relative size of the target and the field of view, the relative reflectances of target and background, and the visual range. Although this influence of surface radiation is usually of lesser importance than that caused by radiation from the sky, in the case of large surface reflectances the effect is of equal importance. The result is that signatures based upon an analysis which excluded surface interaction could lead to inaccuracies in the recognition processing of multispectral data. Specific algorithms can be developed, however, to account for this effect and correct the data.

Finally, we investigated the more general problem of determining the radiance at any point in the atmosphere at which the surface is a non-uniform Lambertian reflector. For simplicity we assumed an infinite strip with one reflectance and a background with another. Thus, we simulated the case of an aircraft or spacecraft moving across the boundary between two dissimilar surfaces. A mathematical expression was obtained for the singly-scattered surface radiance as a function of distance from the strip, altitude of the sensor, reflectances of the surfaces, and atmospheric parameters. A numerical integration of the equation is necessary for realistic atmospheric conditions.

We highly recommend that specific flights be made to collect multispectral data for situations approximating the geometric and physical conditions used in the analysis of this report. Simple experiments will allow us to estimate the degree of contamination, and hence determine the variance in radiance. Likewise, the effect of background on target radiance should be investigated for the simple geometric conditions we have described.

Strong gaseous absorption effects in the infrared have been excluded in this analysis, but they can be considered by unifying the results obtained here with the ERIM band model for gaseous absorption. The unification of these two models would be particularly advantageous for remote sensing applications. Since there is a high degree of variability in the reflective and emissive properties of natural materials in the infrared region, a unified model which accounts for scattering and absorption by aerosols and gases could be used to correct multispectral data over the complete visible and infrared spectral regions.

In view of the development and use of meterological satellites, we now can obtain meaningful information on the actual state of the atmosphere at various locations and times over the entire globe. If such information were readily available to investigators they would have a more

efficient and economic means of applying atmospheric conditions in the processing of multispectral data. Therefore, a closer relationship between meteorological investigators and the earth-resources remote sensing community is highly desirable.

As a result of the knowledge and insights gained in this investigation we can now interpret real multispectral data in a more meaningful way. By means of techniques developed in this report, calculations based upon our present radiative-transfer model can be implemented to generate algorithms for the correction of real data for systematic atmospheric variations. Also, variances in multispectral data resulting from atmospheric effects can be simulated in a more realistic way.

Appendix
FOURIER TRANSFORM DERIVATION

The Fourier transform of intrinsic radiance t the surface is derived as follows.

$$\tilde{L}(k, 0) = \int_{-\infty}^{\infty} e^{ikx} L(x, 0)\, dx$$

where 0 implies zero altitude. Now, by definition the radiance is

$$L(x, 0) = \int_{0}^{2\pi} \int_{0}^{1} \mu' \rho'(x, \mu, \phi, -\mu', \phi') L(x, 0, -\mu', \phi')\, d\mu' d\phi$$

which, for a Lambertian surface, becomes

$$\frac{\rho(x)}{\pi} E(x)$$

Hence,

$$\tilde{L}(k, 0) = \frac{\bar{\rho}}{\pi} E(\bar{\rho}) \int_{-\infty}^{-x_o} e^{ikx}\, dx + \frac{\rho E(\rho)}{\pi} \int_{-x_o}^{x_o} e^{ikx}\, dx + \frac{\bar{\rho} E(\bar{\rho})}{\pi} \int_{x_o}^{\infty} e^{ikx}\, dx$$

$$= \frac{\bar{\rho} E(\bar{\rho})}{\pi} \left[\frac{2 \sin kM}{k} - \frac{2 \sin kx_o}{k} \right] + \frac{\rho E(\rho)}{\pi} \frac{2 \sin kx_o}{k}; \quad M \to \infty$$

$$= 2\pi \left\{ \frac{\bar{\rho} E(\bar{\rho}) \delta(k)}{\pi} + [\rho E(\rho) - \bar{\rho} E(\bar{\rho})] \frac{\sin kx_o}{k} \right\}$$

REFERENCES

1. R. M. Goody, Atmospheric Radiation, Oxford University Press, New York, 1964.
2. V. Ye. Zuyev, Propagation of Visible and Infrared Waves in the Atmosphere, NASA TTF-707, NTIS, U.S. Department of Commerce, Springfield, Va., 1970.
3. U.S. Standard Atmosphere Supplements, U.S. Government Printing Office, Washington, 1966.
4. G. M. Hidy and J. R. Brock, An Assessment of the Global Sources of Tropospheric Aerosols, Academic Press, New York, 1971, p. 1088.
5. F. E. Volz, Infrared Absorption by Atmospheric Aerosol Substances, J. Geophys. Res., 77, No. 6, 1972, p. 1017.
6. F. E. Volz, Infrared Optical Constants of Ammonium Sulfate, Sahara Dust, Volcanic Pumice, and Flyash, Appl. Optics ., No. 3, 1973, p. 564.
7. G. W. Grams, I. H. Blifford, Jr., B. G. Schuster, and J. J. DeLuisi, Complex Index of Refraction of Airborne Fly Ash Determined by Laser Radar and Collection of Particles at 13 km, J. of Atmos. Sciences, 29, 1972, p. 900.
8. D. F. Flanigan and H. P. DeLong, Spectral Absorption Characteristics of the Major Components of Dust Clouds, Appl. Optics, 10, No. 1, 1971, p. 51.
9. C. E. Junge, Journal Meteorol., 12, 1955, p. 13.
10. D. Deirmendjian, Electromagnetic Scattering on Spherical Polydispersions, Elsevier, New York, 1969, p. 78.
11. A. C. Holland and G. Gagne, The Scattering of Polarized Light by Polydisperse Systems of Irregular Particles, Appl. Optics, 9, No. 5, 1970, p. 1113.
12. R. S. Powell, R. R. Circle, D. C. Vogel, P. D. Woodson III, and B. Donn, Optical Scattering from Non-Spherical Randomly Aligned, Polydisperse Particles, Planet. Space Sci., 15, 1967, p. 1641.
13. D. M. Ruthven and K. F. Loughlin, Effects of Particle Shape and Size Distribution on the Transient Solution of the Diffusion Equation, Nature Phys. Sci., 230, 1971, p. 69.
14. C. Junge, Chemical Composition and Radioactivity of the Atmosphere, World Publishing Co., Cleveland, 1963.
15. L. S. Ivlev, Aerosol Model of the Atmosphere, Prob. Fiz. Atmos. Leningrad, No. 7, 1967, pp. 125-160.
16. B. J. Mason, The Physics of Clouds, Clarendon Press, Oxford, 1971.
17. N. A. Fuchs, The Mechanics of Aerosols, Pergamon, Elmsford, N. Y., 1964.
18. C. N. Davies, Aerosol Science, Academic Press, New York, 1966.
19. H. L. Green and W. R. Lane, Particulate Clouds, Dusts, Smokes and Mists, 2nd Edition, D. Van Nostrand, Inc., Princeton, 1964.
20. F. Linke, Handbuch der Geophysik, Vol. VIII, Springer-Verlag, Berlin, 1943.
21. K. Ya. Kondratyev, Radiation in the Atmosphere, Academic Press, New York, 1969.

22. D. T. Chang and R. Wexler, Relation of Aerosols to Atmospheric Features, Final Report AFCRL-68-0360, AD 674 629, Air Force Cambridge Research Laboratories, Bedford, Mass., 1968.

23. L. Elterman, An Atlas of Aerosol Attenuation and Extinction Profiles for the Troposphere and Stratosphere, Environmental Research Papers No. 241, Air Force Cambridge Research Laboratories, Bedford, Mass., 1966.

24. W. E. K. Middleton, Vision Through the Atmosphere, University of Toronto Press, Toronto, 1952.

25. P. N. Tverskoi, Physics of the Atmosphere, A Course in Meteorology, NASA TTF-288, TT65-50114, U. S. Department of Commerce, Washington, 1965.

26. Lord Rayleigh, Phil. Mag., 47, 375, 1899.

27. L. Elterman, U. V., Visible and IR Attenuation for Altitudes to 50 km, Report No. AFCRL-68-0153, Air Force Cambridge Research Laboratories, Office of Aerospace Research, Bedford Mass., 1970.

28. L. Elterman, Vertical-Attenuation Model with Eight Surface Meteorological Ranges 2 to 13 Kilometers, Report No. AFCRL-70-0200, Air Force Cambridge Research Laboratories, Office of Aerospace Research, Bedford, Mass., 1970.

29. A. L. Fymat and K. D. Abhyankar, Theory of Radiation Transfer in Inhomogeneous Atmospheres. I. Perturbation Method, Ap. J. Vol. 158, 1969, p. 315.

30. W. A. Malila, R. B. Crane, and R. E. Turner, Information Extraction Techniques for Multispectral Scanner Data, Report No. 31650-74-T, Willow Run Laboratories, Ann Arbor, 1972.

31. R. E. Turner and M. M. Spencer, Atmospheric Model for Correction of Spacecraft Data, Proceedings of the 8th International Symposium on Remote Sensing of Environment, Center for Remote Sensing Information and Analysis, Willow Run Laboratories, Ann Arbor, 1972.

32. R. E. Turner, Remote Sensing in Hazy Atmospheres, Proceedings of ACSM/ASP Meeting, Washington, March 1972.

33. K. Ya. Kondratyev, O. B. Vasilyev, L. S. Ivlev, G. A. Nikolsky, and O. I. Smokty, Influence of Aerosol on Radiative Transfer: Possible Climatic Consequences, University of Leningrad Press, Leningrad 1973.

34. M. M. R. Williams, Approximate Solutions of the Neutron Transport Equation in Two and Three Dimensional Systems, Nukleonik, Band 9, Heft 7, 305, 1967.

35. G. A. Garrettson and A. Leonard, Green's Functions for Multidimensional Neutron Transport in a Slab, Trans. Am. Nucl. Soc., Vol. 12, 159, 1969.

36. H. G. Kaper, Elementary Solutions of the Reduced Three-Dimensional Transport Equation, J. of Math. Phys., Vol. 10, No. 2, 1969, p. 286.

37. R. C. Erdmann, and A. Sotoodehnia, On the Solution of the Boltzmann Transport Equation in Two Dimensions, J. Of Math. Analysis and App., Vol. 31, 1970, p. 603.

38. G. B. Rybicki, The Searchlight Problem with Isotropic Scattering, J. Quant. Spectrosc. Radiat. Transfer, Vol. 11, No. 6, 1971, p. 827.